Quadrupole Electric Field for Erasing the Fine Structure Splitting of a Nanowire Quantum Dot Entangled Photon Source

by

Mohd Zeeshan

A thesis
presented to the University of Waterloo
in fulfillment of the
thesis requirement for the degree of
Doctor of Philosophy
in
Electrical and Computer Engineering
(Quantum Information)

Waterloo, Ontario, Canada, 2020

© Mohd Zeeshan 2020

Examining Committee Membership

The following served on the Examining Committee for this thesis. The decision of the Examining Committee is by majority vote.

External Examiner: Kimberley Hall
Professor, Dept. of Physics and Atmospheric Science,
Dalhousie University

Supervisor: Michael E Reimer
Assistant Professor, Dept. of Electrical and Computer Engineering,
University of Waterloo,

Internal Member: Michal Bajcsy
Associate Professor, Dept. of Electrical and Computer Engineering
University of Waterloo

Internal Member: Na Young Kim
Associate Professor, Dept. of Electrical and Computer Engineering,
University of Waterloo

Internal-External Member: Jonathan Baugh
Associate Professor, Dept. of Chemistry,
University of Waterloo

Author's Declaration

I hereby declare that I am the sole author of this thesis: see Statement of Contributions included in the thesis. This is a true copy of the thesis, including any required final revisions, as accepted by my examiners.

I understand that my thesis may be made electronically available to the public.

Statement of Contributions

The work presented in this thesis has contributions from several people. The nanowire quantum dot samples have been grown by our collaborators Dan Dalacu and Philip Poole at National Research Council Canada in Ottawa. The micro-PL experimental set-up was designed by me and built with the help from Arash, Nachiket and Michael. The initial idea for a quadrupole electric field was from Michael Reimer. I developed the theoretical framework for calculating the FSS as a function of a quadrupole electric field and performed the simulations with the assistance of Stefan Birner from NextNano. I have developed the majority of the fabrication recipes for the gated nanowire quantum dot devices with some initial help from Sandra Gibson and performed all of the micro-PL measurements on the nanowire quantum dot as a function of an applied quadrupole electric field. The automation codes for performing the fine structure splitting measurements were written by me, Juan Castaneda and Alain Bosch.

- Chapter 3 is adapted from our publication:
  M. Zeeshan, N. Sherlekar, A. Ahmadi, R. Williams, and M. Reimer, "Proposed Scheme to Generate Bright Entangled Photon Pairs by Application of a Quadrupole Field to a Single Quantum Dot" *Physical Review Letters*, vol. 122, p. 227401, June 2019.
- Chapter 5 is based on the manuscript that is under preparation for the publication:
  M. Zeeshan, D. Dalacu, P. J. Poole, S. J. Gibson and M. E. Reimer, "Quadrupole electric feld induced fine structure splitting tuning of the InAsP/InP quantum dot nanowire source,".

Abstract

Entanglement is an essential tool in QIP, for example, to achieve a secure quantum communication network and quantum computing. Semiconductor quantum dots can generate on-demand entangled photon pairs via the biexciton-exciton cascade. These solid-state sources are currently limited in their applications due to two major challenges: first is the collection efficiency since only a fraction of a percent of the emitted photons from the quantum dot can be collected due to its isotropic emission profile; and second is the FSS that causes an energy splitting of the intermediate exciton state —it arises due to strain and structural asymmetry of the quantum dot and degrades its measured entanglement fidelity. Quantum dots have been integrated into photonic structures such as microcavities and nanowires to enhance their collection efficiency by coupling the emitted photons to the cavity or fundamental nanowire waveguide mode. However, the fine structure splitting still remains a major challenge, and although many post growth perturbation techniques have been implemented to tune and completely erase the FSS of a self-assembled QD, erasing the FSS of a QD in a photonic structure has not yet been achieved. In this thesis, we propose and then demonstrate for the first time the tuning of the FSS for a InAsP QD in a tapered InP nanowire by applying a quadrupole electric field.

Out of all the post-growth perturbation based FSS erasing techniques, electric fields, and stress fields have been the most successful ones in erasing the FSS of a self-assembled quantum dot. However, implementing them on a nanowire quantum dot source is not a straightforward solution to its FSS problem. Stress field techniques are difficult to implement on a nanowire quantum dot source due to the thick nanowire shell around the quantum dot, where most of the applied external stress field relaxes and therefore doesn't reach the embedded quantum dot. The electric field on the other hand is known for reducing the e-h overlap and therefore if implemented in its conventional form will reduce

the QD brightness while erasing its FSS. Moreover, both stress and electric field techniques require multiple perturbation axes to erase the FSS of a quantum dot with any possible dipole orientation or macroscopic asymmetry. We overcame these problems by developing a novel approach of applying a quadrupole electric field along the plane of an embedded quantum dot inside the nanowire. We show theoretically that a quadrupole electric field corrects for the spatial asymmetry of the excitonic wave function for any quantum dot dipole orientation ($\theta = 0°, 10°, 20°$) inside a nanowire and completely erases its fine structure splitting from 11 μeV to 0.05 μeV while maintaining a strong e-h overlap ($\beta = 99\%, 90\%$ for a dot with $\theta = 0°, 20°$) even after applying a correction quadrupole electric field.

To experimentally demonstrate our theory we fabricated two prototypes of electrically gated InAsP/InP QD nanowire devices, with four metal gates precisely positioned around an individual InAsP quantum dot inside a vertically standing InP nanowire. The electro-optical characterization of an electrically gated nanowire quantum dot device shows the FSS tuning from 7 μeV to 4 μeV by application of a quadrupole electric field.

Although we have achieved a FSS tuning in nanowire device, tuning and completely erasing the FSS of a nanowire device will require a significant improvement in the fabricated device design. This will require reducing the dimension of the metal gates and aligning it perfectly to touch the sidewalls of the vertical nanowires. We also observed the degradation in the QD emission while exposing it to 100 kV e-beam. Therefore, we propose a bottom-up approach of fabricating the device by first patterning the metal gates by e-beam lithography on a wafer and then selectively growing the nanowire QD source at its center by the conventional site-selected VLS growth method. In principle, such an electrically gated device will erase the FSS of a nanowire quantum dot source and will bring it closer to becoming a deterministic source of entangled photons with near-unity fidelity and collection efficiency.

Acknowledgements

I would like to thank all those people whose constant support, help, and guidance made this thesis possible. First of all, I will thank Dr. Michael Reimer, who welcomed me in his Quantum Photonic Devices (QPD) group 5 years ago, introduced me to the field of experimental quantum optics, and gave me an opportunity to work on many fascinating theoretical and experimental projects. I had a wonderful experience of working under him, his positive attitude toward research and life created a conducive environment to work and learn in our lab. He also gave me the freedom to work on many projects and at the same time provided all the necessary support, resources, and insight to achieve the results. It was inspiring to have him as a mentor. Next, I should thank Dr. Dan Dalacu, Dr. Philip Poole, and Dr. Robin Williams from National Research Council, Ottawa, for providing us the nanowire quantum dot samples, they have always been accommodating to our project-specific requests and it is impressive to see how they have mastered the growth of this world-class entangled photon sources.

The first year of my Ph.D. was mostly spent on designing, acquiring, and building our experimental setup and I must thank Andreas Fognini for his guidance and support during this stage. Sandra Gibson initiated the fabrication process for our gated devices and she was the constant support to me in the cleanroom throughout my project, I have learned a lot from her and I am truly grateful for all of her support. I would also like to thank all my current and past QPD lab members: Arash Ahmadi, Nachiket Sherlekar, Sara Hosseini, Divya Bharadwaj, Michael Kobiersky, Lin Tian, Burak Tekcan, Bradly Van Kasteren, Simon Daley, Juan Castaneda, Alain Van Bosch, and Turner Garrow for being so supportive and contributing to my research through scientific discussion and collaborations. I would especially like to mention Arash and Nachiket with whom I shared my office space

throughout my Ph.D., you both were fun to be around, I had a great experience and I wish both of you a great future ahead.

I am also grateful to the Nathan Fitzpatrick, Vito Logiudice, and all the other members of the quantum nanofab cleanroom for providing technical support and help whenever I needed it. I thank Francois Sfigakis for his insight on device fabrication. Stefan Birner must be acknowledged for his support with the next nano software.

I would also like to thank all of my friends from both inside and outside of IQC who made my stay in Waterloo worthwhile. I will especially cherish the time spent with Kashif Sheikh and will miss our never-ending discussions about cricket and life. Zahid, Sarfaraz, Sameed, M Ali you guys were awesome housemates, and Aimal you are indeed an excellent trip planner thanks for planning that life-threatening but memorable white river rafting trip. Meenu thanks for inviting me to your weekend hangouts, I had a memorable time with Archana and Hemant at your place.

Finally, I have to thank those who are closest to me. My dear parents, you both were a constant source of inspiration for me. I always felt your love, affection, and support despite being so far from you. I will forever be grateful for your presence in my life.

Dedication

This is dedicated to my father.

Table of Contents

List of Figures xiv

List of Tables xvii

List of Abbreviations xviii

1 Introduction 1

1.1 Motivation 1

1.2 Photon Entanglement 4

1.3 Entangled photon sources: State-of-the-art 8

1.4 Thesis overview 13

2 Quantum dot in a Nanowire: Fundamentals 15

2.1 Band structure and quantum confinement in quantum dots 16

2.2 Optical Transitions 19

2.3 Biexciton-Exciton Cascade 23

2.4 Nanowire as a waveguide 26

2.5 Anisotropic exchange interaction: FSS 27

3 Proposal for an electrically gated nanowire quantum dot device 32

3.1 Proposed electrical device 32

3.2 Theory for calculating the FSS 34

3.3 Numerical Simulation 35

3.4 Results 38

4 Fabrication of a gated vertical nanowire quantum dot device 43

4.1 Current state-of-the-art and challenges 44

4.2 Step by step fabrication steps: UV lithography 46

4.2.1 Dielectric Deposition 47

4.2.2 Selected area removal of dielectric 49

4.2.3 Defining Gates 49

4.2.4 Metal deposition and liftoff 51

4.3 Step by step fabrication steps: E-Beam lithography 54

4.3.1 Dielectric Deposition 54

4.3.2 Defining Gates 54

4.3.3 Metal Deposition and lift-off 60

4.3.4 Selected area removal of dielectric 61

5 Characterization and Measurements **65**

5.1 Micro-PL experimental set-up . . . 66

5.2 Effect of SiO_2 shell on the QD emission . . . 67

5.3 UV Lithography device . . . 69

5.3.1 Photoluminescence and power dependent measurement . . . 69

5.3.2 Polarization dependent PL: FSS measurements . . . 72

5.3.3 FSS vs Electric field . . . 72

5.4 Ebeam lithography device . . . 76

5.4.1 Photoluminescence measurement . . . 76

5.5 Conclusions . . . 78

6 Conclusion and future outlook **79**

6.1 Summary . . . 79

6.2 Future Outlook . . . 80

References **83**

List of Publications **99**

APPENDICES **101**

A Fabrication recipe for a vertical nanowire device **102**

A.1 Fabrication steps with UV lithography . . . 102

A.2 Fabrication steps with e-beam lithography . . . 105

B Codes **108**

B.1 Next Nano simualtion code 108

B.2 Python code for 2D Gaussian fit of output wavefunctions from Next Nano 126

List of Figures

1.1 Graphical representation of a Bloch sphere 5

1.2 Comparison of entanglement fidelity versus collection efficiency at the first lens for SPDC and different quantum dot-based entangled photon sources . 11

2.1 Plots for density of states vs energy for a material with a confinement along its different dimensions 17

2.2 Geometry and Bandgap of InAsP/InP nanowire source 18

2.3 Two dimensional harmonics oscillator shell model 19

2.4 Energy band structure of the quantum dot and the allowed optical transitions between its ground states 20

2.5 Emission spectrum InAsP/InP nanowire quantum dot source 22

2.6 Biexciton-Exciton Cascade 25

2.7 Sketch of a typical InP/InAsP nanowire quantum dot source 26

2.8 Biexciton-exciton cascade with a FSS energy splitting Δ_0 31

3.1 Device design 33

3.2 Single particle wavefunctions with an applied quadrupole field 37
3.3 FSS as function of an external electric field 39
3.4 Universal FSS tuning 41

4.1 Nanowire sample image 45
4.2 Schematic of dielectric deposition on the vertical nanowire 47
4.3 Dielectric uniformity on the sidewalls of nanowires 48
4.4 Removal of dielectric from nanowire 50
4.5 Defining gates by UV lithography 51
4.6 Metal deposition and lift-off 52
4.7 Optical image of final device 53
4.8 Defining gates by e-beam lithography 55
4.9 E-beam Dose Test 56
4.10 SEM image of metal cross 57
4.11 Image of the device during the alignment tests 59
4.12 Gates alignment correction SEM image 60
4.13 SEM images metal deposition at UHV 61
4.14 Metal deposition: SEM image 62
4.15 Steps for selectively removing the dielectric and the SEM image of the final device 63

5.1 Schematic illustration of the experimental set-up for the polarization dependent micro-PL 66

5.2 Effect of SiO_2 deposition on the QD emission 68

5.3 Emission spectrum and power-dependent measurements 70

5.4 Polarization dependent measurements 71

5.5 Current vs Voltage swe 73

5.6 FSS as a function of applied quadrupole and lateral electric field 74

5.7 PL spectrum before and after e-beam exposure 77

6.1 Schematic of the proposed bottom-up fabrication steps 81

List of Tables

1.1 Measurement results for different choices of basis by Alice and Bob 7

3.1 Material parameters for GaAs and $InAs_{0.25}P_{0.75}$ quantum dot 36

4.1 Dimensions of the metal gates from an e-beam dose test. A schematic cross sectional illustration of the base of InP nanowire pattern on the chip during the metal deposition step. Different parameters in the table (t,t',w,w') are shown schematically in the figure. Top/Bottom, Left/Right indicates the gates location when viewed from the top as shown in the SEM images of figure 4.10 58

List of Abbreviations

AlGaAs aluminium gallium arsenide 16

Au Gold 51, 52, 56, 60, 104, 106

BOE buffered oxide etch 47--49, 64

DI deionized 55, 102--107

DOS Density of States 16

e-beam electron-beam vi, xvi, xvii, 14, 43, 51, 54--61, 65, 75--78, 80, 81, 105, 107

e-h electron-hole v, vi, 3, 25, 79

FSS fine structure splitting iv--vi, 2--4, 12--15, 31, 32, 34--36, 38--42, 65, 67, 72--76, 78--80, 82

GaAs gallium arsenide 16, 35, 36

HeNe Helium-Neon 66

InAs indium arsenide 16

InAsP indium arsenic phosphide v, vi, xiv, 3, 13, 16--18, 21, 22, 26, 43, 44, 46, 47, 54, 75, 76, 78, 79, 102

InP indium phosphide v, vi, xiv, xvii, 3, 13, 15--18, 20, 22, 26, 27, 43, 44, 46, 47, 54, 57, 58, 76, 78, 79, 102

IPA isopropyl alcohol 102, 103, 105--107

micro-PL micro-Photoluminescence iv, 14, 66, 69

MMA 8.5 methyl methacrylic acid 55, 60

NA numerical aperture 66

PECVD plasma-enhanced chemical vapor deposition 47, 67, 68, 78, 102, 105

PL Photoluminescence 65, 69, 72, 76

PMGI polydimethylglutarimide 49

PMMA A6 poly(meth)acrylates chlorobenzene 55, 105, 106

QD Quantum Dot v, vi, 2, 3, 10, 12--15, 17, 20, 22, 26, 43--47, 67--69, 72, 75, 76, 78--80, 102

QIP quantum information processing v

RPM rotations per minute 46

SEM Scanning electron microscope xv, xvii, 46, 48, 49, 58--61, 63, 64, 107

SiO_2 silicon dioxide 43, 47--50, 54, 61, 63, 64, 67, 68, 75, 76, 78, 102, 103, 105

SPDC spontaneous parametric down-conversion 8, 10

Ti titanium 51, 52, 56, 60, 61, 104, 106

TPE two-photon excitation 82

UHV Ultra-high vacuum 60, 61

UV Ultra Violet 13, 14, 43, 46, 49, 55, 65, 75, 78, 79, 102

VLS vapor-liquid-Solid vi, 3, 26, 44, 46, 54, 80

Chapter 1

Introduction

1.1 Motivation

The generation of photon entanglement is of fundamental importance to quantum information and communication [1]. Currently, in these applications, entangled photon pairs are most commonly produced with parametric down-conversion in a non-linear crystal with near-perfect entanglement fidelity [2]. Owing to their near-perfect entanglement fidelity these sources have long been used in many ground-breaking quantum optics experiments, secure quantum communication and also in addressing fundamental questions in quantum mechanics [3, 4, 5]. However, these sources are Poissonian, which means that they are probabilistic and most of the pulses are empty when operating with near 100 % entanglement fidelity. At higher brightness, multiple photons are emitted in the process due to their probabilistic nature, resulting in a rapidly decreasing entanglement fidelity. The extra emitted photon is undesirable as it can be utilized by an eavesdropper, thereby compromising the security of quantum communication. This limits such sources to operate at a source

efficiency below 1 % to maintain near-unity entanglement fidelity. Furthermore, these systems are incompatible with large scale integration as they are driven by complex lasers and optical tools. Semiconductor QDs can overcome these challenges as they generate single pairs of entangled photons on demand [6], have the potential to reach near-unity source fidelity and efficiency [7], are scalable [8] and can be easily integrated into semiconductor devices [9, 10]. These qualities of QDs as an ideal source for entangled photons pairs have attracted a lot of research in this field over the last decade.

An ideal solid-state QD-based entangled photon source should emit a pair of indistinguishable photons on-demand. 'On-demand' here means that the source should emit photons every time we activate it. Semiconductor quantum dots emit entangled photons on-demand; however, typically used QD are embedded in a three-dimensional semiconductor matrix with high refractive index. As a result the quantum dot emission is isotropic in all directions, thus limiting its collection efficiency to a fraction of a percent. For this purpose, QDs have been integrated into photonic nanowires [9] and micro-pillar cavities [11] to increase their collection efficiency. However, two major challenges remain before these QD sources can be used as a reliable entangled photon source in quantum optics experiments and various applications such as in secure quantum communication. First, is the degradation in the photon indistinguishably —this degradation is due to a fluctuating charge environment around the quantum dot [12]. Second, is the FSS [13] between the two bright exciton states, it reveals the which-path information in the biexciton-exciton cascade[14] and degrades the measured entanglement fidelity.

The first challenge is addressed via resonant excitation of the QD, it suppresses the charge noise around the QD, thereby, enhancing the indistinguishability of single photons to near-unity [6]. To overcome the long-standing problem of FSS, several QD growth techniques have been developed [15, 16, 17, 18], but reducing FSS below the exciton

radiative lifetime energy ($\sim 1\mu eV$) remains a significant challenge. Hence, many post-growth techniques have been developed to minimize the FSS, such as the application of electric fields [19, 20], strain fields [21], magnetic fields [22, 23] and a combination of strain and electric fields [24, 25]. These post-growth compensation techniques have been fairly successful in addressing the challenge of FSS tuning. The next significant step, is to apply these FSS compensation techniques to bright QD sources in photonic structures[9, 11].

Electric and stress field perturbations are by far the leading techniques for FSS compensation. Both of them can be implemented by fabricating micro-structures around the QD. Moreover, an electric field can also suppress the charge noise around the QD. However, strain compensation techniques are difficult to implement on photonic nanowire structures [9, 26] as the stress relaxes over a length scale of $\approx$ 100 nm [27] in the nanowire and therefore does not reach the QD. An electric field on the other hand reduces the brightness of the QD since it reduces the e-h overlap as the electron and hole is separated by the applied electric field [20]. Therefore, a novel device design and a perturbation approach are required that can address the challenge of compensating the FSS for a QD in a photonic nanowire [9] and micropillar cavity [11] without compromising its brightness.

In this thesis, we propose and demonstrate a novel electrical device that can tune the FSS of a single InAsP/InP nanowire quantum dot entangled photon source [8, 9] by applying a quadrupole electric field in the plane of the QD. The nanowire acts as a waveguide for directional QD emission and the tapered nanowire geometry enhances the photon collection efficiency at the nanowire top by reducing total-internal reflection [28]. They are grown by a selected area VLS growth [29] technique. Therefore, we can control the coordinates of each nanowire quantum dot entangled photon source. The underlying theory for tuning the FSS of a quantum dot by a quadrupole electric field has been discussed in detail in our theoretical proposal [30]. We have proposed that a quadrupole electric field can erase the

FSS of the quantum dot for any dipole orientation, while maintaining a strong e-h overlap and therefore the quantum dot brightness. Based on our theoretical modeling we developed, we have fabricated a vertical nanowire with four electrical gates surrounding the quantum dot and demonstrated the tuning of the nanowire quantum dot FSS by application of a quadrupole electric field. In principle, such an electrical device would erase the FSS of the nanowire quantum dot and bring it closer to becoming a deterministic source of entangled photons with near-unity efficiency and fidelity.

1.2 Photon Entanglement

Quantum entanglement is an intriguing phenomenon first proposed by Schrödinger [31] in 1935 to describe the state of a quantum system which cannot be describe as a product of its subsystems, for a bipartite system that is,

$$|\Psi_{ab}\rangle \neq |\Psi_a\rangle \otimes |\Psi_b\rangle \tag{1.1}$$

This means that a state of a system $|\Psi_{ab}\rangle$ cannot be written as a tensor product of its two constituent pure states $|\Psi_a\rangle$ and $|\Psi_b\rangle$. An example of such a state is $|\phi\rangle = \frac{1}{\sqrt{2}}(|\uparrow\downarrow\rangle + |\downarrow\uparrow\rangle)$ for a system of two photons where $\uparrow, \downarrow$ are the two possible polarization states in its computational basis. Quantum entanglement describes a strong correlation between the quantum states that could not be achieved by any classically correlated states. Experimental realization of an entangled photon pair has been used in experiments to demonstrate the quantum nature of its polarization correlations [32]. These polarization-entangled photon sources have been used in many ground-breaking experiments to confirm quantum predictions [33, 34] and disprove semi-classical theories such as the violation of Bell inequality

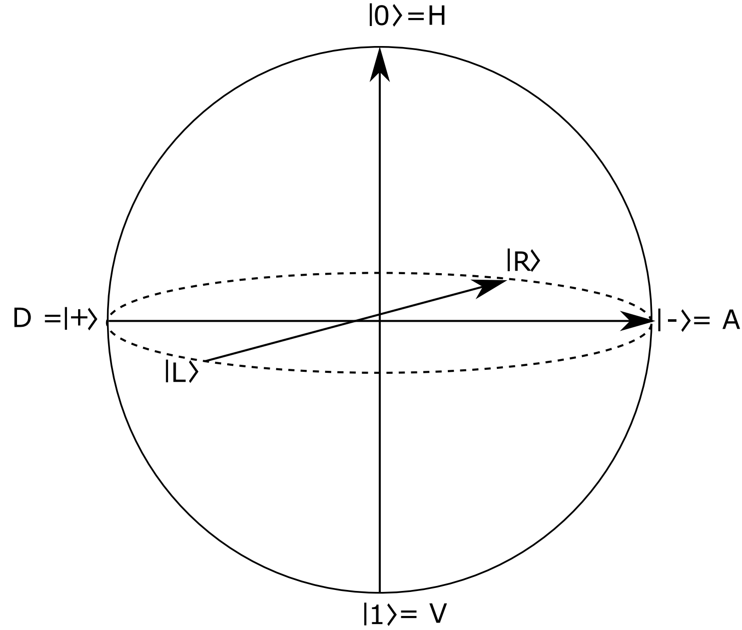

Figure 1.1: Bloch Sphere: A state of the qubit is represented by an arrow originating from the origin to the surface of the sphere. $|0\rangle = H$, $|1\rangle = V$ are the eigenstates in the computational basis, $|R\rangle / |L\rangle = \frac{1}{\sqrt{2}}(|0\rangle \pm i\,|1\rangle)$ in the circular basis and $|\pm\rangle = |D\rangle / |A\rangle = \frac{1}{\sqrt{2}}(|0\rangle \pm |1\rangle)$ in the circular basis

to exclude a local realistic description [35, 2]. Therefore, from the early stage on, photon entanglement became an essential tool both in theory and experimental quantum physics.

We will keep our discussion for photon entanglement to two particles, but this definition can be extended to multi-particle systems. Polarization encoded qubit of a single photon can be represented graphically on a Bloch sphere as shown in Fig. 1.1 and it can take values that are in a superposition of its two eigenstates $|0\rangle$ and $|1\rangle$:

$$|\Psi\rangle = \alpha\,|0\rangle + \beta\,|1\rangle \tag{1.2}$$

where α and β can be any complex numbers which satisfies $|\alpha|^2 + |\beta|^2 = 1$. The polarization state of a single photon can be mapped to this Bloch sphere by a vector that points towards

the three orthonormal planes representing three basis, these are:

$$\begin{gathered}
|H\rangle = |0\rangle , |V\rangle = |1\rangle \\
|D\rangle = \frac{1}{\sqrt{2}}(|0\rangle + |1\rangle), |A\rangle = \frac{1}{\sqrt{2}}(|0\rangle - |1\rangle) \\
|R\rangle = \frac{1}{\sqrt{2}}(|0\rangle + i\,|1\rangle), |L\rangle = \frac{1}{\sqrt{2}}(|0\rangle - i\,|1\rangle)
\end{gathered} \tag{1.3}$$

These basis for a polarization state of light is called $|H\rangle\,|V\rangle$ linear, $|A\rangle\,|D\rangle$ diagonal and $|R\rangle\,|L\rangle$ circular.

The combined state of two photonic qubits has eigenstates in a four-dimensional Hilbert space. The two photon state can be projected onto four special maximally entangled Bell states:

$$\begin{aligned}
\left|\phi^+\right\rangle_{12} &= \frac{1}{\sqrt{2}}(|H\rangle_1\,|H\rangle_2 + |V\rangle_1\,|V\rangle_2) \\
\left|\phi^-\right\rangle_{12} &= \frac{1}{\sqrt{2}}(|H\rangle_1\,|H\rangle_2 - |V\rangle_1\,|V\rangle_2) \\
\left|\psi^+\right\rangle_{12} &= \frac{1}{\sqrt{2}}(|H\rangle_1\,|V\rangle_2 + |V\rangle_1\,|H\rangle_2) \\
\left|\psi^-\right\rangle_{12} &= \frac{1}{\sqrt{2}}(|H\rangle_1\,|V\rangle_2 - |V\rangle_1\,|H\rangle_2)
\end{aligned} \tag{1.4}$$

These bell states cannot be written as a product of two single photon states. If the two parties say Alice and Bob share a pair of photons that are entangled in the Bell state $|\phi^+\rangle$, both Alice and Bob can independently perform measurements on their photons and share the information among themselves to verify the correlations. Now if Alice chooses to measure her photon in a linear basis she will get $|H\rangle$ or $|V\rangle$ with equal probability. However, Alice's measurement will cause the state to collapse in either of the two $|\phi^+\rangle$ states $|H\rangle\,|H\rangle$ or $|V\rangle\,|V\rangle$. Therefore, Bob's measurement would certainly result in the same as Alice if he chooses the linear basis. However. the $|\phi^+\rangle$ state can be rewritten into the

diagonal and circular basis as follows:

$$\left|\phi^{+}\right\rangle = \frac{1}{\sqrt{2}}(\left|H\right\rangle_1 \left|H\right\rangle_2 + \left|V\right\rangle_1 \left|V\right\rangle_2) = \frac{1}{\sqrt{2}}(\left|D\right\rangle_1 \left|D\right\rangle_2 + \left|A\right\rangle_1 \left|A\right\rangle_2) = \frac{1}{\sqrt{2}}(\left|R\right\rangle_1 \left|L\right\rangle_2 + \left|L\right\rangle_1 \left|R\right\rangle_2) \tag{1.5}$$

Therefore, Alice and Bob will observe a correlation in their measurements if they both choose a linear and diagonal basis, and they will get anti-correlations if they choose a circular basis. The possible combination of measurements that can be performed by Alice and Bob are summarised in Table. 1.1. This strong correlation among the shared qubits could not be achieved for any state prepared by a classical machine.

State: $\left|\phi^{+}\right\rangle$	Alice choice of Basis	Bob choice of Basis	Measurement results
1	linear	linear	correlated
2	diagonal	diagonal	correlated
3	circular	circular	anti-correlated
...	No correlation for the other combination of Basis		

Table 1.1: Measurement results for different choices of basis by Alice and Bob

Moreover, both Alice and Bob can independently apply a local unitary Pauli operation to their photons to change the state from one Bell state to another. For example, Alice can change the state from $\left|\phi^{+}\right\rangle$ to $\left|\phi^{-}\right\rangle$ by applying a σ_z Pauli operator to her qubit, similarly, she can change it to the other Bell states by applying σ_x and σ_y operators, respectively. Therefore, the entanglement is preserved under these unitary operations.

These maximally entangled Bell states are special cases and it is difficult to produce these states experimentally. However, these states are used as a benchmark to calculate the entanglement fidelity of an experimentally produced state. Fidelity gives the measure

of how easily the two quantum states can be confused. Therefore, a given two-qubit state ψ with a density matrix $\rho = |\psi\rangle\langle\psi|$ will have a fidelity to the other state ϕ with density matrix $\sigma = |\phi\rangle\langle\phi|$ as follows:

$$F(\rho, \sigma) \equiv tr\sqrt{\rho^{\frac{1}{2}}\sigma\rho^{\frac{1}{2}}} \tag{1.6}$$

Generally, the reference state ϕ is chosen as one of the Bell states and the reference state ψ can have a fidelity between 0-1 depending on how indistinguishable they are. Another way of quantifying the degree of entanglement is by measuring its concurrence, it quantifies the separability of a state. Bell states are not separable, hence, they have a high concurrence value. To estimate the concurrence of an entangled system ($\rho = |\psi\rangle\langle\psi|$), with a spin flipped state ($\left|\tilde{\psi}\right\rangle = \sigma_y |\psi\rangle$) and a density matrix $\tilde{\rho} = (\sigma_y \otimes \sigma_y)\rho^*(\sigma_y \otimes \sigma_y)$. The concurrence is given by the overlap between the original state and its spin-flipped state [36] as,

$$C(\rho) = |\langle\psi|\tilde{\psi}\rangle| \tag{1.7}$$

where σ_y is the Pauli matrix.

1.3 Entangled photon sources: State-of-the-art

The field of entangled photon sources has been developing rapidly over the last few decades. Entangled photon pairs were first realized from atomic emissions [33] in the early 1970's, but the major breakthrough in this field came with the arrival of SPDC sources [37]. In such SPDC sources, the coherent pulses of the laser are incident on a non-linear crystal and subsequently down-converted into a pair of photons, called idler and signal, according to the conservation of energy and momentum. Therefore, they are strongly correlated in time and exhibit high polarization entanglement fidelity. Moreover, the detection of an

idler photon can turn the signal photon into a heralded single photon. Therefore, these sources became the most preferred sources for quantum optics experiments [3, 4, 5] since its inception. However, the wish-list for ideal entangled photon sources expanded over time with the emergence of novel quantum communication protocols [38], linear optical quantum computing [39] and the proposal for building a long-distance secure quantum internet network [40] with quantum repeaters. These new avenues of quantum technologies require an entangled photon source with the following desired properties:

- High entanglement fidelity: emitted photon pair should have a near-unity entanglement fidelity.
- On-demand: 100 % excitation and collection efficiency.
- Low multiphoton emission: One, and only one, photon pair should be emitted from each trigger.
- Indistinguishability: The successive photons emitted from the source should be indistinguishable from each other in all degrees of freedom. i.e., energy, coherence length, line-width, polarization, etc. This is a requirement for performing many quantum communication and computing protocols.
- Tunable: Entanglement swapping in quantum repeater and linear optical quantum computing protocols requires interfering photons from different sources. Therefore, it is desirable to have sources with tunable energy, coherence length, linewidth, etc.
- High-brightness: A source with a high rate of photon-pairs is desirable for overcoming the environmental noise and channel losses. In quantum key distribution (QKD), it would allow a higher key generation rate and the transmission of the photons over longer distances.

- Fourier limited photon: The emitted photons should be monochromatic and should not have any inhomogeneous broadening.
- Gaussian mode: In order to efficiently couple the photons to a single-mode optical fiber the emitted photon should have a Gaussian mode.
- Scalable: The sources should be compact and scalable; position controlled and can be integrated on a semiconductor chip.

As discussed in the motivation section, entangled photon sources based on SPDC are Poissonian and therefore have a fundamental limitation in reaching an on-demand performance. In figure 1.2 we plot the entanglement fidelity versus the pair collection efficiency at the first lens, for state-of-art SPDC sources, blue circles. The minimum entanglement fidelity required to violate Bell's inequality is given by the green dashed line in figure 1.2. Even higher entanglement is needed for secure communication. For example, the blue dashed line in figure 1.2 indicates the minimum calculated fidelity required to ensure a secure key is transferred. However, in practice due to losses and noise in the channel a much higher entanglement fidelity is needed (>95%, red dashed line in figure 1.2). In order to overcome this limitation, there has been extensive research going on in the field of semiconductor quantum dot sources. Quantum dot-based sources have the potential of becoming an ideal entangled photon source required by many novel quantum technologies. However, the first generation of QD sources, self-assembled QD [50, 51] suffered from a very low photon collection efficiency since they were embedded in a high refractive index material. As a result, the photons are emitted isotropically in all directions. In addition, the photons that make its way towards the top experience a strong total internal reflection at the semiconductor-air interface and only a very small fraction of them can be extracted to the collection optics. In figure 1.2 the performance of many recent self-assembled QD

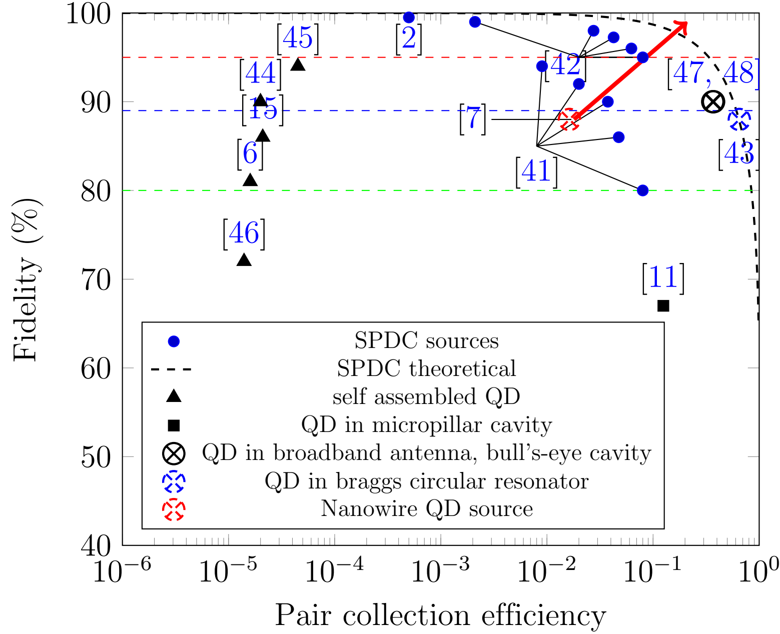

Figure 1.2: Comparison of entanglement fidelity versus collection efficiency at the first lens for SPDC and different quantum dot-based entangled photon sources. Performance of: SPDC sources (blue circles); self-assembled QD sources (black triangles); QDs in different nanostructures including a photonic cavity (black square), optical antenna and Bragg's bull's eye cavity (black circle with cross), Bragg's circular resonator cavity (blue circle with cross) and photonic nanowire as used in this thesis (red circle with cross). Pair collection efficiency of 1 means 100 % probability of collection the entangled photon pairs at the first lens. The black dashed line indicates the theoretical upper limit for the performance of SPDC sources. The lower limit of the entanglement fidelity required to violate the Bell's inequality and performing quantum key distribution is shown by green dashed line, blue dashed line (theoretical QKD limit) and red dashed line (practical QKD limit) respectively. The red arrow depicts the projection of where we want to take the performance of our nanowire QD sources with this work. This figure is adapted and modified from figure 6. in [49]

sources are plotted, black triangle, whereby they all show a very low collection efficiency. However, significant advances have been made in terms of their performance, Huber et al. showed a near-unity ~ 0.98 entanglement fidelity [45], and Trotta et al. have achieved an independent tuning of the QD FSS and the emission energy [52, 53].

In order to address the issue of collection efficiency the QD have been integrated into photonic structures. Dousse et al. [11] was the first to show the extraction of entangled photon pairs for a QD in a photonic micropillar cavity structure and succeeded in achieving the extracting efficiency of 0.12 per pulse with an entanglement fidelity of 67 %, it is plotted by the black square in figure 1.2. Muller et.al [6] have achieved a near-unity (~ 0.98) pair generation with a very low mutliphoton emission, $g^2(0) = 7.5e-5$ from the photonic cavity. Somaschi et al. [54] engineered the charge environment of the QD embedded in a micropillar cavity by an external electric field to achieve near-unity photon indistinguishability (~ 0.99) through resonant optical excitation. QD have also been very recently integrated with a broadband antenna [47], and bull's eye cavity [48] to achieve a remarkable collection efficiency of 0.365 and 0.375 with a fidelity of 90 %, respectively. These are both plotted by the black circle with a cross in figure 1.2. Liu et al. [43] have achieved the best performance for any QD entangled photon source to date with an entanglement fidelity of 88 % and a pair collection efficiency of 0.65 for a GaAs QD in a broadband photonic nanostructure consisting of a circular Bragg resonator on a broadband reflector. This result is plotted by the blue circle with a cross in figure 1.2. Reimer et al. [9] developed the QD in a photonic nanowire. It was further shown by Bulgarini et al. [55] that the tapered nanowire can guide the broadband QD emission into a Gaussian mode with a fidelity of 99 %. Fognini et al. [7] have further achieved the fidelity of 88 % with a pair collection efficiency of 1.63 % from the nanowire QD sources by quasi-resonant excitation. In that work, they have further shown that with resonant excitation and detection system with ultra-low timing

jitter and dark counts it's possible to achieve unity entanglement. The performance of the QD nanowire source is plotted by a red circle with a cross in figure 1.2. The red arrow on the figure 1.2 depicts the projection of where we want to take the performance of our nanowire QD sources by erasing its FSS. However, with an optimized tapering (2°) and the integration of mirror below the nanowire source, a near unity pair (0.94) collection efficiency could be achieved.

1.4 Thesis overview

In **chapter** 2, we describe the background and fundamentals of an InAsP quantum dot in an InP nanowire waveguide. This includes the band structure, optical transitions, and biexciton-exciton cascade that leads to a pair of polarization-entangled photons. It is followed by the discussion on the waveguiding effect of an InP nanowire that effiently guides the quantum dot photons in the desired direction and the theoretical origin of FSS in the QD: anisotropic exchange interaction.

In **chapter** 3, we propose our device design through which we can apply a quadrupole electric field to the QD inside the nanowire. We then present the theoretical simulations for the device to show its response to an applied external quadrupole and lateral electric field. Finally, we show that such a device can correct and erase the FSS of a QD for any dipole orientation while preserving the QD brightness.

In **chapter** 4, we present the fabrication recipes of an electrically gated vertical nanowire device with four gates surrounding the nanowire quantum dot. We present the fabrication steps for two types of devices. In the first generation of devices, metal gates were fabricated by patterning the photoresist by UV lithography, and in the second generation of devices,

metal gates were fabricated by patterning the photoresist by e-beam lithography in order to achieve a closer spacing of the electrical gates.

In **chapter** 5, we present optical and electrical measurements performed on our devices. We performed micro-PL and power dependent-micro-PL to identify the exciton and biexciton transitions for the UV device. Next, we performed polarization-dependent micro-PL to measure its intrinsic FSS value (7 μeV). Finally, we show that we can tune the FSS of our device by applying a quadrupole electric field to 4 μeV, before our device starts leaking current. We also measured the FSS of the same device as a function of lateral electric field and showed that we can reduce the FSS to 5 μeV. This lower bound of FSS is expected in our theoretical model when the dipole orientation of the QD is not aligned with our metal gates. However, we were limited by an electrical leakage in our device to further reduce the FSS. We then present the micro-PL measurements performed on the e-beam device.

In **chapter** 6, we summarise all of our results, discuss the strategies to overcome the current limitations of our device, and provide an outlook for future research in this field.

Chapter 2

Quantum dot in a Nanowire: Fundamentals

In this chapter, we will discuss the fundamental properties of a quantum dot in a nanowire. We will start by discussing the band structure of the QD and the quantum confinement of the charge carriers inside the QD that leads to discrete energy shells. Then we will discuss the optical selection rules, that govern the QD emission spectrum and the biexciton-exciton cascade in its s-shell, which produces a pair of polarization-entangled photons. It is followed by the discussion on the waveguiding effect of an InP nanowire and how it suppresses the total internal reflection at its top due to its tapered geometry. Finally, we present the theory of anisotropic exchange interaction that couples the spin of electron and hole in an exciton and causes an energy splitting between the neutral exciton states known as FSS.

2.1 Band structure and quantum confinement in quantum dots

Semiconducting quantum dot's are nanostructures where a low bandgap materials eg. GaAs, InAsP, are embedded inside a higher bandgap materials eg. AlGaAs, InP. Due to the Type-I bandgap alignment, the nanoscale region of a low bandgap material forms a three-dimensional confinement potential for the electrons and holes. In this chapter, we will keep our discussion to the wurtzite InAsP/InP (quantum dot/nanowire) structure with cylindrical geometry. However, the underlying physics can also be applied to the other III-V group direct bandgap semiconductor quantum dots, with different geometries (hexagonal, triangular, etc.).

Let us start by discussing the DOS of material and how does it change when we reduce its dimensions (quantum confinement) along its different directions. In Fig. 2.1 (a-d), we could see how the DOS of material changes from a continuum (bulk) to discreet energy (quantum dot), as we reduce its dimensions (across its three axes) below its carriers Bohr radius (a_0). The discreet energy levels of the quantum dot can be numerically computed by performing atomistic calculations and taking into account the many-body effect of all its atoms(10^6). However, this requires a lot of computing time and resources. Therefore, we will use an effective mass approach [56] to analytically calculate its energy levels. The main parameters that are required for this calculations are the bandgap values, effective masses of electron (m_e^*), heavy-hole (m_{hh}^*), and the light-hole (m_{lh}^*) of InP and $InAs_xP_{1-x}$ quantum dot with a ternary variable x (values between 0 and 1). The ternary variable x is the doping concentration of As in the quantum dot and its typical value is around 0.25. The effective mass for the quantum dot is calculated by linear interpolation of InP and InAs effective masses, $m_{i,Inp}^*(1-X) + m_{i,InAs}^*X$, i = e,hh,lh, and the growth direction for

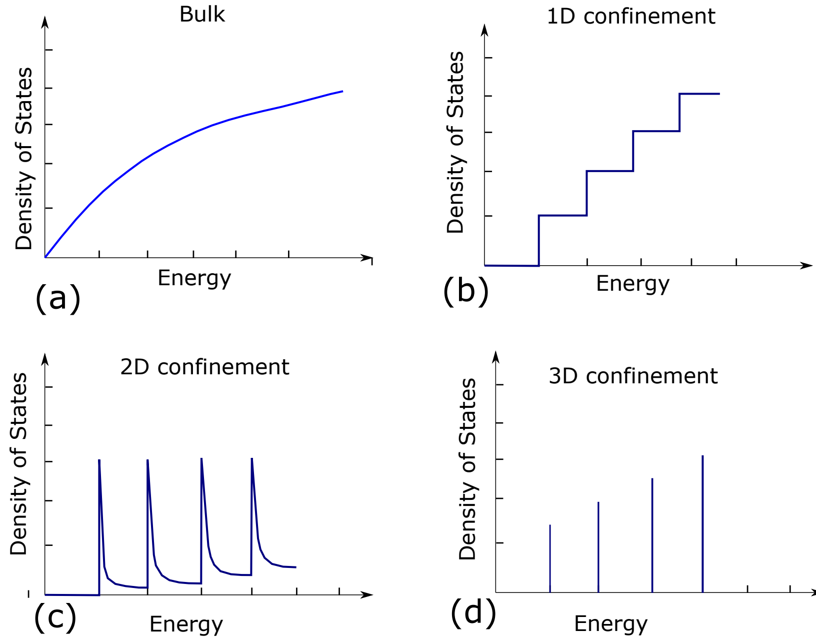

Figure 2.1: Plots for density of states vs energy for a material with a confinement along its different dimensions: (a) Bulk. (b) 1D confinement (quantum well). (c) 2D confinement (quantum wire). (d) 3D confinement (quantum dot).

the QD is considered to be along the z-axis.

A typical InAsP quantum dot in a nanowire has a height of 4-8 nm and a diameter of 20-30 nm. In Fig.2.2 (a) we sketch the schematic of a typical disc shape InAsP quantum dot inside a InP nanowire. In this geometry, the axial confinement along the z-direction is much stronger than the radial direction. Hence, we can treat the confinement along the axial (z) direction and radial direction (r, θ) separately. In the z-direction, the energy level can be calculated by treating the quantum dot as a finite potential well of a width h. For a quantum dot with h $\leq$ 10 nm only a single energy level is confined in the conduction the valance band for the electron and holes as shown in Fig 2.2 (b) [57]. A heavy-hole form the ground state of valance band since they have lower confinement energy due to their heavier

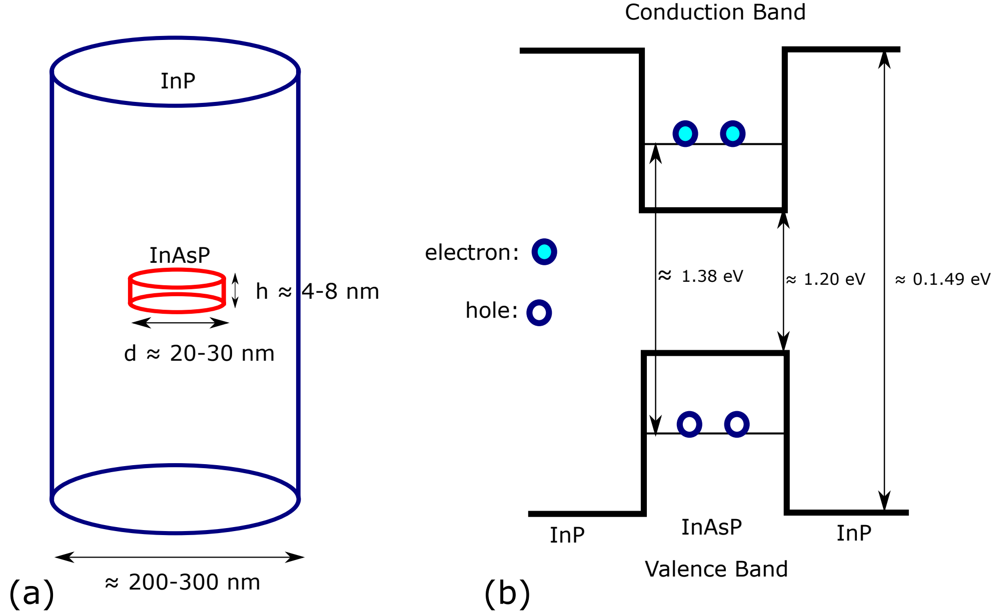

Figure 2.2: Geometry and Bandgap: (a) Sketch of a disk shaped InAsP quantum dot of height h and dimeter d embedded inside a InP nanowire. (b) A band structure of an $InAs_{0.25}P_{0.75}$ quantum dot inside the InP nanowire when only a strong confinement along its z direction is considered.

effective mass. However, the weaker lateral confinement (d>h) further splits this single confined energy levels into sublevels. The lateral confinement potential can be modeled as a two-dimensional harmonic oscillator, V(r) = $\frac{1}{2}m^*\omega r$, where m^* is the effective mass of the carriers and ω is the conduction or valence band harmonic oscillator frequency [57]. In the absence of an external magnetic field this potential can be analytically solved to give energy eigenstates, $E_{n,l} = (2n + |l| + 1)\hbar\omega_{e/h}$ known as Fock-Darwin states. Here, n (=0,1,2,..) is the radial quantum number, l (= 0, ±1, ±2,...) is the angular momentum quantum number of the oscillator and $\hbar\omega_{e/h}$ is the confinement energy for the electron/hole. Each energy shell can be occupied by two carriers of the opposite spin due to the Pauli exclusion principle. By the convention of atomic physics the ground state $E_{0,0}$ is named as

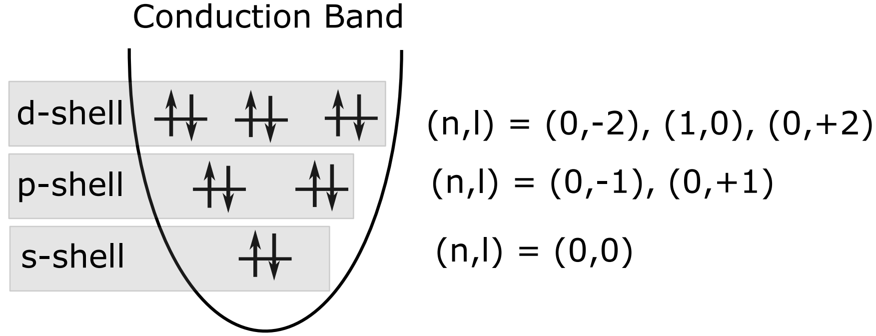

Figure 2.3: Two dimensional harmonics oscillator shell model: Electrons in a conduction band with energy levels and spin degeneracy indicated by radial quantum number (n) and angular momentum quantum number (l).

the s-shell, the degenerate energy levels $E_{0,-1}, E_{0,+1}$ as p-shell and the degenerate energy levels $E_{0,-2}, E_{1,0}, E_{0,2}$ are named as d-shell, refer Fig. 2.3. The energy separation between these shells can be calculated by the following formula [57],

$$\Delta E_{s-p} = \hbar\sqrt{\frac{2\Delta E_c}{m_e}\frac{1}{R}} \tag{2.1}$$

where, ΔE_c is the conduction band offset, m_e is the electron effective mass, and R is the radius of the quantum dot.

2.2 Optical Transitions

The optical transitions between the discreet energy levels of the quantum dot are governed by the optical selection rules. According to this selection rule, the angular momentum should be preserved in the electron-hole recombination and the photon generation. The total angular momentum of the carriers in the band is given by, $\mathbf{J} = \mathbf{L_{band}} + \mathbf{L} + \mathbf{S}$, where $\mathbf{L_{band}}$ is the angular momentum of the band, $\mathbf{L}$ is the orbital angular momentum of the

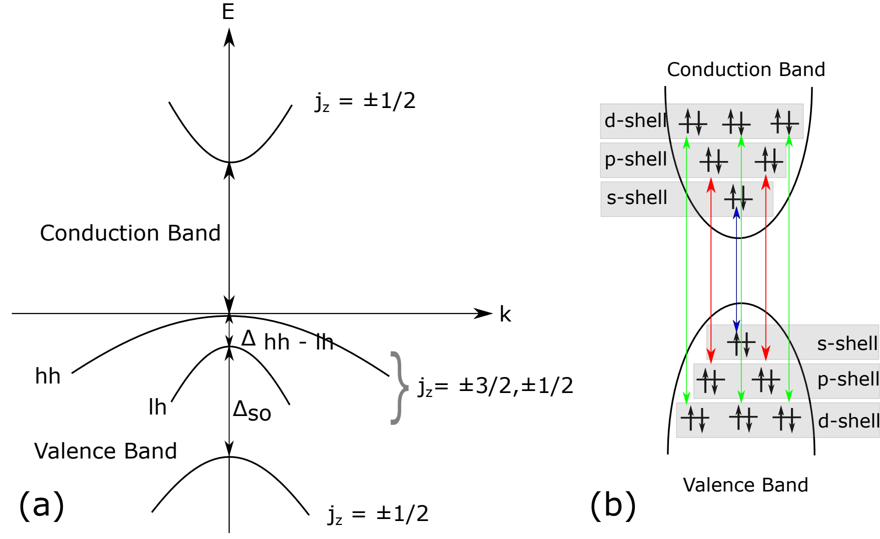

Figure 2.4: Energy band structure of the quantum dot and the allowed optical transitions between its ground states: (a) Energy Vs momentum band structure of quantum dot. The conduction band has only one band for $j_z = 1/2$, while the valance band has three bands for heavy-hole, light-hole and split-off bands. j = 1/2 and j = 3/2 bands are separated in energies by Δ_{So} and j =3/2 band is further splitted into heavy-hole ($j_z = 3/2$) and light-hole ($j_z = 1/2$) by Δ_{hh-lh}. (b) Allowed optical transitions ($\Delta l = 0$) between the QD conduction and valance band. Arrows with different color represent the transitions between different shells (s-shell = blue, p-shell = red, d-shell = green).

orbital in the shell originating from the Fock-Darwin states and **S** is the carriers spin angular momentum. The total angular momentum **J** can be represented by the quantum number j and its z-component $j_z \in \{-j, -j+1, ..., j-1, j\}$, similarly, the quantum number of the spin is s, with its z-component $s_z \in \{-s, -s+\frac{1}{2}, ..., s-\frac{1}{2}, s\}$.

In the InP, the electron at the conduction band minima occupies the s-like orbitals i.e. $\mathbf{L_{band}} = \mathbf{0}$, while hole at the minima of valence band occupies p-like orbital i.e. $\mathbf{L_{band}} = \mathbf{1}$. The spin angular momentum is $\frac{1}{2}$ for both electron and holes. Hence, the total angular

momentum for the s-shell ($\mathbf{L} = \mathbf{0}$) electron will be, $j = s = \frac{1}{2}$ and $j_z = \{-\frac{1}{2}, +\frac{1}{2}\}$, for hole, $\mathbf{J} = \mathbf{L_{band}} + \mathbf{S}$, $j = \{|l_{band}+s|, |l_{band}-s|\} = \{\frac{3}{2}, \frac{1}{2}\}$ with $j_z = \{-\frac{3}{2}, -\frac{1}{2}, \frac{1}{2}, \frac{3}{2}\}$, $j_z = \{-\frac{1}{2}, +\frac{1}{2}\}$ respectively.

The hole state, $\mathbf{J} = \mathbf{\frac{1}{2}}$ is separated in energy from $\mathbf{J} = \mathbf{\frac{3}{2}}$ due to the spin-orbit interaction ($\Delta_{so} \approx 100$ meV's for InAsP Q.D.), and is known as split-off band. The $\mathbf{J} = \mathbf{\frac{3}{2}}$ is further split into two bands, $j_z = \{+\frac{1}{2}, -\frac{1}{2}\}$ (light-hole) and $j_z = \{+\frac{3}{2}, -\frac{3}{2}\}$ (heavy-hole). These bands are degenerate in bulk InAsP. However, in InAsP Q.D. the degeneracy of these bands are lifted due to the quantum confinement owing to a different effective masses ($m^*_{hh} > m^*_{lh}$) of hole in these bands and the strain. The Energy vs Momentum (k) band structure of the InAsP quantum dot is shown in the Fig. 2.4 (a). The conduction band has the single $j_z = \pm\frac{1}{2}$ electron state. While, the valence band has three separate bands heavy-hole, light-hole and the split-off band. The heavy-hole ($j_z = \pm\frac{3}{2}$) and light-hole ($j_z = \pm\frac{1}{2}$) bands are separated by ten's of meV's (Δ_{hh-lh}) and the split-off is separated from the $\mathbf{J} = \mathbf{\frac{3}{2}}$ band by hundred's of meV's (Δ_{so}). Hence, we can neglect the split-off band and light-hole band while considering the ground state transitions of the quantum dots. The ground state transitions will be between $j_z = \pm\frac{1}{2}$ electron band and $j_z = \pm\frac{3}{2}$ heavy hole band.

The angular momentum of the circularly polarized photon is $\pm\hbar$ and its spin is one. Hence, the selection rule for an electron-hole recombination should be,

$$\begin{aligned} \Delta j_z &= \pm 1, \\ \Delta s &= 0, \end{aligned} \tag{2.2}$$

Since, the $\mathbf{L_{band}}$ in $\mathbf{J}$ takes care of $\Delta j_z = \pm 1$, the transitions between electron and hole are only allowed when $\Delta l = 0$ for shells. In Figure. 2.4. (b) the allowed optical transitions

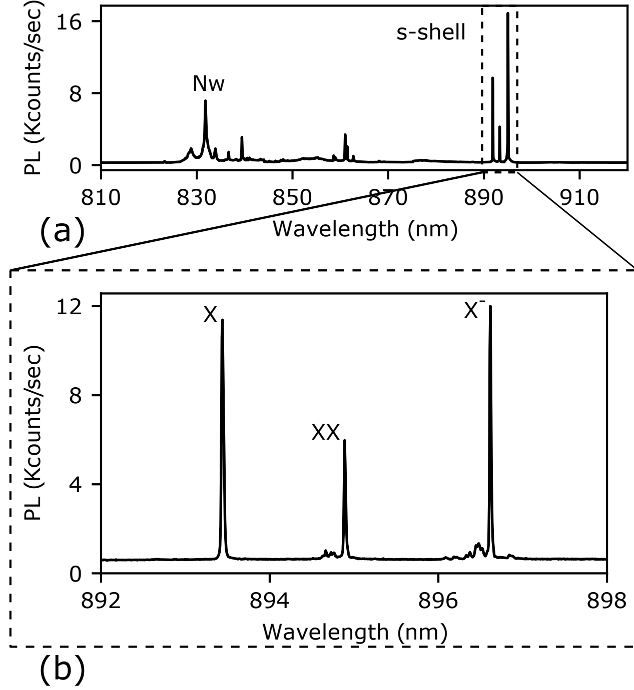

Figure 2.5: Emission spectrum InAsP/InP nanowire quantum dot source:(a) A broad-band emission spectrum from a InAsP/InP QD nanowire quantum dot source when excited at 632 nm. The emission at 830 nm corresponds to the wutzite InP nanowire and the emission lines at 895 blongs to the QD s-shell emissions. (b) A high resolution spectrum of the zoomed in region of (a) indicated by dotted box. The three emission lines exciton (X), biexciton (XX) and charged exciton (X^{-}) corresponds to the InAsP QD s-shell emission

between the different shells of conduction and valance band are shown schematically by an arrow. In Fig. 2.5 (a) we show a typical emission spectrum from a InP/InAsP QD nanowire quantum dot source when it is excited by continuous HeNe laser at 632 nm. The emission peak at 830 nm corresponds to the wurtzite InP nanowire bandgap transition [29], while emission peaks around 895 nm are from InAsP s-shell (ground state) transitions. In Fig. 2.5 (b) we show the high-resolution spectrum of the zoomed-in region of Fig. 2.5 (a),

shown by the dotted box. The three emission lines are for exciton (X), biexciton (XX), and the charged negative exciton (X^-) respectively. A standard way of identifying the emission lines is by performing power and polarization-dependent measurements. The exciton and biexciton has a linear and quadratic dependence on an excitation power respectively, while the charged exciton has no dependence on the linear polarization, unlike exciton and biexciton transitions.

2.3 Biexciton-Exciton Cascade

The energy shells in the conduction and valance band can accommodate two carriers each, of an opposite spin. These charge carriers interact with each other via Coulombic interaction's and emits photons when electron-hole recombination takes place . The conduction band electron and valance band hole forms the bound state of a quasi-particle known as excitons, $|X\rangle$. In this way, quantum dot can be thought of as a hydrogen-like artificial atom with exciton $|X\rangle$ as an excited state. The ground state transitions for the quantum dot will be between conduction band electrons, $j_z \in \{+\frac{1}{2}(\uparrow), -\frac{1}{2}(\downarrow)\}$ and valance band heavy-holes, $j_z \in \{+\frac{3}{2}(\Uparrow), -\frac{3}{2}(\Downarrow)\}$. The four possible exciton states can be written as,

$$\begin{aligned}
|+1\rangle &= |\downarrow\Uparrow\rangle = \left|-\frac{1}{2}\right\rangle_e + \left|+\frac{3}{2}\right\rangle_h \\
|-1\rangle &= |\uparrow\Downarrow\rangle = \left|+\frac{1}{2}\right\rangle_e + \left|-\frac{3}{2}\right\rangle_h \\
|+2\rangle &= |\uparrow\Uparrow\rangle = \left|+\frac{1}{2}\right\rangle_e + \left|+\frac{3}{2}\right\rangle_h \\
|-2\rangle &= |\downarrow\Downarrow\rangle = \left|-\frac{1}{2}\right\rangle_e + \left|-\frac{3}{2}\right\rangle_h
\end{aligned} \tag{2.3}$$

According, to the optical selection rule from equation. 2.2, only two states $|+1\rangle, |-1\rangle$,

out of these four state can lead to the emission of photons, these are called *bright* states. The remaining states, $|+2\rangle, |-2\rangle$ are optically forbidden and are called *dark* excitons.

The recombination process in the s-shell will start with the two electrons in the conduction band and two holes in the valance band, this state is called the bi-exciton state, $|XX\rangle$. This process will be followed by the recombination of the remaining exciton, $|X\rangle$. The energies of the emitted bi-exciton (E_{XX}) and exciton (E_X) photons can be written in terms of the free particle energies (E_e, E_h) and the coulombic interactions (V_{ee}, V_{eh}, V_{hh}) between the electrons and holes states as the following,

$$E_X = E_e + E_h - V_{eh} \tag{2.4}$$

$$E_{XX} = 2E_e + 2E_h + V_{ee} + V_{hh} - 2V_{eh} \tag{2.5}$$

The coulombic interaction can be represented in a general form for any two states as,

$$V_{ij} = \frac{e^2}{4\pi\epsilon} \langle\psi_i\psi_j| \frac{1}{r_i - r_j} |\psi_i\psi_j\rangle \tag{2.6}$$

In general, the hole is much more bound due to its heavier mass. Hence, $V_{hh} > V_{eh} > V_{ee}$ from equation. 2.6. The difference between the energies of biexciton and exciton ($E_{XX} - E_X$) photons is known as biexciton binding energy. The biexcition binding energy can be positive or negative depending on the sign of the term, $V_{ee} + V_{hh} - 2V_{eh}$. Therefore, a quantum dot can have a biexciton photon at a higher as well as lower energy than the exciton photon.

The sequence of biexciton-exciton cascade will be,

$$|XX\rangle \rightarrow |X\rangle \rightarrow |00\rangle \tag{2.7}$$

This two-step process is shown schematically in the figure. 2.6. There are two possible paths for this cascade. The $|XX\rangle$ photon can be right circularly polarised ($j_z = +1$) or

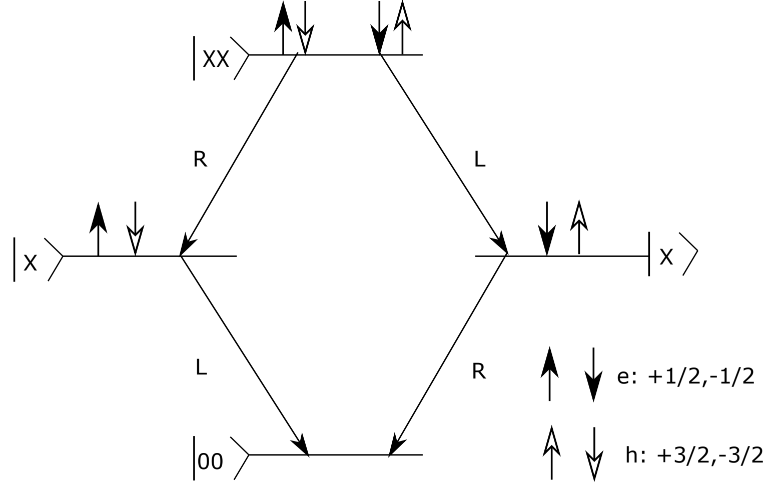

Figure 2.6: Biexciton-Exciton Cascade: The recombination process will take place through one of the two indistinguishable paths shown in the figure, depending on which pair of e-h recombines first. The final cascade state, $\frac{1}{2}(|RL\rangle + |LR\rangle)$, will be a superposition of these two paths.

left circularly polarised ($j_z = +1$) depending on the angular momentum of the exciton that recombines first. The remaining exciton will then subsequently recombine to emit the photon with an orthogonal polarization to the biexciton photon. Since there is no way to know which exciton will recombine first, these two paths are indistinguishable to each other and will emit the pairs of polarization-entangled photons [14], with the following quantum state,

$$|\psi\rangle = \frac{1}{2}(|RL\rangle + |LR\rangle) \tag{2.8}$$

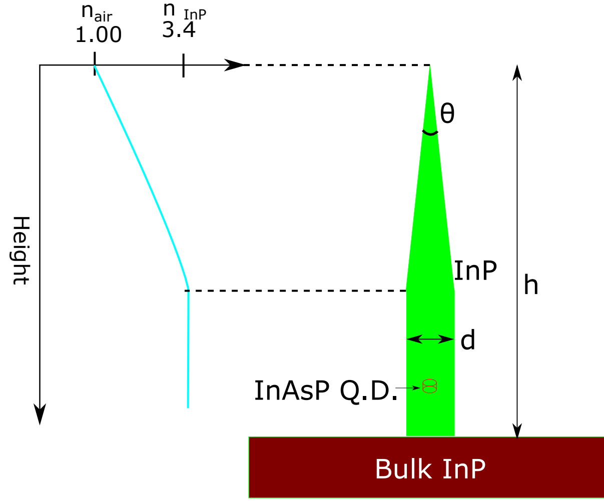

Figure 2.7: Sketch of a typical InP/InAsP nanowire quantum dot source: InP nanowire height h, diameter d and a tapering angle θ. A plot on the left maps the effective refractive index of the InP nanowire as function of its height from its top.

2.4 Nanowire as a waveguide

The InP nanowire not only provides the confining potential for electron and hole, but it also acts as a waveguide for the emitted photon when electron-hole recombination takes place. A conventional self-assembled QD suffer from low collection efficiency due to the isotropic emission profile of photons. The tapered nanowire geometry of the nanowire quantum dot source as shown in Fig. 2.7, overcome this problem by coupling the quantum dot emission to the fundamental waveguide mode of the nanowire and its tapered geometry at the top suppress the total-internal reflection at the semiconductor-air interface [28, 55].

These sources are fabricated through the VLS chemical beam epitaxy method (bottom-up approach)[29] [58]. The site selected growth allows the precise control over the quantum dot geometry and its placement on the axis of nanowire. Therefore, the optimal design,

couples the quantum dot emission to the fundamental mode HE_{11} of the cylindrical InP waveguide. Hence, the spontaneous emission rate Γ_{11} should be maximized into HE_{11} mode relative to the other higher order emission modes Γ', γ a non guided modes 'leaky' and the γ_{nr} non radiative modes. The β_{11} factor quantifies this,

$$\beta_{11} = \frac{\Gamma_{11}}{\Gamma_{11} + \Gamma' + \gamma + \gamma_{nr}} \tag{2.9}$$

The diameter 'd' of the nanowire waveguide as shown in Fig. 2.7 is optimized to reduce the Γ' and γ. For, λ =950 nm, the value of β is $\approx$ 0.90 for 0.20 $<d/\lambda>$0.30 [59]. This way an optimized nanowire cavity can be designed for any quantum dot emission. The gradual tapering of the nanowire ensures that the effective refractive index of the nanowire reduces gradually as the emitted photons travel to the top of the nanowire, as shown in the plot in Fig. 2.7.

2.5 Anisotropic exchange interaction: FSS

Anisotropic exchange interaction couples the spin of electron and hole and removes the degeneracy of the exciton state. This is known as fine structure splitting (FSS). Its value ranges from a few μeV to hundreds of μeV. If this energy splitting exceeds the exciton line-width (1 μeV), which-path information is revealed in the Biexciton- Exciton cascade which degrades the measured entanglement fidelity [60].

The e-h exchange interaction is proportional to the following integral [13],

$$\delta_{ex} = \int \int d^3 r_e d^3 r_h \Psi_X^*(r_e, r_h) \frac{1}{|r_e - r_h|} \Psi_X(r_h, r_e), \tag{2.10}$$

where Ψ_X is the exciton wavefunction and r_e/r_h are the position vector of electron and hole. This exchange integral can be divided into two parts short and long-range interactions.

The short-range interaction accounts for the interaction between electron and hole in the same Wigner-Seitz unit cell. This term is dependent on the symmetry of quantum dot at the atomistic scale i.e. crystal symmetry. Whereas, the long-range interaction term accounts for the contributions from electron-hole interaction when they are in a different Wigner- Seitz unit cells. This term is dependent on the microscopic properties of quantum dot i.e. shape, geometry.

The Hamiltonian for the short range interaction can be written as following [13],

$$H_{exchange} = -(\sum_{i=x,y,z} a_i J_{h,i} S_{e,i} + b_i J_{h,i}^3 S_{e,i}), \tag{2.11}$$

where, a_i and b_i are the coupling constant for electron and hole spin ($S_{e,i}$, $J_{e,i}$) along the three dimensions (i = x,y,z). The z direction is considered to be the growth direction of quantum dot. In III-V quantum dot electron at the conduction band minima has a total angular momentum of 1/2. While, the hole at the valance band minima has a total angular momentum of 3/2. Thus, by substituting the Pauli spin 1/2 matrices $S_{e,x}$, $S_{e,y}$, $S_{e,z}$ for electron from Eq. 2.12,2.13,2.14 and 3/2 spin matrices $J_{h,x}$, $J_{h,y}$, $J_{h,z}$ for hole from Eq. 2.15,2.16,2.17 into the Hamiltonian in Eq.2.11 we can write the total Hamiltonian for short range interaction in a form of 8 X 8 matrix as given in Eq. 2.18.

$$S_{e,x} = \begin{bmatrix} 0 & 1/2 \\ 1/2 & 0 \end{bmatrix} \tag{2.12}$$

$$S_{e,y} = \begin{bmatrix} 0 & -i/2 \\ i/2 & 0 \end{bmatrix} \tag{2.13}$$

$$S_{e,z} = \begin{bmatrix} 1/2 & 0 \\ 0 & -1/2 \end{bmatrix} \tag{2.14}$$

$$J_{h,x} = \begin{bmatrix} 0 & \sqrt{3}/2 & 0 & 0 \\ \sqrt{3}/2 & 0 & 1 & 0 \\ 0 & 1 & 0 & \sqrt{3}/2 \\ 0 & 0 & 1\sqrt{3})/2 & 0 \end{bmatrix} \tag{2.15}$$

$$J_{h,y} = \begin{bmatrix} 0 & -i\sqrt{3}/2 & 0 & 0 \\ i\sqrt{3}/2 & 0 & -i & 0 \\ 0 & i & 0 & -i\sqrt{3}/2 \\ 0 & 0 & i\sqrt{3})/2 & 0 \end{bmatrix} \tag{2.16}$$

$$J_{h,z} = \begin{bmatrix} 3/2 & 0 & 0 & 0 \\ 0 & 1/2 & 0 & 0 \\ 0 & 0 & -1/2 & 0 \\ 0 & 0 & 0 & -3/2 \end{bmatrix} \tag{2.17}$$

$$H_{exchange} = \begin{pmatrix} -3a_z/4 - 27b_z/16 & \cdots & \cdots & -3b_x/8 - 3b_y/8 \\ \vdots & \ddots & & \vdots \\ \vdots & \ddots & \ddots & \vdots \\ -3b_x/8 - 3b_y/8 & \cdots & \cdots & 3a_z/4 + 27b_z/16 \end{pmatrix} 8 \times 8 \tag{2.18}$$

This 8 X 8 matrix for exchange Hamiltonian gives the transition probability for all the possible transitions between spin 1/2 electron and spin 3/2 hole. However, due to the heavy-hole ($J_h, z = \pm 3/2$) and light-hole ($J_h, z = \pm 1/2$) splitting that ranges between few to tens of meV we can neglect the light-hole transitions. The single particle states for electron ($S_e = 1/2, S_{e,z} = \pm 1/2$) and heavy-hole ($J_h = 3/2, J_{h,z} = \pm 3/2$) are then used to construct exciton wave functions. These states are then coupled together to give a total

angular momentum $|M| = S_{e,z} + J_{h,z}$ for the exciton states. Exciton states with $|M| = 2$ cannot couple to the optical field and are known as dark states (dark exciton). The excitons with $|M| = 1$ are optically active (bright-exciton). Therefore, by neglecting light hole transitions and by considering only the following basis $(|1\rangle, |-1\rangle, |2\rangle, |-2\rangle)$ for exciton we can re-write the Hamiltonian for exchange interaction as sub-block of 4 X 4 matrix as the following,

$$H_{exchange} = \frac{1}{2}\begin{bmatrix} \delta_0 & \delta_1 & 0 & 0 \\ \delta_1 & \delta_0 & 0 & 0 \\ 0 & 0 & -\delta_0 & \delta_2 \\ 0 & 0 & \delta_2 & -\delta_0 \end{bmatrix} \tag{2.19}$$

where, $\delta_0 = 1.15(a_z + 2.25b_z)$, $\delta_1 = 0.75(b_x - b_y)$ and $\delta_2 = 0.75(b_x + b_y)$. The diagonal term of this matrix δ_0, is the energy splitting between bright and dark state. The off-diagonal terms δ_1 and δ_2 are responsible for the mixing of bright and dark states as well as the mixing of these states within themselves. For quantum dot with high symmetry (D_{2d}) $b_x = b_y$ and $\delta_1 = 0$, for such quantum dots the eigen states for the bright excitons are $|1\rangle$ and $|-1\rangle$. However, quantum dots with lower symmetry than D_{2d} like C_{nv} group has $\delta_1 \neq 0$, then the eigen states of bright excitons are the mixed states:

$$|+\rangle = \frac{1}{\sqrt{2}}(|+\rangle + |-\rangle) \tag{2.20}$$

$$|-\rangle = \frac{1}{\sqrt{2}}(|+\rangle - |-\rangle) \tag{2.21}$$

with, the energy $E_+ = \frac{1}{2}\delta_0 + \frac{1}{2}\delta_1$ and $E_- = \frac{1}{2}\delta_0 - \frac{1}{2}\delta_1$. The long-range interaction(γ_0) only contributes to the bright exciton. It increases the splitting of two bright states ($\Delta_0 = \delta + \gamma_0$) as well as its mixing ($\Delta_1 = \delta_1 + \gamma_0$). The sub-block of the Hamiltonian for the

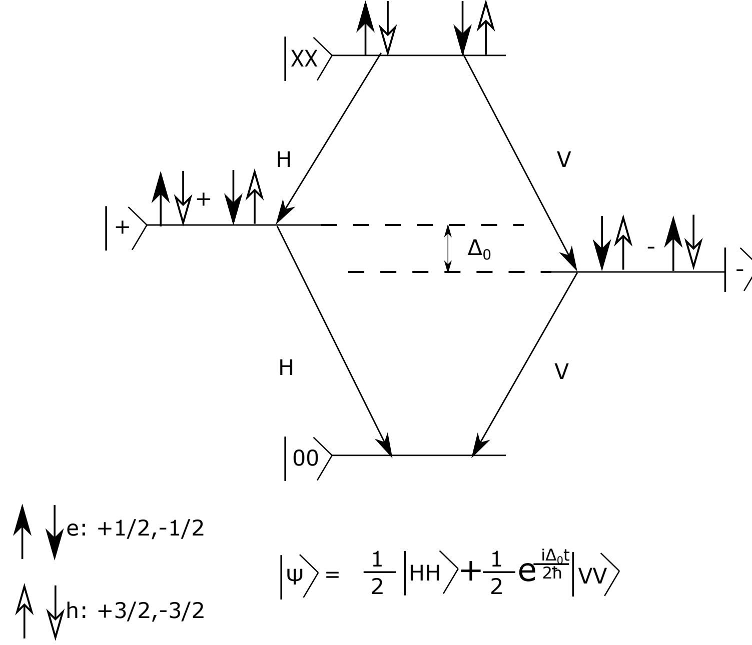

Figure 2.8: Biexciton-exciton cascade with a FSS energy splitting Δ_0: The eigenstate of the bright exciton states are linearly polarised due to the finite energy splitting in its intermediate exciton states. The final state will be $\frac{1}{2}|HH\rangle + \frac{1}{2}e^{\frac{i\Delta_0 t}{2\hbar}}|VV\rangle$

bright exciton state $|1\rangle$ and $|-1\rangle$ with both short range and long range can be written as,

$$H_{exchange} = \frac{1}{2}\begin{bmatrix}\Delta_0 & \Delta_1 \\ \Delta_1 & \Delta_0\end{bmatrix} \tag{2.22}$$

In Fig. 2.8 we draw the two paths for biexciton-exciton cascade when the two linearly polarized bright exciton states ($|+\rangle, |-\rangle$) are split in energy due to the electron-hole exchange interaction term Δ_0 known as the FSS. The contribution of the long-range interaction is much more than the short-range since $\gamma_0 \gg \delta_0$. It depends on the macroscopic properties of a quantum dot and is discussed in more detail in the next chapter section. 3.2

Chapter 3

Proposal for an electrically gated nanowire quantum dot device

3.1 Proposed electrical device

In this chapter, we propose a novel electric device that can erase the fine structure splitting of a quantum dot by applying a quadrupole electric field. The device architecture is shown schematically in Fig. 3.1. It consists of four metal gates aligned along the plane of quantum dot embedded inside the vertically standing tapered nanowire. Tapered nanowire allows for a high extraction efficiency of the emitted photons and the four metal gates are used to apply the quadrupole electric field to erase the fine structure splitting for any in-plane quantum dot orientation without compromising the electron-hole (e-h) overlap. Maintaining this strong e-h overlap in a quadrupole field is in stark contrast to previous electric field implementations to remove the FSS. In previous works, application of a lateral electric field resulted in the reduction of e-h overlap and a lower brightness of the quantum

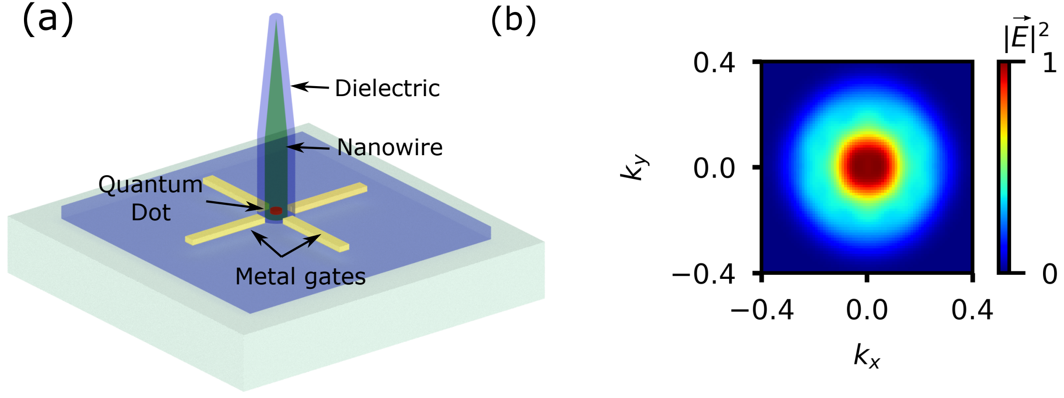

Figure 3.1: Device design: (a) Schematic view of the proposed device architecture consisting of a single quantum dot in a standing nanowire, dielectric coating and four electrical contacts in-plane of the quantum dot. (b) Calculated far-field emission profile from the device using a finite-difference time-domain method in Lumerical, assuming an in-plane dipole on the nanowire waveguide axis.

dot [61, 62, 63, 64]. A thin dielectric layer assist in electrically isolating the metal gates as well as bringing them to the plane of the quantum dot that is located few 100 of nm from the bottom of nanowire. To exhibit the high light extraction efficiency of our proposed device, we show the calculated far-field emission profile in 3.1 (b). This emission profile fits to a 2D Gaussian with near-unity overlap ($R^2 = 99.6$), thus demonstrating that the far-field emission profile is not altered by the gates. The light extraction efficiency for the device is calculated to be 35 %, which can be tailored towards unity by optimizing the device architecture including the nanowire shape, removing the dielectric and integrating a gold mirror at the nanowire base [65, 66].

3.2 Theory for calculating the FSS

We now present the underlying theory for calculating the FSS. The breaking of the quantum dot spatial symmetry causes the coupling of electrons and holes via the electron-hole exchange interaction [13]. The electron-hole exchange interaction can be decomposed into two parts: short-range (within the wigner-seitz cell) and long-range (outside the wigner-seitz cell) [13]. The FSS is mainly determined by the long-range exchange interaction term[67],

$$\begin{aligned}\delta = &\int\int d^3r_1 d^3r_2([\phi_0^h(\vec{r_2})u_{v\Downarrow}(\vec{r_2})]^*[\phi_0^e(\vec{r_2})u_{c\uparrow}(\vec{r_2})])^* \\ &\times\frac{e^2}{4\pi\epsilon\epsilon_0|\vec{r_1}-\vec{r_2}|}([\phi_0^h(\vec{r_1})u_{v\Uparrow}\phi_0^e(\vec{r_1})]^*[\phi_0^e(\vec{r_1})u_{c\downarrow}(\vec{r_1})]),\end{aligned} \tag{3.1}$$

where $\phi_0^e(\vec{r_i})$, $\phi_0^h(\vec{r_i})$ are the wavefunctions for the lowest electron and hole orbitals as a function of position, $\vec{r_i}$. The Bloch functions of the conduction and valance band are u_{cs_z},u_{vj_z}, respectively, with the spin of the electron ($s_z = +1/2$ ($\uparrow$), $-1/2$ ($\downarrow$)) and heavy-hole ($j_z = +3/2$ ($\Uparrow$), $-3/2$ ($\Downarrow$)) resulting in two bright excitonic states of total angular momentum M $= +1(\downarrow,\Uparrow)$ and M $= -1(\uparrow,\Downarrow)$. To carry out this calculation, we assume a 3D asymmetric parabolic quantum dot potential. In such a model, the ground state electron and heavy-hole wavefunctions can be modeled by a Gaussian, $\phi_0^{e/h}(\vec{r}) = (\frac{1}{\pi^{3/2}l_x^{e/h}l_y^{e/h}l_z^{e/h}})^{1/2}exp\{-\frac{1}{2}[(\frac{x}{l_x^{e/h}})^2+(\frac{y}{l_y^{e/h}})^2+(\frac{z}{l_z^{e/h}})^2]\}$. Equation 3.1 is solved analytically, giving FSS in terms of the relevant material properties, wavefunctions and quantum dot geometry by the relation[67],

$$\delta = K\cdot\beta\cdot\xi(1-\xi)\cdot\frac{\gamma_z}{(l_y^{eh})^3}, \tag{3.2}$$

where $FSS = 2|\delta|$; $K = \frac{3\sqrt{\pi}e^2\hbar^2 E_p}{(4\pi\epsilon_0)16\sqrt{2}\epsilon m_0(E_g^b)^2}$, is a constant and is dependent on the quantum dot material properties where E_p and E_g^b are the conduction-valence band interaction energy and bulk energy gap, respectively, and m_0 is the free electron mass; β is the e-h wavefunction overlap ($\beta = |\langle\Psi_h|\Psi_e\rangle|^2$) where Ψ_e and Ψ_h are ground state electron and heavy-hole wavefunctions; $\xi = \frac{l_y^{eh}}{l_x^{eh}}$ characterizes the hybridized wavefunction elongation [68]; and the length parameters $l_{x,y}^{eh}$ are the spatial extents of the hybridized e-h wavefunction ($\Psi_{eh} = \Psi_h\Psi_e$) along the x- and y-axis of the quantum dot; and γ_z is the parameter for z confinement. For a quantum dot where the height is much less than its diameter (*i.e.*, $d_z << d_{x,y}$), the parameter for z confinement (γ_z) equals one.

This analytical expression implies that there are two main strategies to minimize the FSS. The first approach is to reduce the e-h overlap (*i.e.*, β) and the second strategy is to make the exciton wavefunction symmetric (*i.e.*, tune ξ to 1). However, reducing β will affect the quantum dot brightness since it minimizes the recombination probability of the bright exciton state [62]. Hence, the favorable strategy involves the tuning of ξ without compromising the e-h overlap, β.

3.3 Numerical Simulation

We have performed numerical simulations and calculated the FSS for a GaAs quantum dot with dot diameter of 30 nm and dot height of 3 nm. The dot is embedded in an $Al_{0.33}Ga_{0.67}As$ nanowire shell (thickness of 110 nm), which is surrounded by an Al_2O_3 dielectric layer (thickness of 150 nm). Finally, four gold electrical contacts (width of 200 nm) are defined in the plane of the quantum dot to apply a quadrupole electric potential. Refer to Fig.3.1(a) for a schematic view of the proposed device architecture.

To demonstrate that the proposed device allows for FSS correction without compromising

QD	E_g^b (eV)	E_p (eV)	m_e^* (m_o)	m_{hh}^* (m_o)	ϵ
GaAs	1.519	23	0.067	0.5	12.5
$InAs_{0.25}P_{0.75}$	1.20	20.92	0.061	0.533	14.05

Table 3.1: Material parameters for GaAs and $InAs_{0.25}P_{0.75}$ quantum dot

the quantum dot brightness, we have performed a numerical simulation using nextnano [69] to solve the two-dimensional Schrödinger-Poisson equation self-consistently using an effective mass approximation (refer Appendix B.1). The material parameters used for the GaAs quantum dot is listed in Table. 3.1. In our calculations, we assume the ground state is pure heavy-hole. This assumption is in-line with previous theoretical and experimental results [70, 71] where the ground state is dominantly heavy-hole. Ignoring the third dimension is justified for strong confinement ($\gamma_z = 1$), where the dot height is much less than its diameter (*i.e.*, $d_z << d_{x,y}$). In our simple model, we only consider the geometric quantum dot asymmetry as this is typically the dominant source of FSS [72]. Thus, we have modified the quantum dot shape from a circle to an ellipse with 7% elongation along the major axis (*i.e.*, $L_x/L_y = 1.07$). The ground-state electron and heavy-hole wavefunctions are then computed from the solution of the two-dimensional Schrödinger-Poisson equation from which we calculate the hybridized e-h wavefunction. Using equation 3.2, we then calculate the FSS. For this quantum dot elongation of 7%, the calculated FSS is 11 μeV, which is typical for quantum dots.

Fig. 3.2 (a) and (e) show a schematic view of the applied quadrupole electric potential for two different configurations. Configuration 3.3 (a) corresponds to a positive potential applied to the top and bottom gates, and a negative potential with the same magnitude applied to the left and right gates, while it's the opposite for configuration 3.2 (e). Here, the solid blue and dashed red ellipses represent the single particle wavefunctions of the

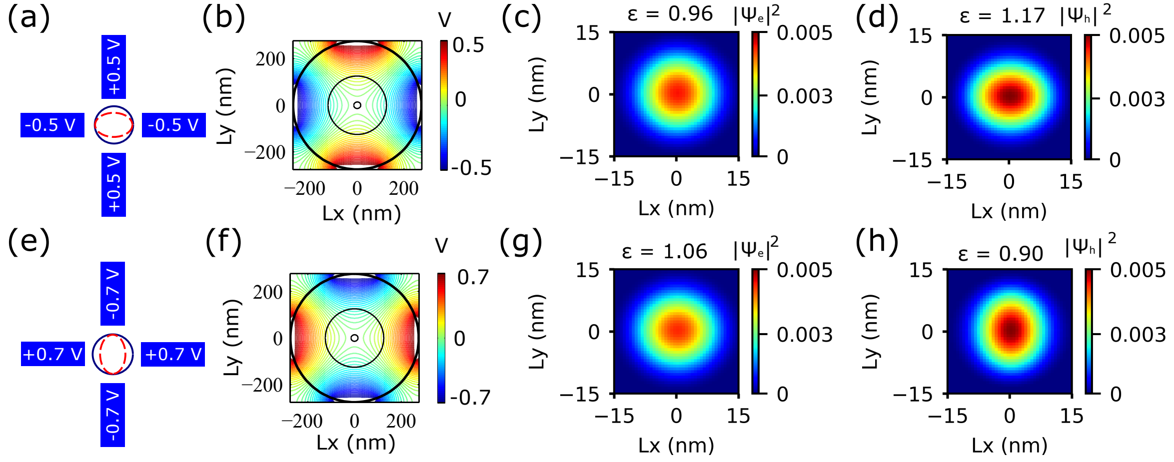

Figure 3.2: Single particle wavefunctions with an applied quadrupole field: (a) Schematic view of applied quadrupole potential. We use the convention that the top and bottom gates are positive at +0.5 V and the left and right gates are negative at -0.5 V. The electron wavefunction is shown schematically in solid blue and hole wavefunction in dashed red. (b) Calculated 2D electric potential for configuration (a). The black circles represent the edges of the dielectric (largest), nanowire (medium), and quantum dot (smallest). (c),(d) Calculated 2D probability density of electron (c) and hole (d) wavefunctions with the configuration from (a). (e) Schematic view of applied quadrupole potential with polarities reversed with respect to (a) and magnitude increased to 0.7 V. (f) Calculated electric potential for configuration from (e). (g),(h) Calculated 2D probability density of electron (g) and hole (h) wavefunction with configuration from (e). Lx and Ly are the dimensions in the x and y direction of the simulated structure, whereas ϵ is the degree of single particle wavefunction elongation of the electron and hole.

electron and hole, respectively, under the applied electric potential. The potential profile is plotted for these two configurations from the solution of the Schrödinger-Poisson equation in Fig. 3.2 (b) and (f). The black circles represent the $GaAs$ quantum dot (smallest circle at center), $Al_{0.33}Ga_{0.67}As$ nanowire (middle circle), and the Al_2O_3 dielectric shell (largest

circle). The contour plot of the electric potential shows that it is zero inside of the quantum dot, which is essential for maintaining a strong e-h overlap of the bright exciton state.

Fig. 3.2 (c) and (d) show the 2D probability densities of the ground state electron ($|\Psi_e|^2$) and heavy-hole ($|\Psi_h|^2$), respectively, for the applied potential configuration from Fig. 3.2 (a). These plots have been fit with 2D Gaussian functions (refer Appendix B.2) to extract the standard deviations along their major (σ_x) and minor (σ_y) axes, and to obtain the single particle wavefunction elongation factor, $\epsilon = \sigma_x/\sigma_y$. We find that the hole wavefunction is stretched along the x-axis ($\epsilon = 1.17$) and is perturbed much more than the electron wavefunction which is slightly stretched along the y-axis ($\epsilon = 0.96$). In contrast, Fig. 3.2 (g) and (h) show the 2D probability densities of the electron and hole, respectively, for the applied potential configuration from Fig. 3.2 (e). These plots show an opposite trend to those in Fig. 3.2 (c) and (d): $|\Psi_h|^2$ is now spread along the y-axis ($\epsilon = 0.90$) instead of the x-axis and $|\Psi_e|^2$ is spread along the x-axis ($\epsilon = 1.06$) instead of the y-axis. The higher perturbation of the heavy-hole wavefunction is expected since heavy-holes are much more localized than electrons due to their larger effective mass.

3.4 Results

In Fig. 3.3 (a) we plot the calculated FSS (circles, left axis) as a function of the quadrupole potential (V), whereby a negative quadrupole potential of -0.5 V represents the configuration from Fig. 3.2 (a) and a positive quadrupole potential of +0.7 V represents the configuration from Fig. 3.2 (e). The trend demonstrates that the FSS can be tuned to zero by applying a quadrupole potential. The calculated e-h overlap for the quadrupole field is also shown in Fig. 3.3 (a), represented by stars (right axis). Remarkably, the quadrupole field maintains near-unity e-h overlap, with a value above 99 % over the entire range of

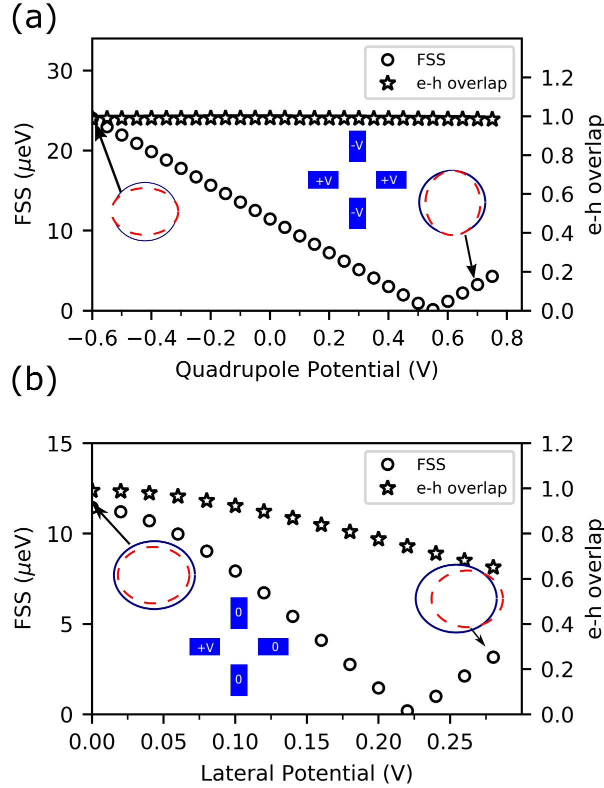

Figure 3.3: FSS as function of an external electric field:(a) Calculated FSS (circles, left axis) and e-h overlap (stars, right axis) as a function of quadrupole potential. (b) Calculated FSS (circles, left axis) and e-h overlap (stars, right axis) as a function of lateral potential. Insets: Schematic view of applied quadrupole (in (a)) and lateral potential (in (b)). The probability density of the electron (solid blue) and hole (dashed red) wavefunctions are schematically shown by the ellipses.

the applied field, thus conserving the quantum dot brightness. This desirable feature is in stark contrast to previous work where an applied lateral field was used and the e-h overlap had to be drastically reduced to remove the FSS [61, 62, 63, 64].

To directly compare the two approaches (quadrupole and lateral electric field), we

modeled the device under an applied lateral field with a positive potential on the left gate while keeping all other gates at zero potential (Fig. 3.3(b)). In this case, the FSS (circles, left axis) can be corrected for by applying V = 0.225 V, but the e-h overlap (stars, right axis) is reduced to 74 % at this potential (Fig. 3.3 (b)), thus compromising the quantum dot emission brightness. We re-emphasize that in the case of the lateral electric field the gates must be aligned along the quantum dot dipole orientation, otherwise the FSS cannot be removed.

The device architecture that we have modeled represents an ideal case where the four electrical gates are perfectly aligned along the quantum dot dipole orientation. In practical devices; however, the quantum dot asymmetric axis is randomly oriented from dot to dot. Moreover, there is also the challenge of fabricating the device with the required precision. In such cases, the quantum dot asymmetry will be misaligned with respect to the electrical gates. To model this misalignment, we have simulated two additional dipole orientations with the quantum dot major axis oriented at an angle of $\theta = 10°$ and $\theta = 20°$ with respect to the gates along the x-axis (Fig. 3.4 (a)). Fig. 3.4 (b) shows the calculated FSS as a function of quadrupole potential for $\theta = 0°, 10°$ and $20°$. The minimum FSS is obtained for an applied quadrupole potential of V = 0.5 V (for $\theta = 10^0, 20^0$). Clearly, there exists a non-zero minimum bound to the FSS for $\theta = 10°$ and $\theta = 20°$, whereas the FSS can reach zero for $\theta = 0°$

To reduce the minimum bound of the FSS further when the quantum dot dipole orientation is not aligned with the electrical gates ($\theta = 20^0$), we modify the applied quadrupole potential by increasing the potential on the right gate by $\triangle V_{RL}$ and decreasing the potential on the bottom gate by $\triangle V_{TB}$. The calculated FSS is plotted as a function of $\triangle V_{RL}$ and $\triangle V_{TB}$ in Fig. 3.4 (c). In Fig. 3.4 (d) we zoom into the region of the white dotted box of Fig. 3.4(c) and find near-zero FSS (0.05 μeV) at $\triangle V_{RL} = 0.095$ V and $\triangle V_{TB}$

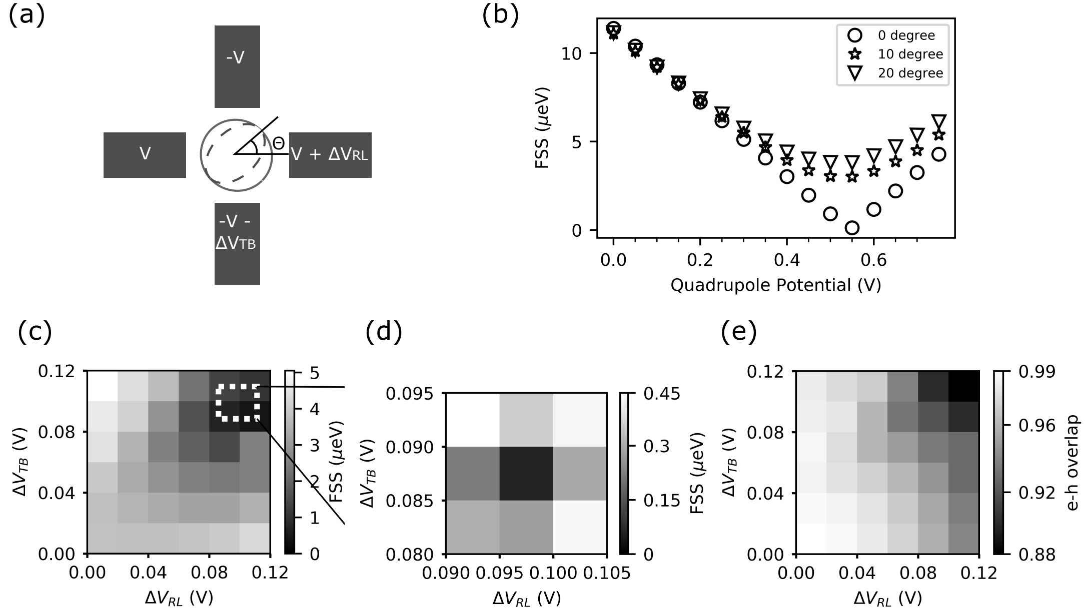

Figure 3.4: Universal FSS tuning: (a) Schematic view of an applied asymmetric quadrupole potential. Inset: electron (solid grey) and hole (dash grey) wavefunctions of a quantum dot with asymmetric axis aligned at an angle θ with respect to the gates along the x axis. (b) Calculated FSS as a function of quadrupole potential with the quantum dot major axis oriented at three different angles with respect to the gates along the x-axis ($\theta = 0°, 10°$, and $20°$). (c) Greyscale plot of FSS as a function of ΔV_{RL} and ΔV_{TB} for $\theta = 20^0$. (d) High resolution greyscale plot of the zoomed-in region (white dotted line box from (c)) showing near-zero FSS. (e) Greyscale plot of e-h overlap as a function of ΔV_{RL} and ΔV_{TB} for $\theta = 20^0$.

$= 0.085\,\text{V}$.

The e-h overlap is also plotted as a function of $\triangle V_{RL}$ and $\triangle V_{TB}$ in Fig. 3.4 (e). An overlap of 90% is obtained for the modified quadrupole potential near-zero FSS. This high e-h overlap with close to zero FSS is desired for a high-efficiency entangled photon source with near-unity fidelity.

In summary, we showed that an applied quadrupole field to a single quantum dot in a photonic nanowire results in zero FSS without compromising the quantum dot brightness. With our approach, we envision high-efficiency entangled photon sources with near-unity fidelity are within reach. Such sources are the missing building block of quantum networks and can also be used as a new source in quantum communication, quantum sensing, quantum optics, and integrated quantum optics on a chip.

Chapter 4

Fabrication of a gated vertical nanowire quantum dot device

In this chapter, we present the recipe to fabricate the vertically standing electrically gated InAsP/InP single nanowire device. Based on our theoretical proposal in chapter. 3, we have fabricated two generations of devices. First, is the device where metal gates are defined by UV lithography (resolution of 1 μm), and the four metal gates are separated by a few μm (3.5 μm). In the second generation of devices, metal gates are defined by e-beam lithography and we could bring them very close (100's of nm) to the nanowire sidewalls. Both the devices have a similar architecture to the device in figure 3.1, with an exception of a selective removal of a dielectric (SiO_2) from the top of the nanowire, for conserving the brightness and spectral properties of the QD. First, we will discuss the state of the art and challenges related to the fabrication of these devices. Then we will report, step by step fabrication recipes for both the devices.

4.1 Current state-of-the-art and challenges

The fabrication of vertical nanowire devices has been under development over the last few decades. Their application ranges from solar cells [73] to transistors [74] and FETs [75, 76]. Most of these fabrication recipes were developed for planar architecture devices, where the source and drain contacts were usually made by contacting the bottom of the substrate and the top of nanowires. However, most of the single nanowire devices are usually fabricated in horizontal geometry, where nanowire is transferred to an insulating chip carrier first and then the conventional lithographic techniques are employed to fabricate source, drain, and gates on a lying down nanowires. In our case, we are trying to apply the electric field in the plane of the quantum dot while simultaneously maintaining high extraction efficiency, this is a lot harder to obtain in a horizontal geometry unless we couple the quantum dot emission into an integrated waveguide [77]. Vertical geometry of the nanowire in our case offers a simple solution to this problem. This architecture also has the advantage of a smaller device footprint.

Fabricating a single nanowire vertical device has many challenges. Conventional lithographic techniques rely on a golden ratio between the photoresist thickness and the dimensions of features that have to be written by lithography. This becomes a major challenge with vertical single-nanowire devices due to its large aspect ratio. Therefore, we are limited in our choices of photoresist. Some of the main challenges related to our device fabrication are as follows:

- *Site-selected vertical quantum dot in nanowires* with required lengths and density is required. InAsP QD in a InP nanowires are grown on a lithographically defined pattern via VLS technique. The quantum dot has to be placed at the required height inside the nanowire.

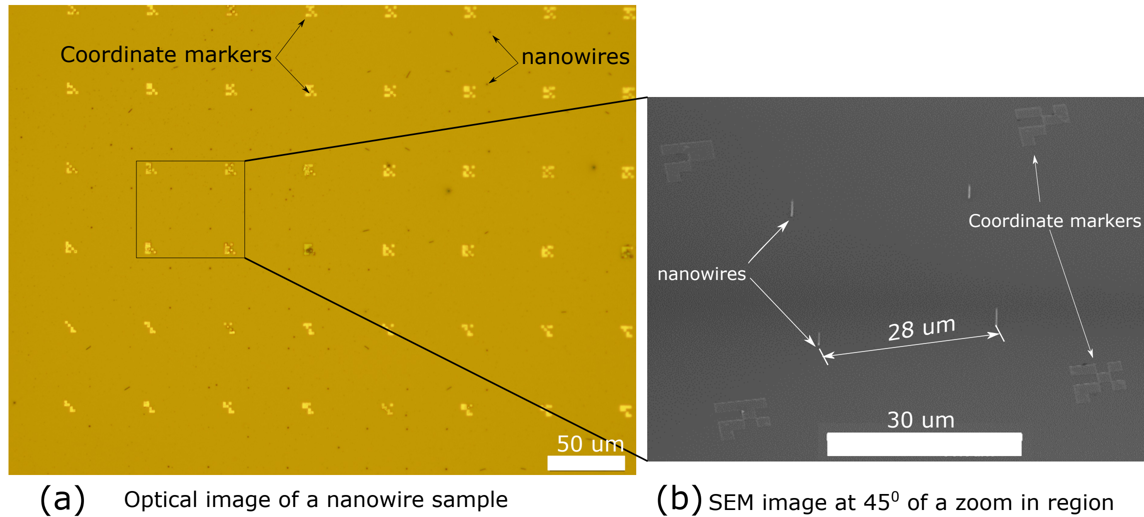

Figure 4.1: Nanowire sample image:(a) Optical image of the nanowire sample, nanowires are patterned in blocks with four nanowires in each block. (d) SEM image of one such block. Nanowires have a separation of 28 um. Gold micro-pattern pads give coordinates of every block in the form of binary rows and columns. The image is taken at 45 $^{\circ}$

- *Alignments of the gates* has to be done with respect to the single nanowires location and the plane of the QD. This alignment depends on the accuracy of the global/alignment markers on the chip. Any misalignment with respect to the alignment markers and the nanowire location has to be corrected before writing the final device.

- *Uniform photo/e-beam resist coverage* is required to protect the nanowire during the metal deposition and lift-off process. Due to the high aspect ratio of the nanowire, spin coating of the resist has to be uniform on the sidewalls of nanowires and the bottom of the substrate

- *Dielectric with good step-coverage* is necessary for the uniform deposition of the dielectric on the sidewalls and the bottom of the substrate. The quality and choice of

the dielectric material will dictate the break-in voltages of our devices.

- *Breaking down of nanowires during spin coating resist* is one of the major challenges we have faced in our fabrication processes. The bare vertical nanowire is very brittle and they break down on spin coating above the RPM of 3000/minute.

- *Processing temperature* is very crucial to preserving the quantum dot brightness. The desorption temperature of Arsenic in InAsP quantum dot is 400 °C. If this temperature is exceeded during the processing, the optical property of the QD is degraded.

- *Preserving optical quality of quantum dot* is fundamental to the final device performance. The dielectric deposition, spin coating processes, and lithography all affect the optical quality of quantum dot emission.

4.2 Step by step fabrication steps: UV lithography

In this section, we will present the different processing steps for the fabrication of a vertical nanowire device by UV lithography. The whole process can be divided into four steps and these steps are discussed in the following sections. The detailed recipe for each step can be found in Appendix A.1. We start our process with a site selected VLS grown InP nanowire on a chip as shown in an optical image in Fig. 4.1 (a), a SEM image of its zoomed-in region is shown in Fig. 4.1 (b). The InAsP QD is placed at 250 nm from the bottom of $\langle 111 \rangle$ InP wafer and the nanowires are grown in a block pattern with a separation of 28 μm.

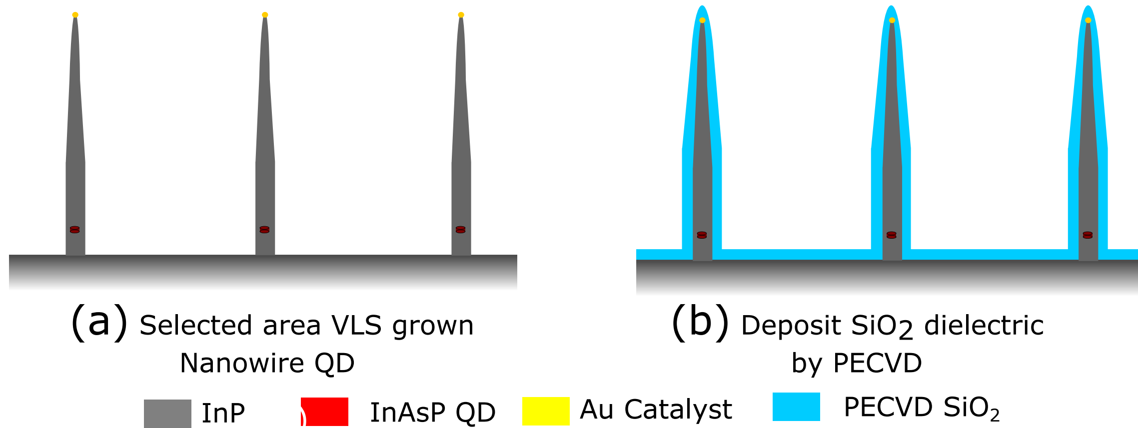

Figure 4.2: Schematic of dielectric deposition on the vertical nanowire: (a) Schematic depiction of a InP/InAsP nanowire/QD source. (b) After 200 nm of PECVD SiO_2 deposition. Different colors in the figures are explained in a legends below.

4.2.1 Dielectric Deposition

To avoid electric leakage between the metal gates, a thin film of the dielectric is deposited on an InP nanowire chip. InP nanowires are very brittle and therefore they break down during the processing steps, such as spin coating, lift-off, etc. A thin dielectric film, therefore, not only provides electric isolation but also provides mechanical stability to the nanowires. We deposit 200nm PECVD SiO_2 at a temperature of 330° C. A schematic of this process is shown in Fig. 4.2 (a) and (b). We choose a PECVD process, because it allows us to deposit a uniform film of a dielectric material within the allowed temperature window (below 400° C). However, the choice for dielectric was made due to the existence of a well-known recipe for obtaining a uniform and high-quality SiO_2 in our fabrication lab and its controlled BOE based wet etching recipe.

We also characterized the uniformity of SiO_2 on the sidewall of the nanowire by performing a controlled BOE wet etching as shown in Fig. 4.3. In this process, we first

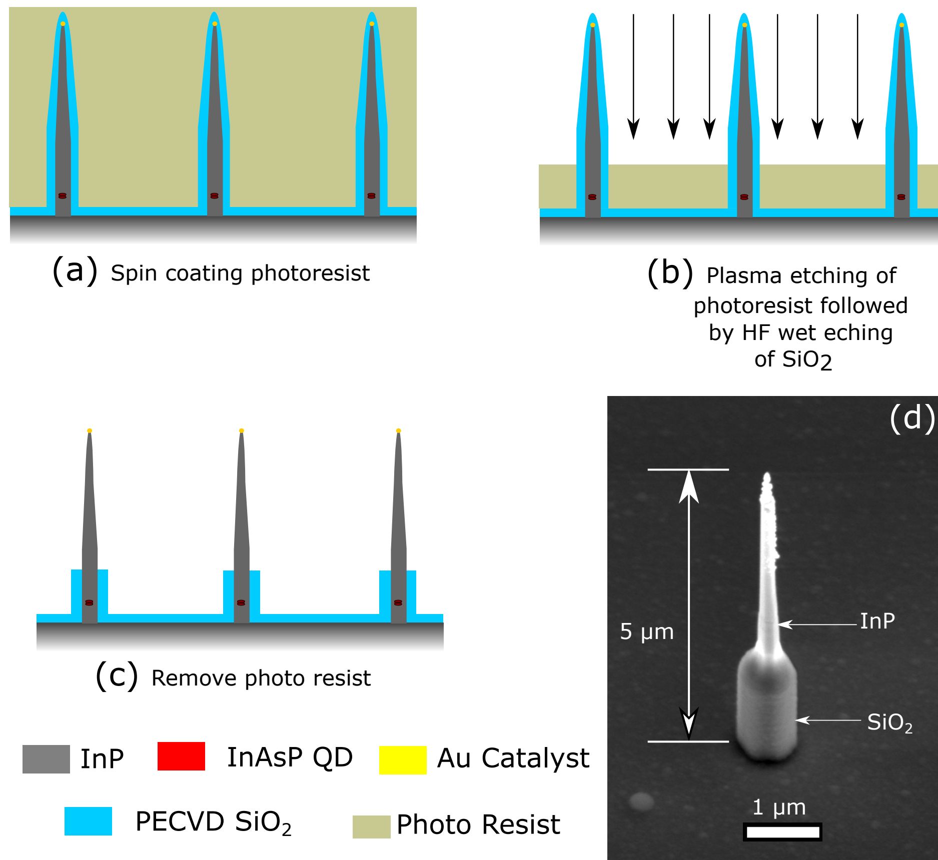

Figure 4.3: Dielectric uniformity on the sidewalls of nanowires: The schematic cross-sectional illustration of a wet BOE etching the SiO_2 from the top of nanowire (a) Sample after the spin coating the photoresist. (b) Plasma dry etching to selectively thin down the photoresist, followed by dipping in the BOE solution for 1 minute. (c) Striping the photoresist. (d) A 45 ° SEM image of the nanowire after the processing. Different colors in the figures represent different materials and are explained in the legends below.

spin-coated the sample with a positive photoresist AZ400 that covers the nanowires, refer Fig. 4.3 (a). Then the photoresist is etched down by dry plasma etching, followed by a wet etching of exposed SiO_2 by BOE, refer Fig. 4.3 (b). In the final step, the photoresist is

removed by dipping the sample in a PG remover(Fig. 4.3 (c)) . A 45° SEM image of the nanowire after the process is shown in Fig. 4.3 (d). The nanowire's sidewall to the wafer step coverage $d_{sidewalls}/d_{wafer}$ is ≈ 0.8.

4.2.2 Selected area removal of dielectric

In this step, we selectively remove the dielectric from the top of nanowires. This is done by lithographically defining the opening in the mask of a positive photoresist (PMGI + S1805). The spin rate for each resist is carefully optimized to avoid the formation of side beads around the edge of the sample (1x1 cm). Subsequently, each layer is baked and its thickness is measured by Filmetric F-50 optical UV reflectometer set-up. Then, this PMGI (450 nm) and S1805 (500 nm) bi-layer is exposed to a pattern by a mask-less MLA 150 Heidelberg UV-lithography, Fig. 4.4 (a). Here, S1805 is the photosensitive resist while the PMGI layer assists in the metal lift-off process due to its undercut profile after the development. The alignment markers (metal-crosses) that were used to pattern nanowire growth are used for aligning the pattern for exposure around the nanowires. After this step, the photoresist is developed in an MF-319 solution, Fig. 4.4 (b) and a descum is performed to get rid of any residual resist. Any organic contamination or resist residual can affect the wet etching. Then the SiO_2 is wet etched by the BOE solution from the exposed area, Fig. 4.4 (c). Finally, the resist mask is removed by dipping the sample in a PG remover, Fig. 4.4 (d). In the figure, 4.4 (e) an optical image of the device is shown after all these steps.

4.2.3 Defining Gates

For defining the gates around the nanowires, the lithography steps are similar to the steps used for patterning the resist in section 4.2.2. It is shown schematically in Fig. 4.5

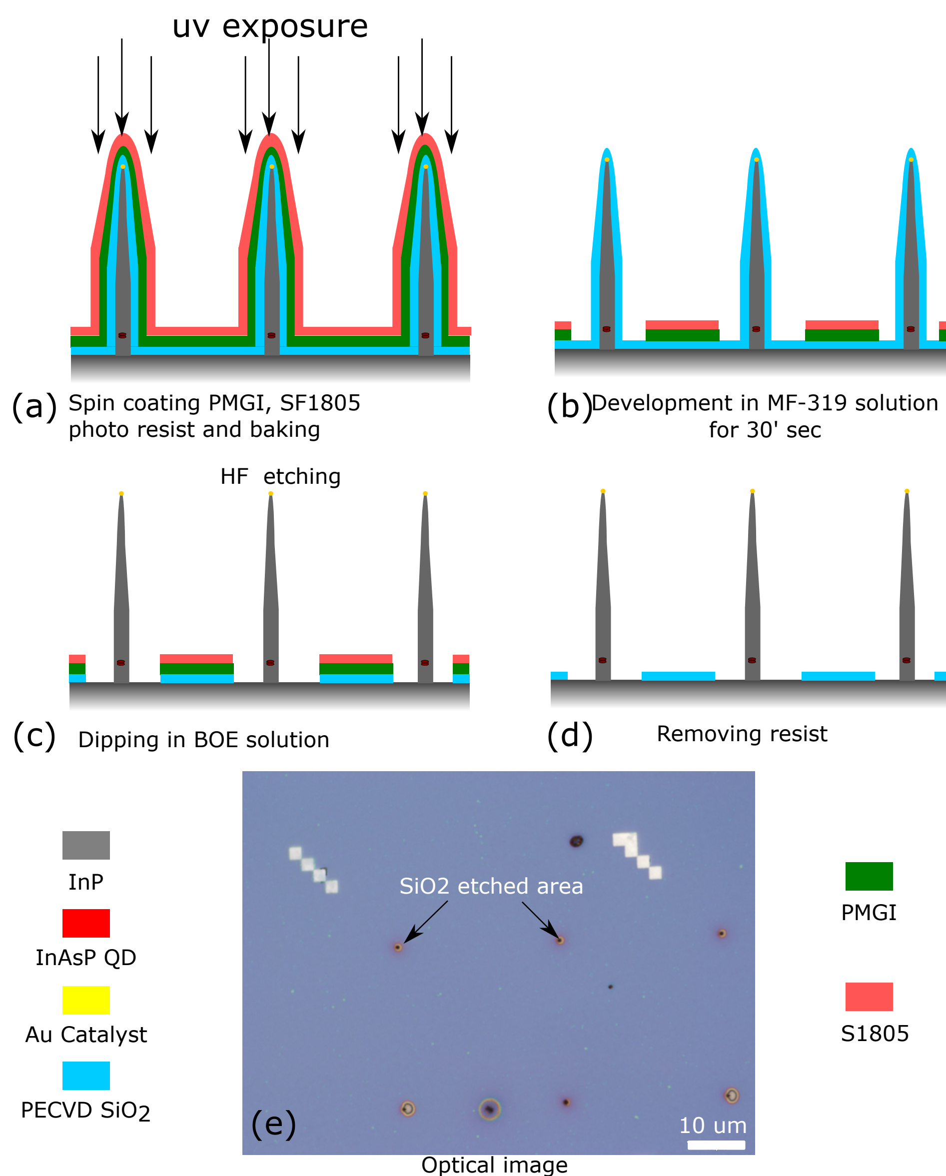

Figure 4.4: Steps for removing the dielectric from the nanowires: Schematic cross-sectional illustration of the mains steps for selectively removing the SiO_2, shown in the order (a)-(d). The different processes are explained in the texts. (e) Optical image of the device after step d. Different colors in the figures represent different materials and are explained in the legends below.

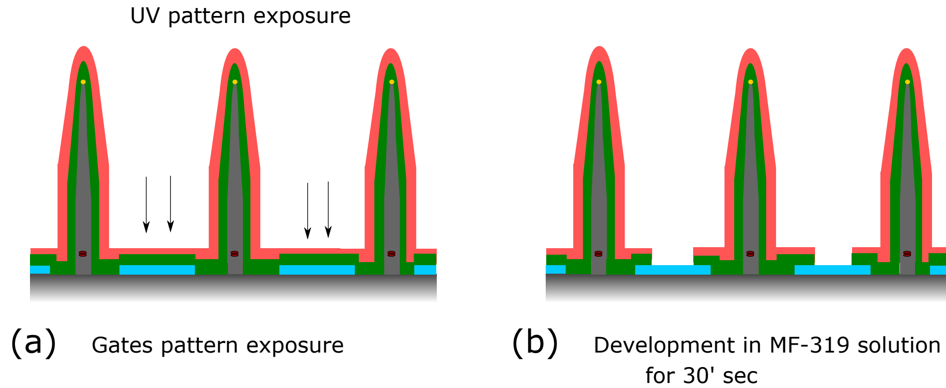

Figure 4.5: Defining gates: Schematic cross-sectional illustration of the mains steps for exposing an area of metal gates, shown in the order (a)-(b). The different processes are explained in the texts. Legends for different color can be found in figure 4.4

(a) and (b). Here, instead of exposing the nanowires, we expose an area where we want to deposit the metal gates. It is followed by the descum process to prepare the device for metal deposition and lift-off

4.2.4 Metal deposition and liftoff

In the final step we deposit a thin metal of Ti/Au 15 nm/80 nm by an e-beam thermal evaporator. A thin layer of Ti helps in improving the adhesion of an Au film. After this step, we do a lift-off process by dipping the device in a PG remover. PG remover dissolves the photoresist and the metal film from the unexposed area of the sample is lifted-off. It is shown schematically in the figure 4.6 (a) and (b). In figure 4.7 (c) we draw the schematic three dimensional figure of the final single nanowire device after the fabrication.

In Fig. 4.7 (a) we show an optical image (top-view) of the chip after the fabrication. The large area optical image of the chip shows multiple gated nanowires connected with micron-sized metal bond pads. Figure 4.7 (b) and (c) are the optical images of a zoomed-in

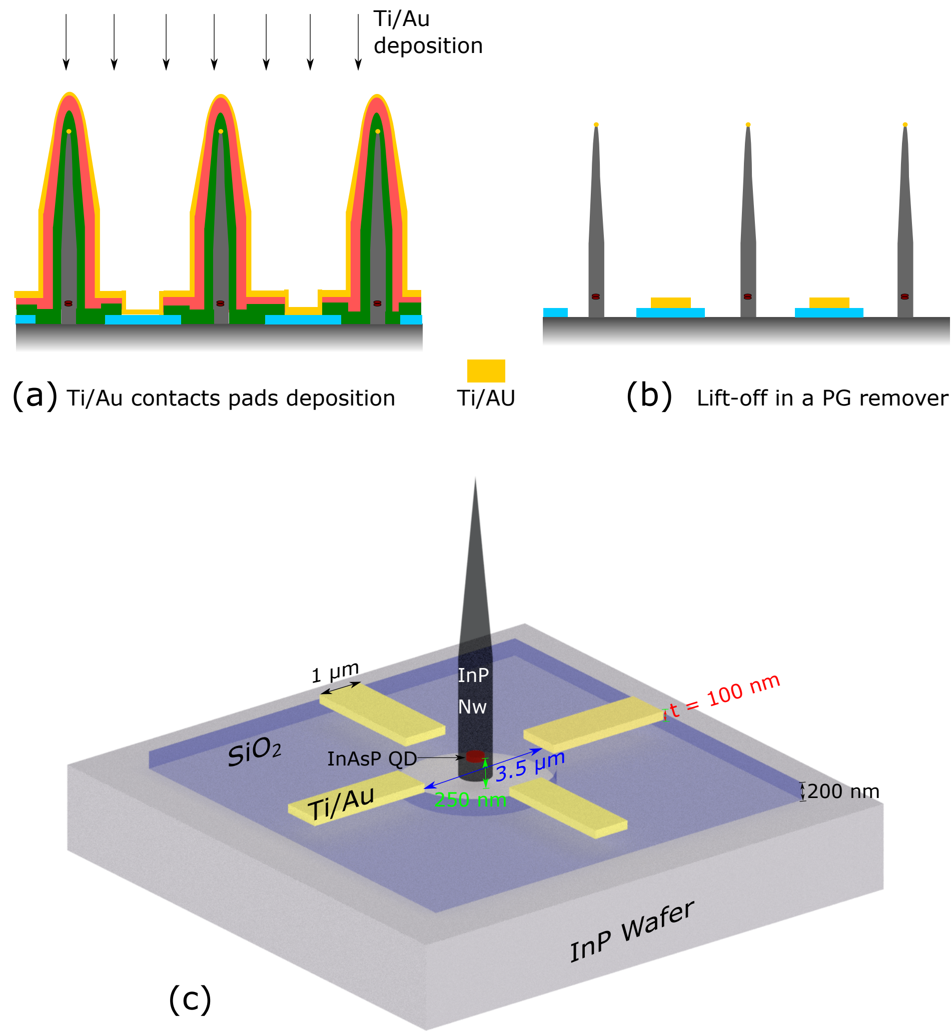

Figure 4.6: Metal deposition and lift-off: Schematic cross-sectional illustration of the mains steps of metal deposition and lift-off process (a)-(b). The different processes are explained in the texts. A schematic three-dimensional figure of a single nanowire device is shown in figure (c). Legends for different color other than Ti/Au can be found in figure 4.4

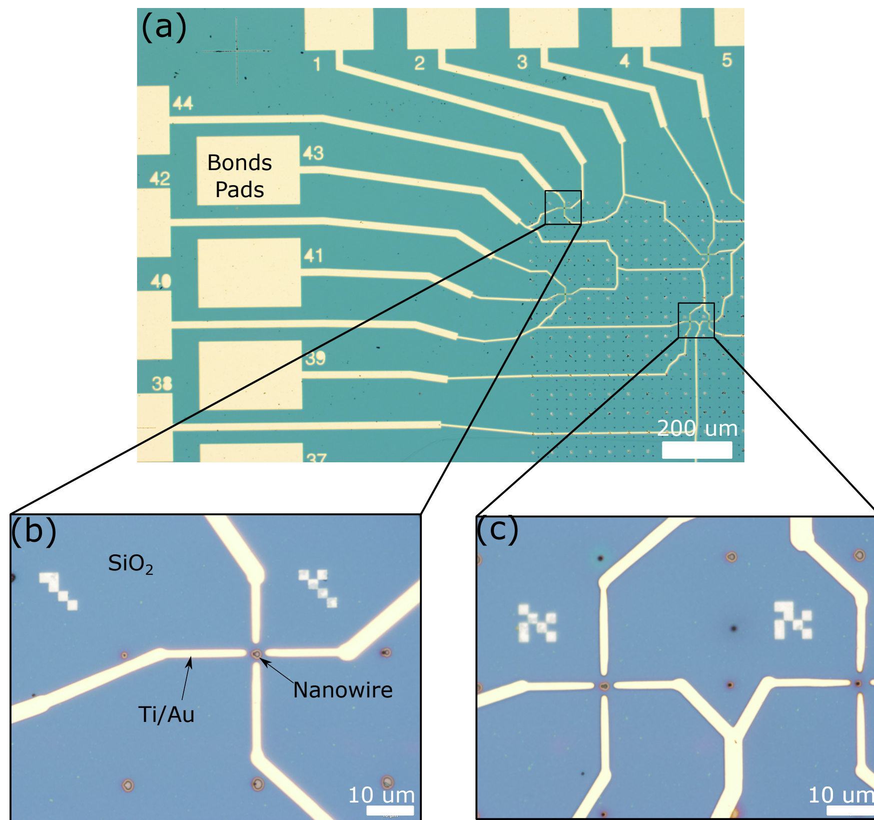

Figure 4.7: Optical image of the final device: (a) Top view of the final device. (b) and (c) are the zoomed-in images (regions shown by black boxes in (a)).

region shown by black boxes in Fig. 4.7 (a). It shows a single gated nanowire device. We have fabricated eight such single nanowire gated device on this chip.

4.3 Step by step fabrication steps: E-Beam lithography

In this section, we will present a step by step fabrication steps for a InAsP/InP vertical nanowire gated device by an e-beam lithography. We again start with a site selected VLS grown nanowires, refer image 4.1 (a), (b) and the main process can be divided into four steps. However, instead of selectively removing SiO_2 first and then fabricating metal gates, we changed our approach to fabricating metal gates first and then selectively removing the SiO_2 in the last step. We made this change in our approach to avoid the breaking down of InP nanowires during spin coating and metal lift-off steps. By selectively removing the SiO_2 in the last step, we avoided performing any spin-coating or lift-off process on the bare InP nanowires and therefore it increases the yield of our devices. The details recipe for each step can be found in Appendix A.2.

4.3.1 Dielectric Deposition

The SiO_2 deposition steps and recipe is same as described in the section 4.2.1

4.3.2 Defining Gates

In this step, we lithographically define an opening in the e-beam positive resist mask by exposing it to a pattern of 100 kV e-beam and then developing it in chilled water co-solvent

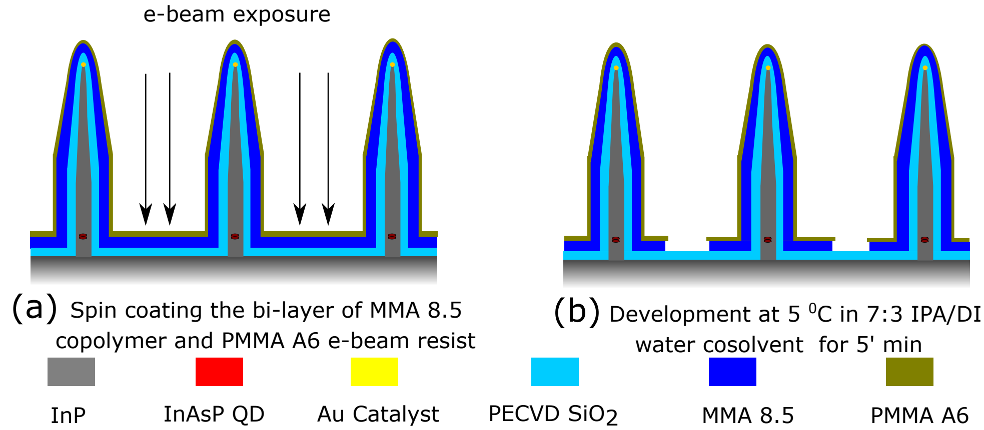

Figure 4.8: Defining gates by e-beam lithography: Schematic cross-sectional illustration of the mains steps for defining the gates by e-beam lithography. Processes are explained in the texts. Different colors in the figures are explained in the legends below.

(7:3 IPA/di-water) solution for 5' minutes (at 5 °C). We choose a bi-layer of MMA 8.5 and PMMA A6 positive e-beam photoresist. PMMA A6 is an e-beam sensitive resist while MMA 8.5 assist in the metal lift-off process due to its undercut profile after the development. The spin rate for each resist is carefully optimized to avoid the formation of side beads around the edge of the sample (1x1 cm). Subsequently, each layer is baked and its thickness is measured by Filmetric F-50 optical UV reflectometer set-up. To uniformly cover the nanowires and protect it during the metal lift-off step a minimum of 1500 nm of MMA 8.5 and 500 nm of PMMA A6 (1500 nm) e-beam thick resist is required. A cross-section illustration of the process is shown in figure 4.8 (a) and (b). Finally, a thin layer of a conductive polymer is spin-coated on the sample before exposing it to a e-beam pattern. This conductive polymer helps in grounding the sample surface and avoiding a charging at the time of e-beam exposure that could damage the nanowire quantum dot source. This polymer layer is removed after the exposure by dipping the sample in DI water for few minutes before development.

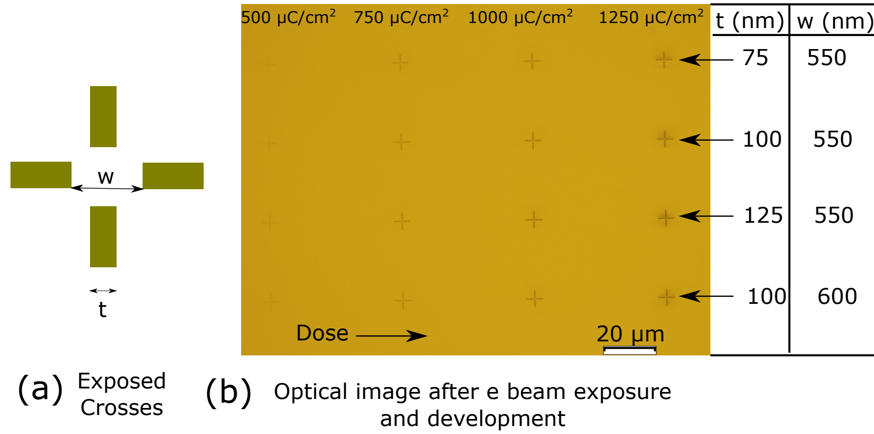

Figure 4.9: E-beam Dose Test: (a) Schematic of the exposed cross gates with a separation of (w) and the gate thickness (t). (b) An optical image after the e-beam exposure and development, doses are shown in the units of $\mu m/cm^2$ for each column of crosses. The table on the far right shows the thickness (t) and the separation (w) of the exposed crosses in each row.

The resolution of the features that we aim to expose is close to 100 nm (width of the gates), whereas the resist thickness is around $\approx 2\mu m$, due to this large aspect ratio between the exposed feature and resist thickness, the dose of an e-beam and the alignment of the gates with respect to the nanowires becomes very critical for our device. Both these steps are discussed in detail below.

Dose test

The e-beam dose test was performed by exposing the pattern of crosses as shown in Fig. 4.9 (a) into a series of columns with different doses expressed in the units of $\mu C/cm^2$, refer Fig. 4.9 (b). Each row of the exposed pattern has a different thickness (t) and separations (w) as shown in the table at the far right of Fig. 4.9. This step was followed by descum process to remove any residual resist followed by the Ti (15 nm)/Au (80 nm) deposition by

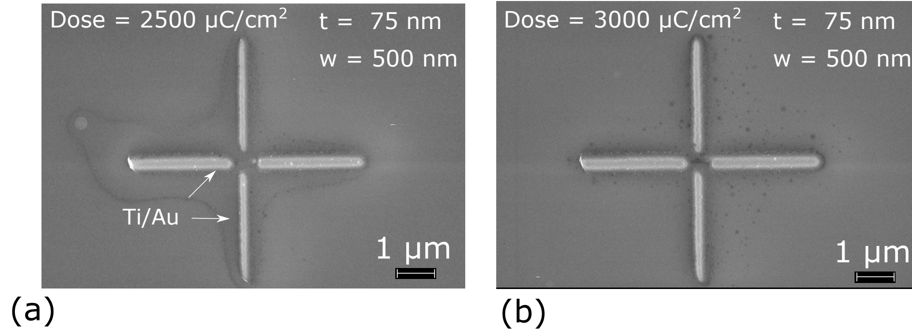

Figure 4.10: SEM image of metal cross: (a), (b) SEM image after metal deposition and lift-off, e-beam dose, gates dimensions (t), (w) for each image is in the text.

e-beam evaporation and lift-off process. We observed a substantial variation between the dimensions of the exposed features and the dimensions of the final metal gates after the lift-off process. Fig. 4.10 (a) and (b) shows the SEM image of the metal crosses after the lift-off.

The variations between the dimensions of the exposed features **t**, **w**, and the final dimensions of the metal gates **t'**, **w'** is summarised in the table 4.1. The figure above the table 4.1 shows the cross-sectional schematic view of the device-base after the metal deposition. It illustrates the spread of metal gates before it reaches the base of the InP wafer. This causes the actual dimension of the metal gates to differ from the exposed gates. Furthermore, we observe that the final gates are not symmetric. Top/Bottom gates have different dimensions than the Left/Right gates. We attribute this asymmetry in gates to the slight angle between the sample and metal source during the time of metal deposition. Hence, in the table 4.1 we have summarised both **t'** Top/Bottom and **t'** Left/ Right for an initially exposed pattern thickness (**t**) for a fixed dose of 2500 $\mu C/cm^2$. We didn't observe any substantial effect of an e-beam dose on these parameters. Below 2200 $\mu C/cm^2$ the features were underdeveloped and above that 3800 $\mu C/cm^2$ we saw an overexposure.

Dose = 2500 $\mu C/cm^2$

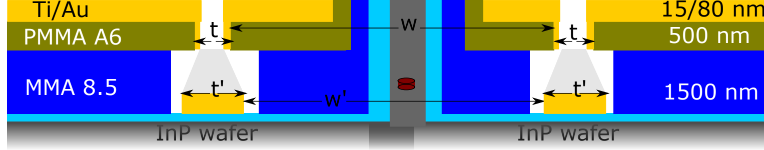

S.No	t (nm)	t' (nm) Top/Bottom	t' (nm) Left/Right	w (nm)	w' (nm)
1	100	455	544	600	350
2	125	448	567	500	290
3	100	449	535	500	231
4	75	346	481	550	368
5	50	261	465	550	375

Table 4.1: Dimensions of the metal gates from an e-beam dose test. A schematic cross sectional illustration of the base of InP nanowire pattern on the chip during the metal deposition step. Different parameters in the table (t,t',w,w') are shown schematically in the figure. Top/Bottom, Left/Right indicates the gates location when viewed from the top as shown in the SEM images of figure 4.10

Therefore, we choose 2500 $\mu C/cm^2$ as an e-beam dose for exposing the final pattern. At the time of metal deposition, we optimized the sample position to achieve a symmetric gate for t = 100 nm.

Alignment of the gates

An alignment of the gates to the single nanowires is important for our device design. For this purpose, we performed an alignment test by fabricating the test cross gates around the nanowires. In this test, we again repeated the procedure of spin coating, e-beam pattern exposure, development, metal deposition, and lift-off process as discussed in the previous

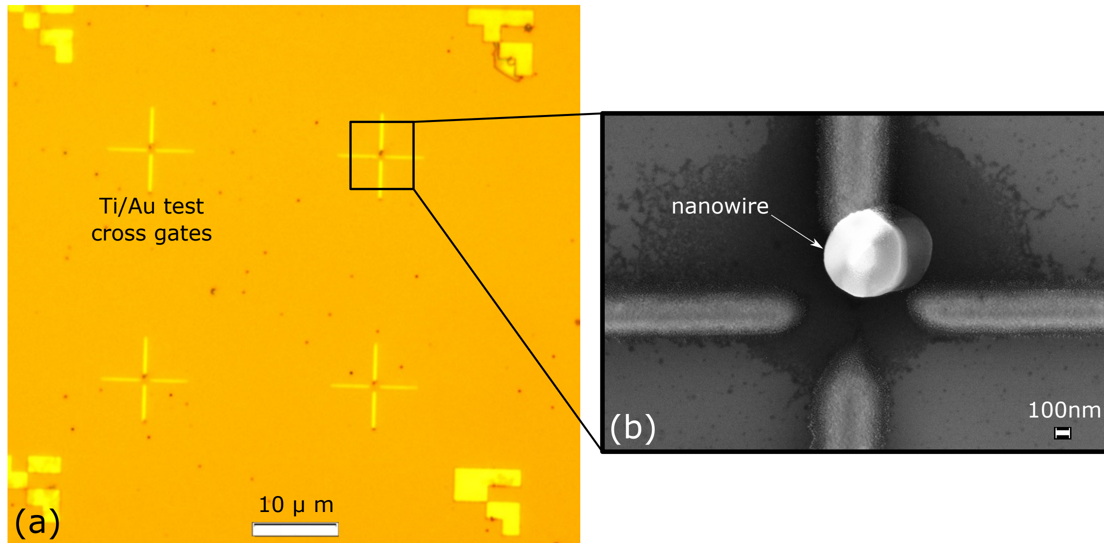

Figure 4.11: Image of the device during the alignment tests: (a) An optical image (top view) of the test metal gates fabricated around the nanowires. (b) SEM image (top view) of the single nanowire with test metal gates, corresponding to the nanowire shown by a small black box in the (a).

sections. However, this time we exposed the cross gates patterns (refer fig. 4.9 (a)) with different gates separation (**w**) around the nanowires at the fixed e-beam dose of 2500 $\mu C/cm^2$.

In Fig. 4.11 (a) we show an optical image (top view) of such large area on the sample with multiple metal gates fabricated around the nanowires. Fig. 4.11 (b) is the SEM image (top view) of one such single nanowire shown by the small black box on the Fig. 4.11 (a). A misalignment of the gates to the nanowires can be seen in Fig. 4.11 (b). The alignment markers on the sample were written by the different e-beam lithography system (50 kV JEOL), at the time of the nanowire growth. Therefore, any error in the coordinates of these alignment markers will cause the misalignment of our exposed features. We observed a constant offset error for all our test metal gates, hence, this misalignment could be corrected

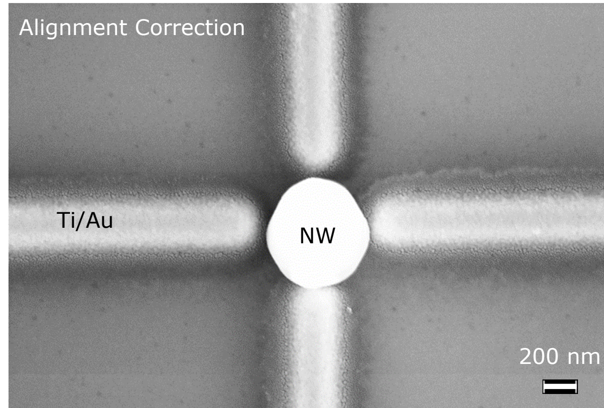

Figure 4.12: Gates alignment correction SEM image: SEM image (top view) of the device after alignment correction

by taking into account this global error. Before exposing the features of the final device we added this offset in our pattern. In Fig. 4.12 we show the SEM image of the final device (top view) after the alignment correction. Thus, we need to perform this alignment test for every chip before exposing the final gates.

4.3.3 Metal Deposition and lift-off

Although we have been depositing Ti/Au (15 nm/80 nm) during the dose and alignment test, the metal deposition step becomes critical in the final e-beam exposure and lift-off step. We observed that Ti was spreading between the regions of exposure and causing electrical leakage between the metal gates. This Ti migration is attributed to the kinetic phenomenon, in which the Ti molecules collide with each other at the time of the deposition under the MMA 8.5 resist layer. Therefore, we performed metal deposition under different deposition rates and vacuum pressures to observe if we could avoid this problem. For our features, we found out that at the slow deposition rate of 0.3 A/s and under UHV (10^{-7}

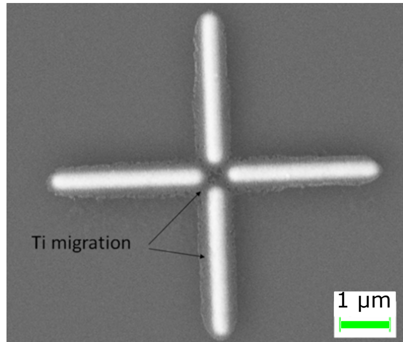

(a) SEM image (top View) Ti/Au at a dep rate: 1 A/s & pressure: 10^{-6} torr

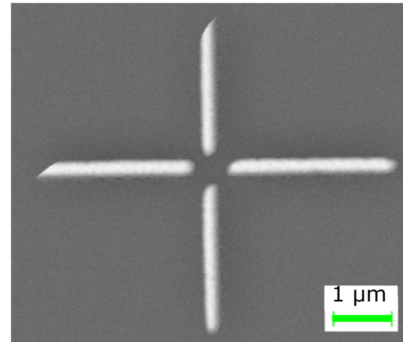

(b) SEM image (top View) Ti/Au at a dep rate: 0.3 A/s & pressure: 10^{-7} torr

Figure 4.13: SEM images metal deposition at UHV: SEM images at different deposition rate and vacuum, different parameters are given in text below the figures.

torr) of the deposition chamber, the Ti was not migrating between the exposed features. In Fig. 4.13 (a) and (b) we show the SEM image (top view) of the metal cross gates at two different deposition rates and vacuum. The metal deposition at UHV of 10^{-7} and slow deposition rates shows no Ti migration, refer Fig. 4.13 (b).

Therefore, we used these deposition conditions to fabricate the final device. In Fig. 4.14 (a) and (b) we show the schematic cross-sectional illustration for metal deposition and lift-off steps. In Fig. 4.14 (c) we show the SEM image at 45 ° of a single nanowire device after this step.

4.3.4 Selected area removal of dielectric

In this final step, we selectively remove the SiO_2 from the nanowires. The sample is again spin coated with the e-beam resist bi-layer, conductive polymer layer and exposed to the e-beam pattern to selectively remove the hard mask of resist from the nanowires by development in the chilled water co-solvent (7:3 IPA/di-water) solution (at 5 °C), these

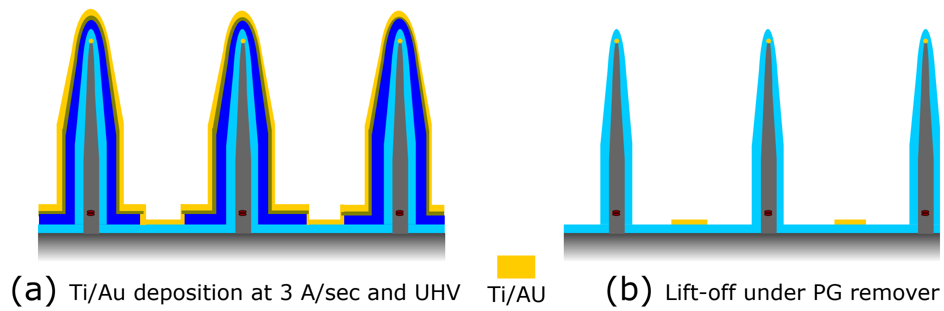

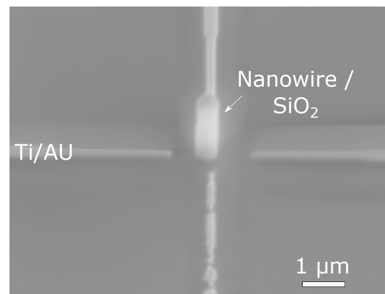

t!

(c) SEM image at 45 ^{0}

Figure 4.14: Metal deposition: Schematic cross sectional illustration of the metal deposition steps (a), (b). (c) SEM image at 45° of a single nanowire after the metal deposition. Processes from (a)-(b) are explained in the texts. Legends for different colors can be found in figure 4.8 with an additional legend for Ti/Au

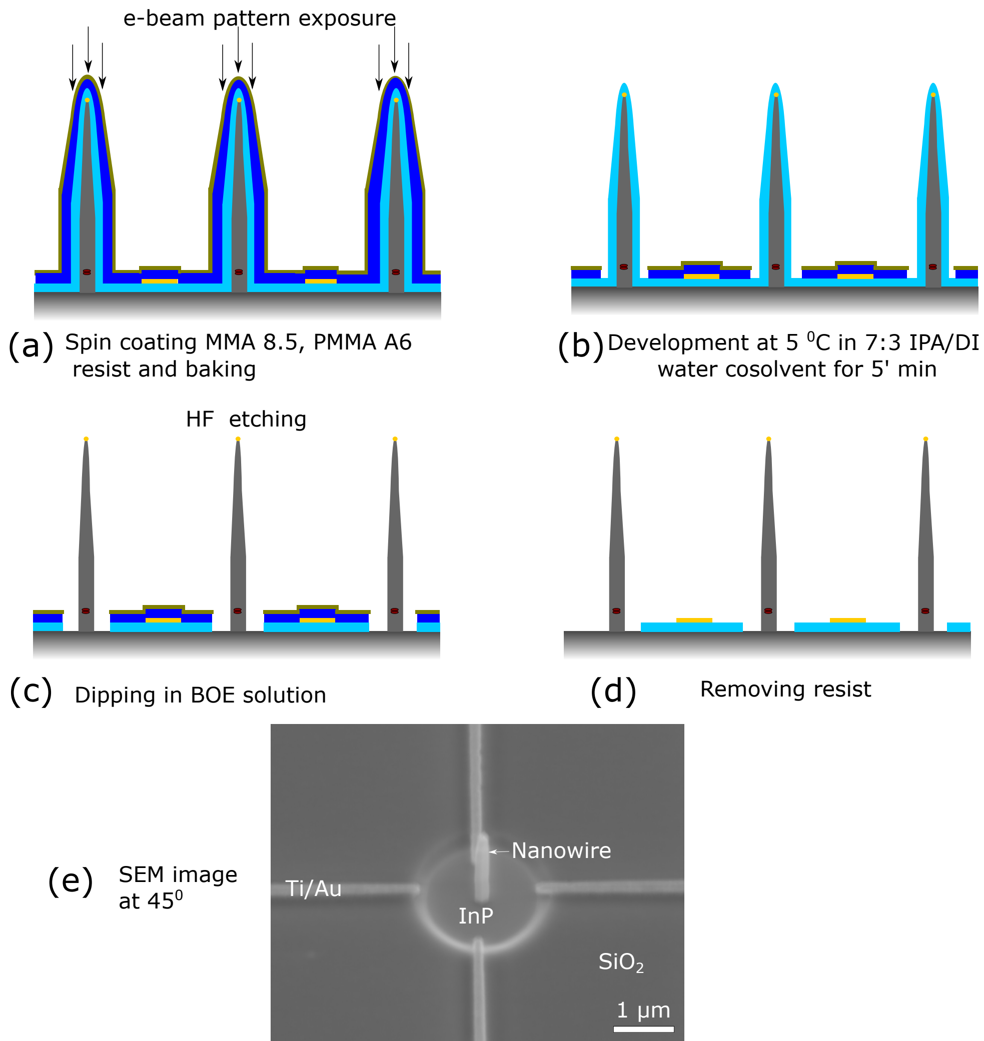

Figure 4.15: Steps for selectively removing the dielectric and the SEM image of the final device: Schematic cross sectional illustration of the mains steps for selectively removing the SiO_2, shown in the order (a)-(d). The different processes are explained in the texts. (e) SEM image at 45° of the final nanowire device. Legends for different colors can be found in figure 4.8 and 4.14

steps are shown in the cross sectional illustrations in Fig. 4.15 (a) and (b). Then the sample is dipped in a BOE solution to etch the SiO_2 from an unprotected area of nanowires, refer Fig. 4.15 (c). Finally the resist is removed by dipping the sample in the PG remover, refer Fig. 4.15 (d). The SEM image (at 45 $^{\circ}$) of a single nanowires gated device is shown the Fig. 4.15 (e). We fabricate eight such single nanowire devices on one chip. These nano-metal contacts are extended to a micron-sized metal bond pads, likes the ones that are shown in Fig. 4.7 (a), they are used for wire bonding.

Chapter 5

Characterization and Measurements

In this chapter, we will report the characterization and measurements of the gated nanowire devices that we have fabricated. The first generation of devices were fabricated by UV lithography and the second generation by an e-beam lithography (refer chapter 4). Therefore for classification, we will label them as UV and e-beam gates device respectively. In the first section, we will present an experimental set-up designed by us for performing a polarization-dependent micro-PL measurement, this set-up is used to characterize the optical emission from a single nanowire device and measure its FSS. In the next sections, we will present these measurements performed on our fabricated devices. Finally, we present the FSS measurement on our device as the function of an applied quadrupole and lateral electric field.

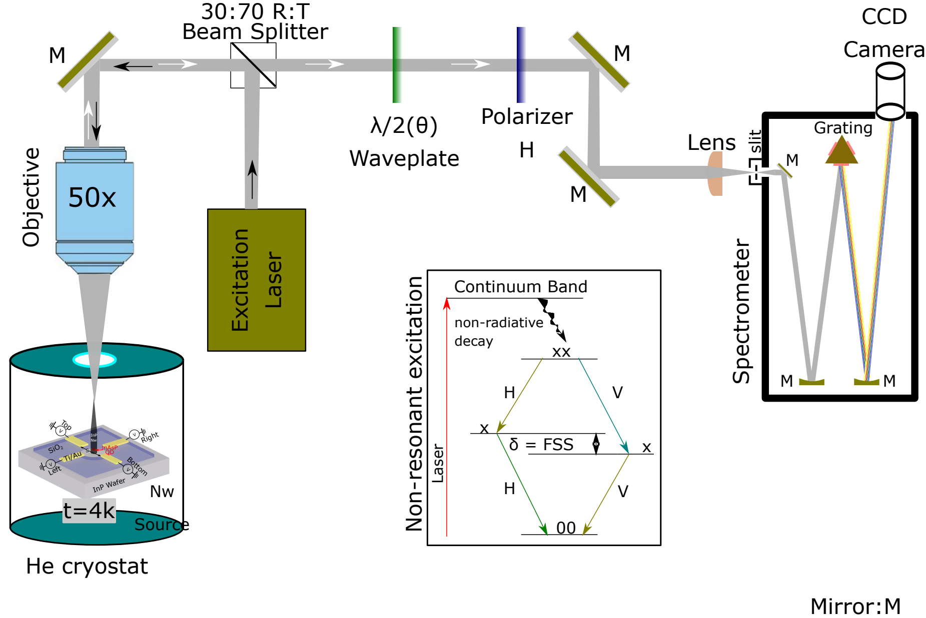

Figure 5.1: Schematic illustration of the experimental set-up for the polarization dependent micro-PL: Inset: Non resonant excitation scheme where the sample is excited with the continuous HeNe laser above the InP band gap.

5.1 Micro-PL experimental set-up

A micro-PL measurement is performed by exciting the nanowire source non-resonantly above the InP band gap by a continuous HeNe laser at 632 nm (refer Fig. 5.1 inset box) and collecting the emission by the same 50x infinity-corrected objective of a NA of 0.85 and a spot size of 2 μm. The fabricated device is mounted on a piezo stage that can move the sample on the three (x,y,z) axis inside the closed cycle Helium (He) cryostat and all the measurements are then performed at 4.5 K. The metal gates on the device are wire bonded to the connection lines inside the cryostat that share the same ground. Therefore, we can apply an independent potential on all the four gates of the device. In figure 5.1 we sketch the experimental set-up for the optical measurements. The emission is sent to

a spectrometer where the emission is filtered by the 1200 lines/mm grating, to suppress the laser and InP nanowire fluorescence, while resolving the InAsP quantum dot s-shell emission lines. The polarization-dependent PL measurement is performed by inserting the half-waveplate ($\lambda/2$) on a high precision motorized control mounts and a linear polarizer in between the optical path of the collected beam. The optical axis of the linear polarizer is kept fixed and aligned with the horizontal axis of the optical table. FSS causes the eigenstates of the QD to change from circular basis to the rectilinear basis, refer equation 2.20, 2.21. Hence, by rotating the half-wave-plates (degrees) we can select one of the two orthogonal linear polarization to pass through the linear polarizer. Therefore, we can experimentally measure the FSS of the QD by recording the shift in the peaks of exciton and biexciton peaks as a function of linear orthogonal polarization's. However, to increase the accuracy of FSS measurement we plot the relative difference between the exciton(E_X) and biexciton (E_{XX}) peaks: $(E_X - E_{XX}) - \overline{(E_X - E_{XX})}$, the FSS is then estimated by the amplitude of the fitted cosine function.

5.2 Effect of SiO_2 shell on the QD emission

A thin film of SiO_2 is required for the electrical isolation of metal gates in our device design. However, this post-growth PECVD SiO_2 deposition has a significant impact on the optical properties of the quantum dot. To study this impact we deposited 300 nm of SiO_2 on a separate QD sample and took the spectra from a single nanowire before and after the dielectric deposition. We observe a redshift and the broadening in the emission of the QD s-shell emission after the SiO_2 deposition. This is shown in Fig. 5.2. After the deposition of SiO_2 the emission of an as-grown QD (1.41 eV) redshifts to 1.38 eV. This shift in the QD emission (30 meV) is significant in comparison to the neutral exciton line-width of

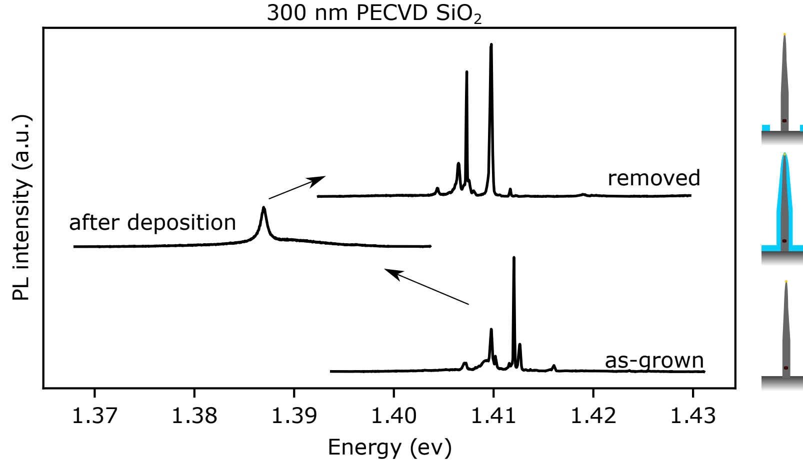

Figure 5.2: Effect of SiO_2 deposition on the QD emission: A PL spectrum from an as-grown quantum dot, same dot with 300 nm of PECVD SiO_2 deposited, spectrum after the oxide is removed. Spectrum are shifted vertically for comparisons and intensities are in arbitrary units. Schematic illustration of a nanowires after each step, legends for different colors can be found in Fig. 4.2

about 0.15 meV. When we selectively remove the dielectric from the top of the nanowire (refer section 4.2.2) the shape and energies of the QD shifts back to its original value. A slight shift in the energies (1.409 eV) from the original value is attributed to some residual dielectric left on the nanowire.

The QD energy shift and its restoration after the removal of SiO_2 indicates that this is due to the straining of the QD by the dielectric layer. A thin oxide film deposited by PECVD is known for inducing the strain on the underlying semiconductor material [78]. An applied tensile strain on the semiconductor would increase its lattice parameter and reduce its band-gap energy [79]. Therefore, selectively removing the SiO_2 from the top of the nanowire is a necessary step in our device design. It restores the QD brightness and its

emission properties.

5.3 UV Lithography device

5.3.1 Photoluminescence and power dependent measurement

The micro-PL measurements were performed on the chips to find and map the coordinates of the nanowires with a bright QD emissions. Hence, we fabricated the gated device on eight such nanowires by the methods discussed in section 4.2. However, only one nanowire device survived our fabrication steps, the rest of the nanowires were found out to be broken by the end of all the fabrication steps. The reason and strategy to overcome this problem have been discussed in section 4.3. The chip with a fabricated device is then mounted inside the closed cycle Helium (He) cryostat and all the measurements are then performed at 4.5 K. In Fig. 5.3 (a) we plot the broadband PL spectrum of our nanowire device. The peak at 830 nm corresponds to the wurtzite InP nanowire bandgap transition [29] and the QD s-shell transitions are indicated by the arrow. The exciton and biexciton peaks are then characterized by the power-dependent PL measurements. In Fig. 5.3 (b) we plot the higher resolution PL spectra of the QD s-shell transitions for different excitation powers. The integrated counts/sec for exciton and biexciton has a linear and quadratic dependence on the excitation power this could be seen in Fig. 5.3 (c), where we plot them on the log-log scale. The blue (linear) and red (quadratic) line fits the two emission lines confirms that these transitions are exciton and biexciton.

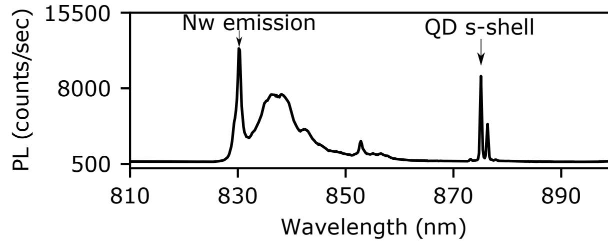

(a) Broadband emission spectrum of the nanowire source excited at 632 nm

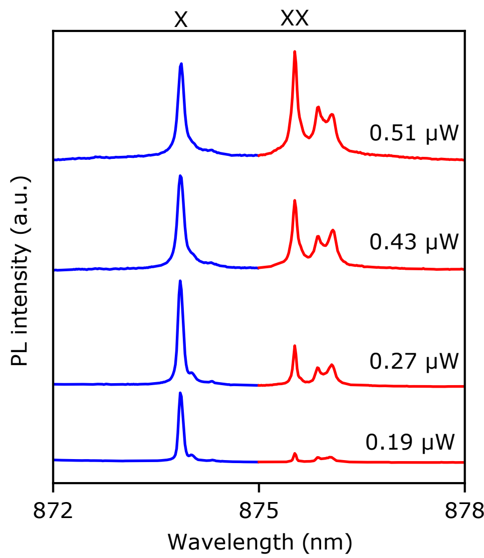

(b) Power dependent PL

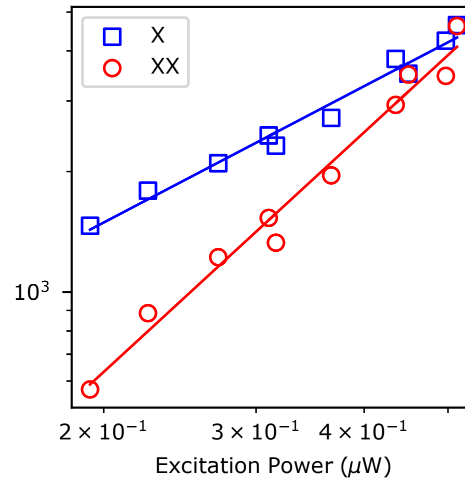

(c) Linear and quadratic fit to the integrates peaks of X and XX

Figure 5.3: Emission spectrum and power-dependent measurements: (a) Broadband nanowire emission spectra. Nanowire and QD s-shell emission is indicated by the text (b) Higher resolution power-dependent PL spectrum of the QD s-shell emissions for different excitation powers indicated by the texts and are shifted vertically for comparison, PL intensities are in arbitrary units. (c) Integrated peaks intensities for exciton and biexciton peaks. Square (X) and circles (XX) are the data points and blue and red lines are the linear and quadratic fits in the log-log scale to the excitation power.

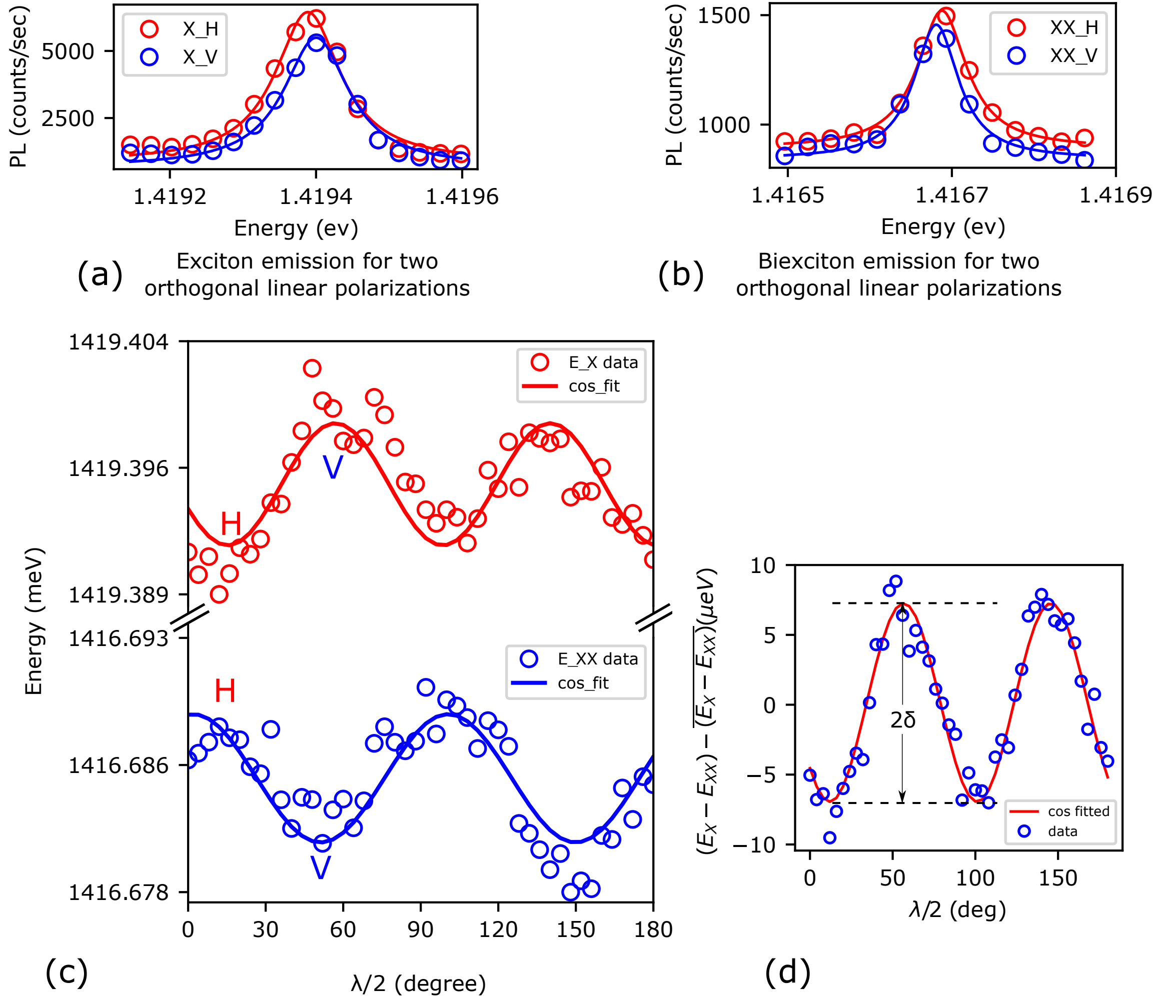

Figure 5.4: Polarization dependent measurements: Polarization dependent spectrum of exciton and biexciton emissions for the two orthogonal linear polarization H and V (a) and (b). (c) Plots of Exciton (red circles) and biexciton (blue circles) emission peaks as function of $\lambda/2$ wave-plate angle in degrees, fitted with cosine function. Orthogonal linear polarization H and V are indicated on the figures. (d) Plot for $(E_X - E_{XX}) - \overline{(E_X - E_{XX})}$ (blue circles) as a function of $\lambda/2$ wave-plate angle in degrees, fitted with a cosine function (red curve)

5.3.2 Polarization dependent PL: FSS measurements

The polarization dependent PL measurements were performed on the gated device by rotating the $\lambda/2$ wave-plate (degrees) and recording the QD spectrum after passing it through a linear polarizer with its optical axis aligned with the horizontal (H) axis of the optical table (refer Fig. 5.3).

In Fig. 5.4 (a) and (b) we plot the high-resolution exciton (X) and biexciton (XX) emission peaks for the two orthogonal linear polarization's, horizontal (H, red circles) and vertical (V, blue circles), and they are fitted with Lorentzian function to extract its peak wavelength. The exciton (red circles) and biexciton (blue circles) Lorentzian fitted peaks oscillate between the two orthogonal linear polarization's (H, V) as we rotate the $\lambda/2$ wave-plate (degrees) and it can be seen the Fig. 5.4 (c) where we plot them as a function of the $\lambda/2$ wave-plate angles (degree) and there oscillations are fitted with the cosine functions. The FSS can be estimated by the amplitude (A_{cos}) of the fitted cosine functions of these plots ($\delta = 2A_{cos}$). To increase the accuracy of FSS measurement we plot the relative difference between the exciton(E_X) and biexciton (E_{XX}) peaks: $(E_X - E_{XX}) - \overline{(E_X - E_{XX})}$ (blue circles) in Fig. 5.4 (d). FSS is then estimated by the amplitude of the fitted cosine function to this curve. For our device when all the gates are grounded (V=0) the intrinsic value of the QD FSS is found out to be $7.103 \pm 0.289\ \mu eV$

5.3.3 FSS vs Electric field

In the final step, we applied an external DC electric field on the metal gates and measured the FSS of our device. To perform this measurement, we wire-bonded the micro-contact pads of the device to d-sub connectors inside the cryostat cold-head. These d-sub electrical lines are connected to an external BNC female ports. We then connect

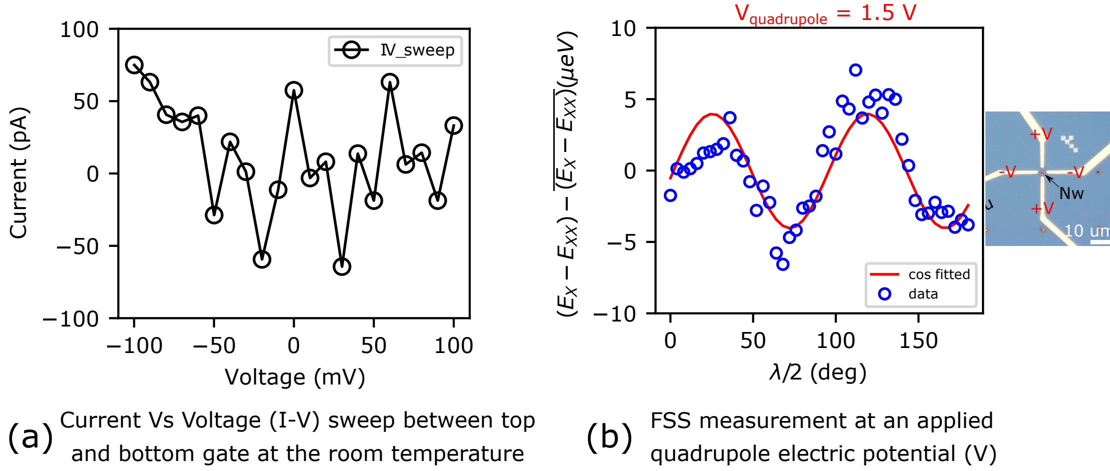

Figure 5.5: Current vs Voltage sweep: (a) Volatge vs Current plot between top and bottom gates. (b) (b) At V$_{quadrupole}$ = 1.5 V, relative difference between exciton (E_X) and biexciton (E_{XX}) is plotted and the FSS is estimated from the amplitude of fitted cosine function. On the far right an optical image of the device (top-view) with the text on each gates specifying the applied voltage on each gate i.e. top/bottom gates = +1.5 V and left/right gates = -1.5 V,

external DC power supplies (SIM900) to these BNC ports. The DC power supplies and the cold-head inside the cryostat share the same grounds. Therefore, we can apply independent electric potential on each gate of the device.

Before starting the FSS measurements we perform a current-voltage (I-V) sweep across the gates to test their electrical isolation. We swept 100 mV of voltages between the two gates at the room temperature and measured the current between them. In Fig. 5.5 (a) we plot voltage vs current between the top and bottom gates of the device, we detected the fluctuating current in tens of picoamp around the standard noise level of our measurement set-up. These tests were performed between all the gates to confirm they all were electrically isolated. Finally, to test our quadrupole theory we applied the quadrupole potential on

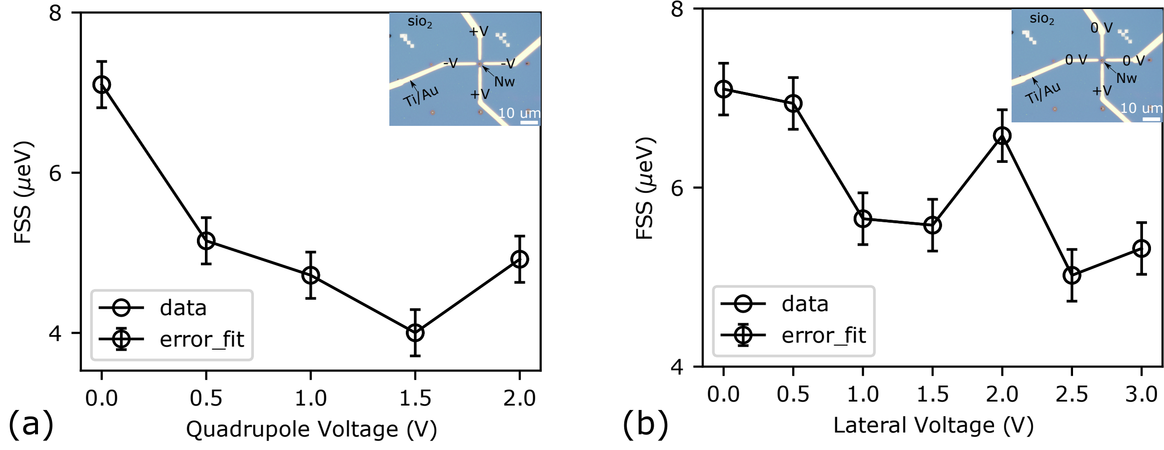

Figure 5.6: FSS as a function of applied quadrupole and lateral electric field: (a) Measured FSS as the function of quadrupole voltage (V). (b) Measured FSS as the function of lateral voltage (V). Insets: an optical image of the device (top-view) with the text on each gates specifying the applied voltage on each gate. Circles: data points. A straight line joining the circles are for visual aid.

our device by applying a positive potential (+V) on top and bottom gates and an equal negative potential (-V) on the left and right gate. We observed a decrease in the FSS of our device when we applied a quadrupole potential in a step of 0.5 V. In Fig. 5.5 (b) we plot the oscillation for the relative $((E_X - E_{XX}) - \overline{(E_X - E_{XX})})$ peak for $V_{quadrupole} = 1.5$ V.

In Fig. 5.6 (a) we plot the measured FSS of our device as a function of an applied quadrupole potential. The trend suggests we can reduce the FSS of our device. However, we observe the lower bound to the FSS of 4.0 μev, this lower bound for FSS is expected when the dipole orientation of the quantum dot is not aligned to the axis of metal gates [30]. The FSS tuning with quadrupole potential can be further explored according to our theoretical proposal [30], by reducing the step size of potentials as well as changing the individual potential of each gate to further reduce the FSS below this lower bound.

However, our metal gates started leaking current at an applied quadrupole voltage of 2 V during the potential sweep. This leakage was fixed by warming up our sample to the room temperature and again cooling it down to 4.5 K. This thermal cycle assist in healing the insulating SiO_2 layer below the metal gates. Consecutively, we applied a lateral electric field (V) on our device by keeping all the metal gates grounded (0 V) while sweeping the potential on the bottom gates. In Fig. 5.6 (b) we plot the FSS as a function of an applied lateral field (V), the trend suggests we can tune the FSS and decrease it to 5.02 μeV. In principle, by applying an additional lateral electric potential between the left and right gate we should be able to completely erase the FSS. However, we again encountered the electrical leakage at an applied lateral potential of 3 V. The device could not be healed by thermal cycling after these measurements.

The FSS tuning of our device shows the proof of principle. However, these devices are far from an optimum design proposed in chapter 3. The perfect device will have metal gates very close to the sidewalls (100's nm) of the nanowire source so that we can effectively apply the electric field in the plane of the QD. In the case of the UV device, the metal gates are relatively far (1-2 μm) from the nanowire source, therefore a higher voltage is required between the gates to tune the FSS of the InAsP QD. This higher voltage also causes the breakdown of the underlying SiO_2 dielectric thin film in our device. Therefore, for the next generation of gated devices, we switched to an e-beam lithography to bring the metal gates much closer to the nanowire source and achieve a FSS tuning at much lower external voltages.

5.4 Ebeam lithography device

5.4.1 Photoluminescence measurement

We performed a micro-PL measurements on the chip with InAsP/InP QD nanowires to find and map the nanowires with bright QD emission. On the sample chip with a dimension of 10 x 10 mm, we fabricated gates around eight such nanowires (refer section. 4.3). For this device, we kept the deposited dielectric (SiO_2) film until the last step of the fabrication, and then selectively removed it from an area lithographically defined around the nanowire. This way we protected the nanowires throughout the fabrication procedure and were able to successfully fabricate six nanowire devices.

However, we observed that a 100 kV e-beam deteriorates the QD emission. In Fig. 5.7, we show the PL spectrums of the nanowire quantum dot sources before (left figure) and after (right figure) the device fabrication. In Fig. 5.7 (a) we show broadband spectrum of a nanowire device (labeled device-1), the nanowire (Nw) emission at 830 nm [29] remains unaffected, while the QD s-shell emission is lost after the e-beam exposure. In Fig. 5.7 (b) and (c) we plot the high-resolution PL spectrum of the two other nanowire quantum dot sources, labeled as device-2 and the device-3. In these figures, we could see the deterioration of the QD s-shell emission, the multiple emission lines (as-grown, left figure) are broadened and are shifted in energies (after e-beam, right figure). Therefore, we could not perform any FSS measurement on this device.

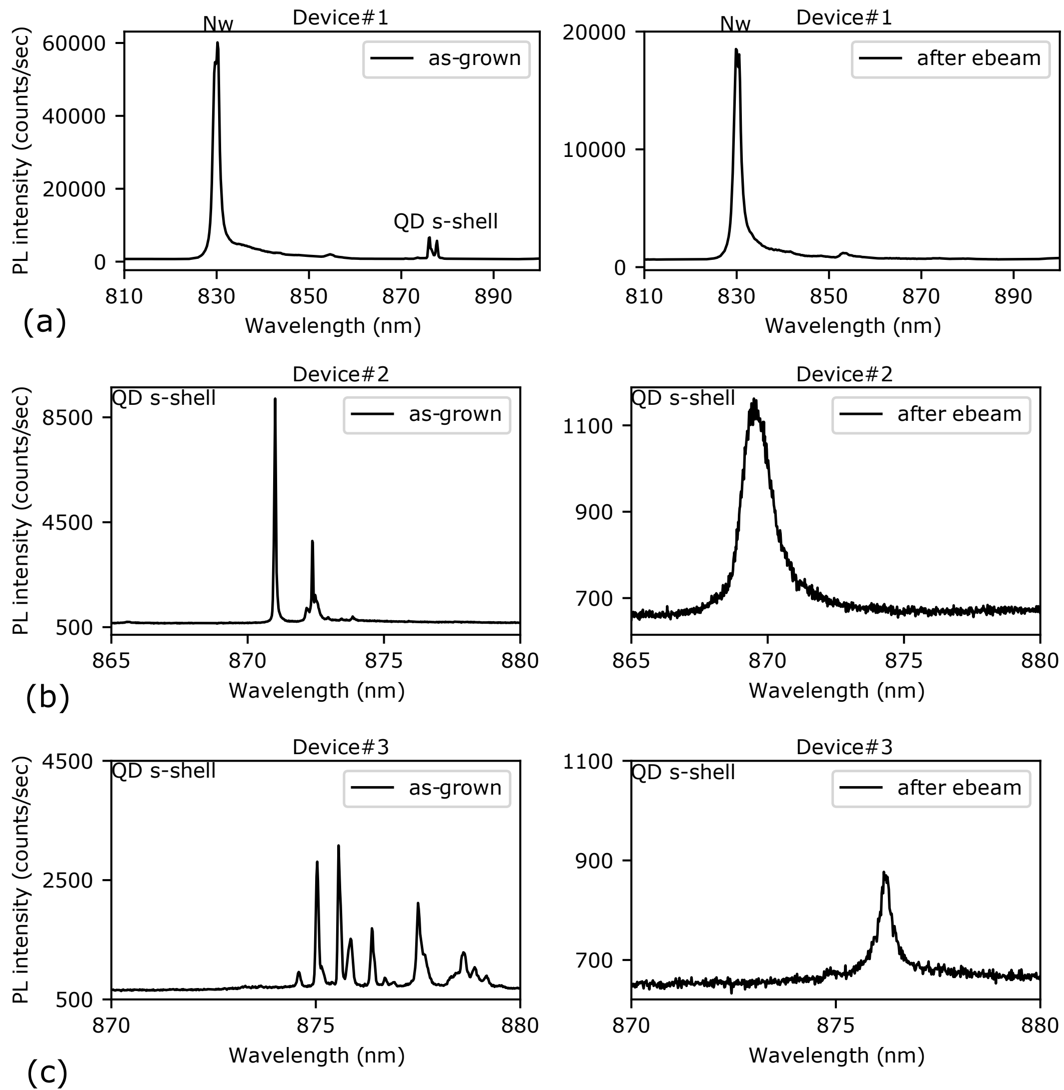

Figure 5.7: PL spectrum before and after e-beam exposure: (a) A broadband PL spectrum of the nanowire device-1 before (left figure) and after (right figure) the 100 kV e-beam exposure, during the fabrication of the metal gates. The quantum dot (QD) s-shell emission is lost after the e-beam exposure for this device. (b) and (c) are the high-resolution PL spectrum plots for device-2 and device-3. In these figures, we can see the deterioration and broadening of the QD s-shell emission lines after the e-beam exposure.

5.5 Conclusions

In summary, we have characterized the optical properties of the vertical InP/InAsP nanowire quantum dot source after fabricating metal gates around them by UV and e-beam lithography. The post-growth PECVD SiO_2 dielectric layer degrades the QD emission by straining (tensile) the nanowire, but this effect is reversible, and the QD emission can be restored by removing the SiO_2 from the nanowire. The FSS of the UV devices can be tuned by applying a quadrupole as well as a lateral electric field across its four gates. However, due to the electrical leakage in the device, we were only able to achieve the lower bound of 4 μeV and 5.02 μeV respectively. Although we were able to fabricate an optimum device by an e-beam lithography we observed that 100 kV e-beam permanently deteriorates the InAsP QD during the fabrication of the device.

Chapter 6

Conclusion and future outlook

6.1 Summary

In summary, we have proposed an approach to erase the FSS of a nanowire QD entangled photon source by applying a quadrupole electric field. We have performed numerical simulations for calculating the single-particle wave-functions of the QD as a function of an applied external quadrupole field. The novelty of our proposal lies in the demonstration that we can erase the FSS of the QD for any dipole orientation (QD elongation axis), without compromising its brightness (e-h overlap). This opens up an opportunity to design an electrically gated nanowire /QD as a bright source of entangled photons generated on-demand.

To test our theory, we have fabricated and tested vertically gated InAsP/InP nanowire quantum dot devices. In the first generation of devices (UV devices), we demonstrated the tuning of the FSS by applying an external quadrupole and lateral electric field and we could reduce the FSS of the InAsP QD from 7 μeV to 4 μeV and 5.02 μeV, respectively, before our

device starts leaking electrical current between the gates. Next, we developed a fabrication recipe for the second generation of the device by patterning the metal gates by e-beam lithography. Although we were able to fabricate a near-optimum device, unfortunately, we were unable to demonstrate its FSS tuning since we found out that a 100 kV e-beam deteriorates the QD emission. In principle, we could switch to lower e-beam energies (50 kV, 20 kV) to protect the QD emission, however, it would be difficult to achieve such resolutions (100 nm width) while patterning a thick resist (2 μm) that is required to protect the vertical nanowires. Therefore, we are currently limited with fabrication technological challenges where we can't pattern current features with an e-beam of lower energies.

6.2 Future Outlook

The research work in this thesis lays the groundwork for envisioning an electrically gated source of bright entangled photon pairs based on photonic nanowires. Erasing the FSS of a nanowire quantum dot source without compromising its high brightness will bring them to the forefront of entangled photon research and applications. Building on our fabrication knowledge, an alternate recipe could be developed with a lower energy e-beam. However, the biggest challenge while fabricating a vertical nanowire quantum dot source is the protection and preservation of the QD emission while the sample goes through various fabrication steps. This has limited us with our choices of resist, spin coating recipes, and the energies of the e-beam. Therefore, we envision a possible bottom-up approach for fabricating such devices, where the metal gates are fabricated first and the nanowire quantum dot sources are then grown selectively at the desired location. In Fig. 6.1 (a-f) we illustrate the proposed fabrication steps for fabricating a metal gate by conventional e-beam lithography and then integrating the selective VLS nanowire growth method [29] to grow

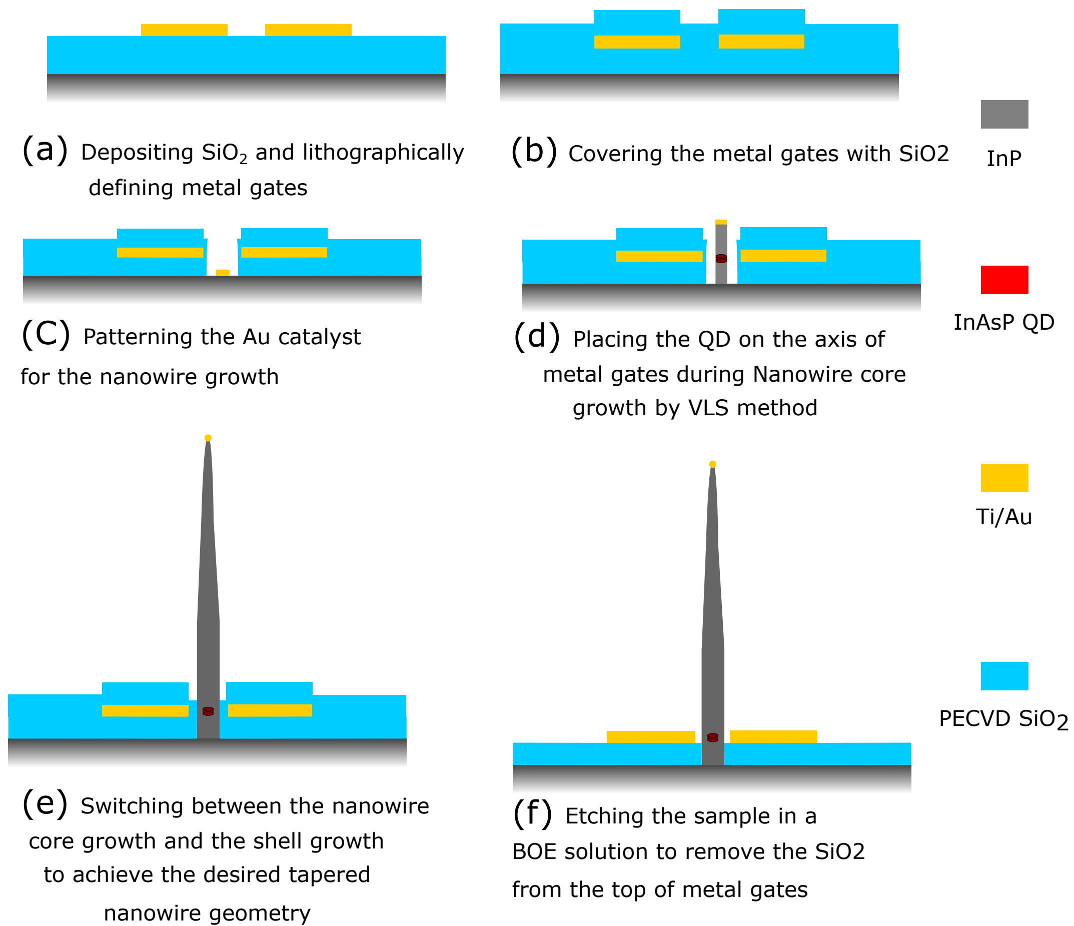

Figure 6.1: Schematic of the proposed bottom-up fabrication steps: Schematic cross-sectional illustration of the mains steps for fabricating a vertical nanowire device by a bottom-up approach, shown in the order (a)-(b). The different processes are explained in the texts. Legends for different color can be found in figure

the nanowire at the desired location between the fabricated gates. This approach has a significant advantage over the top-down fabrication approach as the nanowire quantum dot source will avoid all of the physically demanding fabrication steps, as well as any e-beam exposure that can degrade its optical properties.

The next step should be to perform quantum state tomography measurements to study the effect of an applied quadrupole electric field on the entanglement fidelity of the emitted biexciton-exciton photon pairs. We have built an experimental set-up to perform these measurements by exciting the nanowire quantum dot source at a quasi-resonant frequency [60], but the next step should be to perform these measurements by resonant (TPE) excitation. Our approach to erase the FSS with a quadrupole field is also promising for building a quantum repeater [80]. The key ingredients for building a quantum repeater is a tunable source of entangled photons with near-unity efficiency, fidelity, and indistinguishability. We envision that the quantum dot emission wavelength can be tuned for entanglement swapping by adding an additional back-gate. This same back gate can also be used to control the electrostatic environment of the quantum dot for achieving near-unity indistinguishability [?]. Finally, electric-field based devices have a potential advantage over strain-based devices as only a few volts are needed to remove the FSS. In contrast, for a typical strain-based device an external power source of a few kV is required [52].

References

[1] J. W. Pan, Z. B. Chen, C. Y. Lu, H. Weinfurter, A. Zeilinger, and M. Zukowski, ''Multiphoton entanglement and interferometry,'' *Reviews of Modern Physics*, vol. 84, no. 2, 2012.

[2] L. K. Shalm, E. Meyer-Scott, B. G. Christensen, P. Bierhorst, M. A. Wayne, M. J. Stevens, T. Gerrits, S. Glancy, D. R. Hamel, M. S. Allman, *et al.*, ''Strong loophole-free test of local realism,'' *Physical review letters*, vol. 115, no. 25, p. 250402, 2015.

[3] J.-W. Pan, D. Bouwmeester, M. Daniell, H. Weinfurter, and A. Zeilinger, ''Experimental test of quantum nonlocality in three-photon Greenberger–Horne–Zeilinger entanglement,'' *Nature*, vol. 403, no. 6769, pp. 515--519, 2000.

[4] M. Giustina, A. Mech, S. Ramelow, B. Wittmann, J. Kofler, J. Beyer, A. E. Lita, B. Calkins, T. Gerrits, S. W. Nam, R. Ursin, and A. Zeilinger, ''Bell violation using entangled photons without the fair-sampling assumption,'' *Nature*, vol. 497, no. 7448, pp. 227--230, 2013.

[5] C. Erven, E. Meyer-Scott, K. Fisher, J. Lavoie, B. L. Higgins, Z. Yan, C. J. Pugh, J. P. Bourgoin, R. Prevedel, L. K. Shalm, L. Richards, N. Gigov, R. Laflamme, G. Weihs,

T. Jennewein, and K. J. Resch, ‘‘Experimental three-photon quantum nonlocality under strict locality conditions,’’ *Nature Photonics*, vol. 8, no. 4, pp. 292--296, 2014.

[6] M. Müller, S. Bounouar, K. D. Jöns, M. Glässl, and P. Michler, ‘‘On-demand generation of indistinguishable polarization-entangled photon pairs,’’ *Nature Photonics*, vol. 8, no. 3, pp. 224--228, 2014.

[7] A. Fognini, A. Ahmadi, M. Zeeshan, J. T. Fokkens, S. J. Gibson, N. Sherlekar, S. J. Daley, D. Dalacu, P. J. Poole, K. D. Jöns, V. Zwiller, and M. E. Reimer, ‘‘Path to perfect photon entanglement with a quantum dot,’’ *arXiv:1710.10815 [quant-ph]*, pp. 1--8, 2017.

[8] M. E. Reimer, D. Dalacu, J. Lapointe, P. J. Poole, D. Kim, G. C. Aers, W. R. McKinnon, and R. L. Williams, ‘‘Single electron charging in deterministically positioned InAs/InP quantum dots,’’ *Applied Physics Letters*, vol. 94, no. 1, 2009.

[9] M. E. Reimer, G. Bulgarini, N. Akopian, M. Hocevar, M. B. Bavinck, M. A. Verheijen, E. P. A. M. Bakkers, L. P. Kouwenhoven, and V. Zwiller, ‘‘Bright single-photon sources in bottom-up tailored nanowires.,’’ *Nature Communications*, vol. 3, p. 737, 2012.

[10] C. L. Salter, R. M. Stevenson, I. Farrer, C. A. Nicoll, D. A. Ritchie, and A. J. Shields, ‘‘An entangled-light-emitting diode,’’ *Nature*, vol. 465, no. 7298, pp. 594--597, 2010.

[11] A. Dousse, J. Suffczyński, A. Beveratos, O. Krebs, A. Lemaître, I. Sagnes, J. Bloch, P. Voisin, and P. Senellart, ‘‘Ultrabright source of entangled photon pairs,’’ *Nature*, vol. 466, no. 7303, pp. 217--220, 2010.

[12] W. M. Witzel, M. S. Carroll, A. Morello, Ł. Cywiński, and S. Das Sarma, "Electron spin decoherence in isotope-enriched silicon," *Physical Review Letters*, vol. 105, no. 18, 2010.

[13] M. Bayer, G. Ortner, O. Stern, A. Kuther, A. A. Gorbunov, A. Forchel, P. Hawrylak, S. Fafard, K. Hinzer, T. L. Reinecke, S. N. Walck, J. P. Reithmaier, F. Klopf, and F. Schäfer, "Fine structure of neutral and charged excitons in self-assembled in(ga)as/(al)gaas quantum dots," *Phys. Rev. B*, vol. 65, p. 195315, May 2002.

[14] O. Benson, C. Santori, M. Pelton, and Y. Yamamoto, "Regulated and entangled photons from a single quantum dot," *Physical review letters*, vol. 84, no. 11, p. 2513, 2000.

[15] T. Kuroda, T. Mano, N. Ha, H. Nakajima, H. Kumano, B. Urbaszek, M. Jo, M. Abbarchi, Y. Sakuma, K. Sakoda, I. Suemune, X. Marie, and T. Amand, "Symmetric quantum dots as efficient sources of highly entangled photons: Violation of bell's inequality without spectral and temporal filtering," *Phys. Rev. B*, vol. 88, p. 041306, Jul 2013.

[16] Y. H. Huo, A. Rastelli, and O. G. Schmidt, "Ultra-small excitonic fine structure splitting in highly symmetric quantum dots on GaAs (001) substrate," *Applied Physics Letters*, vol. 102, no. 15, p. 152105, 2013.

[17] J. Skiba-Szymanska, R. M. Stevenson, C. Varnava, M. Felle, J. Huwer, T. Müller, A. J. Bennett, J. P. Lee, I. Farrer, A. B. Krysa, P. Spencer, L. E. Goff, D. A. Ritchie, J. Heffernan, and A. J. Shields, "Universal growth scheme for quantum dots with low fine-structure splitting at various emission wavelengths," *Phys. Rev. Applied*, vol. 8, p. 014013, Jul 2017.

[18] R. Keil, M. Zopf, Y. Chen, B. Höfer, J. Zhang, F. Ding, and O. G. Schmidt, ‘‘Solid-state ensemble of highly entangled photon sources at rubidium atomic transitions,’’ *Nature Communications*, vol. 8, no. May, p. 15501, 2017.

[19] K. Kowalik, O. Krebs, A. Lemaître, S. Laurent, P. Senellart, P. Voisin, and J. A. Gaj, ‘‘Influence of an in-plane electric field on exciton fine structure in InAs-GaAs self-assembled quantum dots,’’ *Applied Physics Letters*, vol. 86, no. 4, 2005.

[20] A. J. Bennett, M. A. Pooley, R. M. Stevenson, M. B. Ward, R. B. Patel, A. B. de la Giroday, N. Sköld, I. Farrer, C. A. Nicoll, D. A. Ritchie, and A. J. Shields, ‘‘Electric-field-induced coherent coupling of the exciton states in a single quantum dot,’’ *Nature Physics*, vol. 6, pp. 947--950, Dec. 2010.

[21] J. Wang, M. Gong, G. C. Guo, and L. He, ‘‘Eliminating the fine structure splitting of excitons in self-assembled InAs/GaAs quantum dots via combined stresses,’’ *Applied Physics Letters*, vol. 101, no. 6, p. 063114, 2012.

[22] R. M. Stevenson, R. J. Young, P. Atkinson, K. Cooper, D. A. Ritchie, and A. J. Shields, ‘‘A semiconductor source of triggered entangled photon pairs.,’’ *Nature*, vol. 439, no. 7073, pp. 179--182, 2006.

[23] R. M. Stevenson, R. J. Young, P. See, D. G. Gevaux, K. Cooper, P. Atkinson, I. Farrer, D. A. Ritchie, and A. J. Shields, ‘‘Magnetic-field-induced reduction of the exciton polarization splitting in inas quantum dots,’’ *Phys. Rev. B*, vol. 73, p. 033306, Jan 2006.

[24] R. Trotta, E. Zallo, C. Ortix, P. Atkinson, J. D. Plumhof, J. van den Brink, A. Rastelli, and O. G. Schmidt, ‘‘Universal recovery of the energy-level degeneracy of bright

excitons in ingaas quantum dots without a structure symmetry,'' *Phys. Rev. Lett.*, vol. 109, p. 147401, Oct 2012.

[25] J. Zhang, E. Zallo, B. Höfer, Y. Chen, R. Keil, M. Zopf, S. Böttner, F. Ding, and O. G. Schmidt, ''Electric-Field-Induced Energy Tuning of On-Demand Entangled-Photon Emission from Self-Assembled Quantum Dots,'' *Nano Letters*, vol. 17, no. 1, pp. 501--507, 2017.

[26] M. A. M. Versteegh, M. E. Reimer, K. D. Jöns, D. Dalacu, P. J. Poole, A. Gulinatti, A. Giudice, and V. Zwiller, ''Observation of strongly entangled photon pairs from a nanowire quantum dot,'' *Nature Communications*, vol. 5, p. 5298, 2014.

[27] P. E. Kremer, A. C. Dada, P. Kumar, Y. Ma, S. Kumar, E. Clarke, and B. D. Gerardot, ''Strain-tunable quantum dot embedded in a nanowire antenna,'' *Physical Review B - Condensed Matter and Materials Physics*, vol. 90, no. 20, pp. 1--6, 2014.

[28] J. Claudon, J. Bleuse, N. S. Malik, M. Bazin, P. Jaffrennou, N. Gregersen, C. Sauvan, P. Lalanne, and J. M. Gérard, ''A highly efficient single-photon source based on a quantum dot in a photonic nanowire,'' *Nature Photonics*, vol. 4, no. 3, pp. 174--177, 2010.

[29] D. Dalacu, K. Mnaymneh, J. Lapointe, X. Wu, P. J. Poole, G. Bulgarini, V. Zwiller, and M. E. Reimer, ''Ultraclean emission from inasp quantum dots in defect-free wurtzite inp nanowires,'' *Nano Letters*, vol. 12, no. 11, pp. 5919--5923, 2012.

[30] M. Zeeshan, N. Sherlekar, A. Ahmadi, R. Williams, and M. Reimer, ''Proposed Scheme to Generate Bright Entangled Photon Pairs by Application of a Quadrupole Field to a Single Quantum Dot,'' *Physical Review Letters*, vol. 122, p. 227401, June 2019.

[31] E. Schrödinger, ''Die gegenwärtige situation in der quantenmechanik,'' *Naturwissenschaften*, vol. 23, no. 49, pp. 823--828, 1935.

[32] C. A. Kocher and E. D. Commins, ''Polarization correlation of photons emitted in an atomic cascade,'' *Physical Review Letters*, vol. 18, no. 15, p. 575, 1967.

[33] J. F. Clauser, ''Experimental distinction between the quantum and classical field-theoretic predictions for the photoelectric effect,'' *Physical Review D*, vol. 9, no. 4, p. 853, 1974.

[34] J. F. Clauser, ''Experimental limitations to the validity of semiclassical radiation theories,'' *Physical Review A*, vol. 6, no. 1, p. 49, 1972.

[35] A. Aspect, P. Grangier, and G. Roger, ''Experimental realization of einstein-podolsky-rosen-bohm gedankenexperiment: a new violation of bell's inequalities,'' *Physical review letters*, vol. 49, no. 2, p. 91, 1982.

[36] W. K. Wootters, ''Entanglement of formation of an arbitrary state of two qubits,'' *Physical Review Letters*, vol. 80, no. 10, p. 2245, 1998.

[37] C. Hong and L. Mandel, ''Experimental realization of a localized one-photon state,'' *Physical Review Letters*, vol. 56, no. 1, p. 58, 1986.

[38] A. K. Ekert, ''Quantum cryptography based on bell's theorem,'' *Physical review letters*, vol. 67, no. 6, p. 661, 1991.

[39] E. Knill, R. Laflamme, and G. J. Milburn, ''A scheme for efficient quantum computation with linear optics,'' *nature*, vol. 409, no. 6816, pp. 46--52, 2001.

[40] H. J. Kimble, ''The quantum internet,'' *Nature*, vol. 453, no. 7198, pp. 1023--1030, 2008.

[41] V. Scarani, H. De Riedmatten, I. Marcikic, H. Zbinden, and N. Gisin, ‘‘Four-photon correction in two-photon bell experiments,’’ *The European Physical Journal D-Atomic, Molecular, Optical and Plasma Physics*, vol. 32, no. 1, pp. 129--138, 2005.

[42] X.-L. Wang, L.-K. Chen, W. Li, H.-L. Huang, C. Liu, C. Chen, Y.-H. Luo, Z.-E. Su, D. Wu, Z.-D. Li, *et al.*, ‘‘Experimental ten-photon entanglement,’’ *Physical review letters*, vol. 117, no. 21, p. 210502, 2016.

[43] J. Liu, R. Su, Y. Wei, B. Yao, S. F. C. da Silva, Y. Yu, J. Iles-Smith, K. Srinivasan, A. Rastelli, J. Li, *et al.*, ‘‘A solid-state source of strongly entangled photon pairs with high brightness and indistinguishability,’’ *Nature nanotechnology*, vol. 14, no. 6, pp. 586--593, 2019.

[44] M. Reindl, K. D. Jöns, D. Huber, C. Schimpf, Y. Huo, V. Zwiller, A. Rastelli, and R. Trotta, ‘‘Phonon-assisted two-photon interference from remote quantum emitters,’’ *Nano letters*, vol. 17, no. 7, pp. 4090--4095, 2017.

[45] D. Huber, M. Reindl, Y. Huo, H. Huang, J. S. Wildmann, O. G. Schmidt, A. Rastelli, and R. Trotta, ‘‘Highly indistinguishable and strongly entangled photons from symmetric gaas quantum dots,’’ *Nature communications*, vol. 8, no. 1, pp. 1--7, 2017.

[46] G. Juska, V. Dimastrodonato, L. O. Mereni, A. Gocalinska, and E. Pelucchi, ‘‘Towards quantum-dot arrays of entangled photon emitters,’’ *Nature Photonics*, vol. 7, no. 7, pp. 527--531, 2013.

[47] Y. Chen, M. Zopf, R. Keil, F. Ding, and O. G. Schmidt, ‘‘Highly-efficient extraction of entangled photons from quantum dots using a broadband optical antenna,’’ *Nature Communications*, vol. 9, no. 1, pp. 1--7, 2018.

[48] H. Wang, H. Hu, T.-H. Chung, J. Qin, X. Yang, J.-P. Li, R.-Z. Liu, H.-S. Zhong, Y.-M. He, X. Ding, *et al.*, ‘‘On-demand semiconductor source of entangled photons which simultaneously has high fidelity, efficiency, and indistinguishability,’’ *Physical review letters*, vol. 122, no. 11, p. 113602, 2019.

[49] K. D. Jöns, L. Schweickert, M. A. Versteegh, D. Dalacu, P. J. Poole, A. Gulinatti, A. Giudice, V. Zwiller, and M. E. Reimer, ‘‘Bright nanoscale source of deterministic entangled photon pairs violating bell's inequality,’’ *Scientific Reports*, vol. 7, no. 1, pp. 1--11, 2017.

[50] P. Petroff and S. DenBaars, ‘‘Mbe and mocvd growth and properties of self-assembling quantum dot arrays in iii-v semiconductor structures,’’ *Superlattices and microstructures*, vol. 15, no. 1, p. 15, 1994.

[51] C. Becher, A. Kiraz, P. Michler, A. Imamoğlu, W. V. Schoenfeld, P. M. Petroff, L. Zhang, and E. Hu, ‘‘Nonclassical radiation from a single self-assembled inas quantum dot,’’ *Phys. Rev. B*, vol. 63, p. 121312, Mar 2001.

[52] R. Trotta, J. Martín-Sánchez, J. S. Wildmann, G. Piredda, M. Reindl, C. Schimpf, E. Zallo, S. Stroj, J. Edlinger, and A. Rastelli, ‘‘Wavelength-tunable sources of entangled photons interfaced with atomic vapours,’’ *Nature Communications*, vol. 7, p. 10375, jan 2016.

[53] R. Trotta, J. Martín-Sánchez, I. Daruka, C. Ortix, and A. Rastelli, ‘‘Energy-tunable sources of entangled photons: A viable concept for solid-state-based quantum relays,’’ *Phys. Rev. Lett.*, vol. 114, p. 150502, Apr 2015.

[54] N. Somaschi, V. Giesz, L. De Santis, J. Loredo, M. P. Almeida, G. Hornecker, S. L. Portalupi, T. Grange, C. Antón, J. Demory, *et al.*, ‘‘Near-optimal single-photon sources in the solid state,’’ *Nature Photonics*, vol. 10, no. 5, pp. 340--345, 2016.

[55] G. Bulgarini, M. E. Reimer, M. Bouwes Bavinck, K. D. Jöns, D. Dalacu, P. J. Poole, E. P. A. M. Bakkers, and V. Zwiller, ‘‘Nanowire waveguides launching single photons in a Gaussian mode for ideal fiber coupling,’’ *Nano Letters*, vol. 14, no. 7, pp. 4102--4106, 2014.

[56] M. A. Verheijen, G. Immink, T. de Smet, M. T. Borgström, and E. P. Bakkers, ‘‘Growth kinetics of heterostructured gap- gaas nanowires,’’ *Journal of the American Chemical Society*, vol. 128, no. 4, pp. 1353--1359, 2006.

[57] M. van Weert, ‘‘Quantum dots in vertical nanowire devices,’’ *PhD thesis, TU Delft*, 2010.

[58] M. E. Reimer, G. Bulgarini, N. Akopian, M. Hocevar, M. B. Bavinck, M. A. Verheijen, E. P. A. M. Bakkers, L. P. Kouwenhoven, and V. Zwiller, ‘‘Bright single-photon sources in bottom-up tailored nanowires,’’ *Nature Communications*, vol. 3, p. 737, mar 2012.

[59] G. Bulgarini, M. E. Reimer, T. Zehender, M. Hocevar, E. P. Bakkers, L. P. Kouwenhoven, and V. Zwiller, ‘‘Spontaneous emission control of single quantum dots in bottom-up nanowire waveguides,’’ *Applied Physics Letters*, vol. 100, no. 12, p. 121106, 2012.

[60] A. Fognini, A. Ahmadi, M. Zeeshan, J. T. Fokkens, S. J. Gibson, N. Sherlekar, S. J. Daley, D. Dalacu, P. J. Poole, K. Jöns, V. Zwiller, and M. E. Reimer, ‘‘Dephasing

free photon entanglement with a quantum dot,'' *ACS Photonics*, vol. 6, no. 7, pp. 1656--1663, 2019.

[61] B. D. Gerardot, S. Seidl, P. A. Dalgarno, R. J. Warburton, D. Granados, J. M. Garcia, K. Kowalik, O. Krebs, K. Karrai, A. Badolato, and P. M. Petroff, ''Manipulating exciton fine structure in quantum dots with a lateral electric field,'' *Applied Physics Letters*, vol. 90, no. 4, pp. 1--4, 2007.

[62] M. Korkusinski, M. E. Reimer, R. L. Williams, and P. Hawrylak, ''Engineering photon cascades from multiexciton complexes in a self-assembled quantum dot by a lateral electric field,'' *Phys. Rev. B*, vol. 79, p. 035309, Jan 2009.

[63] K. Kowalik, O. Krebs, A. Lemaître, S. Laurent, P. Senellart, P. Voisin, and J. A. Gaj, ''Influence of an in-plane electric field on exciton fine structure in InAs-GaAs self-assembled quantum dots,'' *Applied Physics Letters*, vol. 86, no. 4, 2005.

[64] K. Kowalik, O. Krebs, A. Lemàtre, B. Eble, A. Kudelski, P. Voisin, S. Seidl, and J. A. Gaj, ''Monitoring electrically driven cancellation of exciton fine structure in a semiconductor quantum dot by optical orientation,'' *Applied Physics Letters*, vol. 91, no. 18, pp. 2005--2008, 2007.

[65] N. Gregersen, T. R. Nielsen, J. Claudon, J.-M. Gérard, and J. Mørk, ''Controlling the emission profile of a nanowire with a conical taper,'' *Opt. Lett.*, vol. 33, pp. 1693--1695, Aug 2008.

[66] N. Gregersen, D. P. S. McCutcheon, J. Mørk, J.-M. Gérard, and J. Claudon, ''A broadband tapered nanocavity for efficient nonclassical light emission,'' *Opt. Express*, vol. 24, pp. 20904--20924, Sep 2016.

[67] H. Y. Ramirez, C. H. Lin, C. C. Chao, Y. Hsu, W. T. You, S. Y. Huang, Y. T. Chen, H. C. Tseng, W. H. Chang, S. D. Lin, and S. J. Cheng, "Optical fine structures of highly quantized ingaas/gaas self-assembled quantum dots," *Phys. Rev. B*, vol. 81, p. 245324, Jun 2010.

[68] E. Poem, J. Shemesh, I. Marderfeld, D. Galushko, N. Akopian, D. Gershoni, B. D. Gerardot, A. Badolato, and P. M. Petroff, "Polarization sensitive spectroscopy of charged quantum dots," *Phys. Rev. B*, vol. 76, p. 235304, Dec 2007.

[69] S. Birner, T. Zibold, T. Andlauer, T. Kubis, M. Sabathil, A. Trellakis, and P. Vogl, "nextnano: General purpose 3-d simulations," *IEEE Transactions on Electron Devices*, vol. 54, pp. 2137--2142, Sept 2007.

[70] G. Bester, S. Nair, and A. Zunger, "Pseudopotential calculation of the excitonic fine structure of million-atom self-assembled $\mathrm{in}_{1-x}\mathrm{ga}_x\mathrm{As}$/GaAs quantum dots," *Phys. Rev. B*, vol. 67, p. 161306, Apr 2003.

[71] B. D. Gerardot, D. Brunner, P. A. Dalgarno, P. Öhberg, S. Seidl, M. Kroner, K. Karrai, N. G. Stoltz, P. M. Petroff, and R. J. Warburton, "Optical pumping of a single hole spin in a quantum dot," *Nature*, vol. 451, no. 7177, pp. 441--444, 2008.

[72] M. Abbarchi, C. A. Mastrandrea, T. Kuroda, T. Mano, K. Sakoda, N. Koguchi, S. Sanguinetti, A. Vinattieri, and M. Gurioli, "Exciton fine structure in strain-free GaAs/$\mathrm{al}_{0.3}\mathrm{ga}_{0.7}\mathrm{As}$ quantum dots: Extrinsic effects," *Phys. Rev. B*, vol. 78, p. 125321, Sep 2008.

[73] J. A. Czaban, D. A. Thompson, and R. R. LaPierre, "Gaas core−shell nanowires for photovoltaic applications," *Nano Letters*, vol. 9, no. 1, pp. 148--154, 2009. PMID: 19143502.

[74] T. Bryllert, L.-E. Wernersson, T. Löwgren, and L. Samuelson, ‘‘Vertical wrap-gated nanowire transistors,’’ *Nanotechnology*, vol. 17, no. 11, pp. S227--S230, 2006.

[75] H. T. Ng, J. Han, T. Yamada, P. Nguyen, Y. P. Chen, and M. Meyyappan, ‘‘Single crystal nanowire vertical surround-gate field-effect transistor,’’ *Nano Letters*, vol. 4, no. 7, pp. 1247--1252, 2004.

[76] M. H. M. van Weert, N. Akopian, U. Perinetti, M. P. van Kouwen, R. E. Algra, M. A. Verheijen, E. P. A. M. Bakkers, L. P. Kouwenhoven, and V. Zwiller, ‘‘Selective excitation and detection of spin states in a single nanowire quantum dot,’’ *Nano Letters*, vol. 9, no. 5, pp. 1989--1993, 2009.

[77] A. W. Elshaari, I. E. Zadeh, A. Fognini, M. E. Reimer, D. Dalacu, P. J. Poole, V. Zwiller, and K. D. Jöns, ‘‘On-chip single photon filtering and multiplexing in hybrid quantum photonic circuits,’’ *Nature communications*, vol. 8, no. 1, pp. 1--8, 2017.

[78] A. Tarraf, J. Daleiden, S. Irmer, D. Prasai, and H. Hillmer, ‘‘Stress investigation of PECVD dielectric layers for advanced optical MEMS,’’ *Journal of Micromechanics and Microengineering*, vol. 14, pp. 317--323, nov 2003.

[79] H. Saito, K. Nishi, and S. Sugou, ‘‘Influence of GaAs capping on the optical properties of InGaAs/GaAs surface quantum dots with 1.5 µm emission,’’ *Applied Physics Letters*, vol. 73, pp. 2742--2744, Nov. 1998.

[80] L. M. Duan, M. D. Lukin, J. I. Cirac, and P. Zoller, ‘‘Long-distance quantum communication with atomic ensembles and linear optics,’’ *Nature*, vol. 414, no. 6862, pp. 413--418, 2001.

[81] I. Newton, ''1704,'' *Opticks. London: Smith and Walford*, 1952.

[82] G. N. Cantor, *Optics after Newton: theories of light in Britain and Ireland, 1704-1840*. Manchester University Press, 1983.

[83] C. Huygens, ''Traité de la lumiere (leiden, 1690),'' *Oeuvres completes XIX*, vol. 1737, 1912.

[84] T. Young, ''On the theory of light and colors (the 1801 bakerian lecture) philosophical transactions of the royal society of london,'' *Philosophical transactions of the Royal Society of London*, 1802.

[85] J. C. Maxwell, ''Viii. a dynamical theory of the electromagnetic field,'' *Philosophical transactions of the Royal Society of London*, no. 155, pp. 459--512, 1865.

[86] H. Hertz, ''Ueber einen einfluss des ultravioletten lichtes auf die electrische entladung,'' *Annalen der Physik*, vol. 267, no. 8, pp. 983--1000, 1887.

[87] J. J. Thomson *et al.*, *Cathode rays.* US Government Printing Office, 1897.

[88] J. J. Thomson, ''Lviii. on the masses of the ions in gases at low pressures,'' *The London, Edinburgh, and Dublin philosophical magazine and journal of science*, vol. 48, no. 295, pp. 547--567, 1899.

[89] A. Einstein, ''Uber einen die erzeugung und verwandlung des lichtes betreffenden heuristischen gesichtspunkt,'' *Annalen der physik*, vol. 322, no. 6, pp. 132--148, 1905.

[90] G. N. Lewis, ''The conservation of photons,'' *Nature*, vol. 118, no. 2981, pp. 874--875, 1926.

[91] L. d. Broglie, ''Diss. paris 1924,'' *Phil. Mag*, vol. 47, p. 446, 1924.

[92] J. P. Dowling and G. J. Milburn, ‘‘Quantum technology: the second quantum revolution,’’ *Philosophical Transactions of the Royal Society of London. Series A: Mathematical, Physical and Engineering Sciences*, vol. 361, no. 1809, pp. 1655--1674, 2003.

[93] P. Shadbolt, J. C. Mathews, A. Laing, and J. L. O’brien, ‘‘Testing foundations of quantum mechanics with photons,’’ *Nature Physics*, vol. 10, no. 4, pp. 278--286, 2014.

[94] O. Gazzano, S. Michaelis De Vasconcellos, C. Arnold, A. Nowak, E. Galopin, I. Sagnes, L. Lanco, A. Lemaître, and P. Senellart, ‘‘Bright solid-state sources of indistinguishable single photons,’’ *Nature Communications*, vol. 4, 2013.

[95] J. D. Plumhof, V. Křápek, F. Ding, K. D. Jöns, R. Hafenbrak, P. Klenovský, A. Herklotz, K. Dörr, P. Michler, A. Rastelli, and O. G. Schmidt, ‘‘Strain-induced anticrossing of bright exciton levels in single self-assembled gaas/al$_x$ga$_{1-x}$as and in$_x$ga$_{1-x}$as/gaas quantum dots,’’ *Phys. Rev. B*, vol. 83, p. 121302, Mar 2011.

[96] C. L. Salter, R. M. Stevenson, I. Farrer, C. A. Nicoll, D. A. Ritchie, and A. J. Shields, ‘‘An entangled-light-emitting diode,’’ *Nature*, vol. 465, pp. 594--597, 2010.

[97] E. Moreau, I. Robert, L. Manin, V. Thierry-Mieg, J. M. Gérard, and I. Abram, ‘‘Quantum cascade of photons in semiconductor quantum dots,’’ *Phys. Rev. Lett.*, vol. 87, p. 183601, Oct 2001.

[98] V. Křápek, P. Klenovský, and T. Šikola, ‘‘Excitonic fine structure splitting in type-ii quantum dots,’’ *Phys. Rev. B*, vol. 92, p. 195430, Nov 2015.

[99] R. Singh and G. Bester, ‘‘Nanowire quantum dots as an ideal source of entangled photon pairs,’’ *Phys. Rev. Lett.*, vol. 103, p. 063601, Aug 2009.

[100] R. Seguin, A. Schliwa, S. Rodt, K. Pötschke, U. W. Pohl, and D. Bimberg, ''Size-dependent fine-structure splitting in self-organized InAs/GaAs quantum dots,'' *Phys. Rev. Lett.*, vol. 95, p. 257402, Dec 2005.

[101] M. Zieliński, ''Excitonic fine structure of elongated inas/inp quantum dots,'' *Phys. Rev. B*, vol. 88, p. 155319, Oct 2013.

[102] R. Singh and G. Bester, ''Effects of atomic ordering on the electronic and optical properties of self-assembled in$_x$ga$_{1-x}$as/gaas semiconductor quantum dots,'' *Phys. Rev. B*, vol. 84, p. 241402, Dec 2011.

[103] A. J. Bennett, M. A. Pooley, R. M. Stevenson, M. B. Ward, R. B. Patel, A. Boyer de la Giroday, N. Skoeld, I. Farrer, C. A. Nicoll, D. A. Ritchie, and A. J. Shields, ''Electric-field-induced coherent coupling of the exciton states in a single quantum dot,'' *Nat Phys*, vol. 6, pp. 947--950, 2010.

[104] W. Langbein, P. Borri, U. Woggon, V. Stavarache, D. Reuter, and A. D. Wieck, ''Control of fine-structure splitting and biexciton binding in in$_x$ga$_{1-x}$As quantum dots by annealing,'' *Phys. Rev. B*, vol. 69, p. 161301, Apr 2004.

[105] G. S. Solomon, M. Pelton, and Y. Yamamoto, ''Single-mode spontaneous emission from a single quantum dot in a three-dimensional microcavity,'' *Phys. Rev. Lett.*, vol. 86, pp. 3903--3906, Apr 2001.

[106] Y. Ma, P. E. Kremer, and B. D. Gerardot, ''Efficient photon extraction from a quantum dot in a broad-band planar cavity antenna,'' *Journal of Applied Physics*, vol. 115, no. 2, 2014.

[107] P. Hawrylak, ''Excitonic artificial atoms: Engineering optical properties of quantum dots,'' *Physical Review B*, vol. 60, no. 8, pp. 5597--5608, 1999.

[108] S. Strauf, N. G. Stoltz, M. T. Rakher, L. A. Coldren, P. M. Petroff, and D. Bouwmeester, ''High-frequency single-photon source with polarization control,'' *Nature Photonics*, vol. 1, no. 12, pp. 704--708, 2007.

[109] Y. Chen, I. E. Zadeh, K. D. Jï?‘½ns, A. Fognini, M. E. Reimer, J. Zhang, D. Dalacu, P. J. Poole, F. Ding, V. Zwiller, and O. G. Schmidt, ''Controlling the exciton energy of a nanowire quantum dot by strain fields,'' *Applied Physics Letters*, vol. 108, no. 18, pp. 1--6, 2016.

[110] D. C. Burnham and D. L. Weinberg, ''Observation of simultaneity in parametric production of optical photon pairs,'' *Physical Review Letters*, vol. 25, no. 2, p. 84, 1970.

List of Publications

Journal Articles

1. M. Zeeshan, N. Sherlekar, A. Ahmadi, R. Williams, and M. Reimer, "Proposed Scheme to Generate Bright Entangled Photon Pairs by Application of a Quadrupole Field to a Single Quantum Dot" *Physical Review Letters*, vol. 122, p. 227401, June 2019.

2. A. Fognini, A. Ahmadi, M. Zeeshan, J. T. Fokkens, S. J. Gibson, N. Sherlekar, S. J.Daley, D. Dalacu, P. J. Poole, K. Jöns, V. Zwiller, and M. E. Reimer, "Dephasing free photon entanglement with a quantum dot," *ACS Photonics*, vol. 6, no. 7, pp. 1656--1663, 2019.

3. M. Zeeshan, D. Dalacu, P. J. Poole, S. J. Gibson and M. E. Reimer, "Quadrupole electric feld induced fine structure splitting tuning of the InAsP/InP quantum dot nanowire source," *in preparation*.

Conferences and proceedings:

1. M. Zeeshan, N. Sherlekar, S. J. Gibson, A. Ahmadi and M. E. Reimer, "Unique qaudrupole field to generate high efficiency entangled photon pairs in a single quantum dot," *Conference for Quantum Information and Quantum Control (CQIQC-VII)*, August 2017, Toronto, Canada.

2. M. Zeeshan, S. J. Gibson, N. Sherlekar, and M. E. Reimer, "Nanoscale Tunable Quantum light sources," *Canadian Graduate Quantum Conference*, June 2018, Vancouver, Canada.

3. M. Zeeshan, N. Sherlekar, A. Ahmadi, S. J. Gibson, and M. E. Reimer, "Fine structure splitting energy correction for single quantum dot via quadrupole potential," *Nanophotonics and Micro/Nano Optics International Conference*, October 2018, Rome, Italy.

APPENDICES

Appendix A

Fabrication recipe for a vertical nanowire device

A.1 Fabrication steps with UV lithography

This section contains the step by step fabrication process for the fabrication of a vertical nanowire gated device by a UV lithography. The InAsP/InP QD/nanowire sample is grown by our collaborators Dan Dalacu and Philip Poole at National Research Council, Canada and the main steps can be divided into four sections.

Dielectric Deposition

- Rinsing a nanowire sample for a 30' sec in an IPA and DI water
- Depositing PECVD SiO_2 200 nm at 330 °C

Selected area removal of dielectric

- Rinsing the SiO_2 coated nanowire sample for a 30' sec in an IPA and DI water
- Applying HMDS vapor layer
- Spin coating PMGI 5' 500 rpm/ 60' 5000 rpm
- Baking for 3 min at 180 °C
- Measuring the resist thickness by Filmetric F-50 optical UV reflectometer
- Spin coating SF1805 5' 500 rpm/ 60' 5000 rpm
- Baking for 120' at 150 °C
- Measuring the resist thickness by Filmetric F-50 optical UV reflectometer
- Exposing the UV pattern by the mask-less MLA 150 Heidelberg UV-lithography with a dose of 120 mJ/cm^2
- 30' develop MF-319
- Rinsing in DI for 1' minute to stop the development

Defining gates

- Rinsing the nanowire sample for a 30' sec in an IPA and DI water
- Applying HMDS vapor layer
- Spin coating PMGI 5' 500 rpm/ 60' 5000 rpm

- Baking for 3 min at 180 °C
- Measuring the resist thickness by Filmetric F-50 optical UV reflectometer
- Spin coating SF1805 5' 500 rpm/ 60' 5000 rpm
- Baking for 120' at 150 °C
- Measuring the resist thickness by Filmetric F-50 optical UV reflectometer
- Exposing the UV pattern by the mask-less MLA 150 Heidelberg UV-lithography with a dose of 120 mJ/cm^2
- 30' sec develop MF-319
- Rinsing in a DI for 5' minute to stop the development
- Optical inspection

Metal deposition and liftoff

- Descum the sample
- Deposit 15 nm Ti / 80 nm Au by e-beam thermal evaporator at a deposition rate of---- at room temperature.
- Lift-off by dipping the sample in a PG remover for an overnight. Sometimes heating the sample at 80 °C helps the lift-off process.
- Optical/electrical inspection

A.2 Fabrication steps with e-beam lithography

This section contains the step by step fabrication process for the fabrication of a vertical nanowire gated device by an e-beam lithography. The main steps can be divided into four sections.

Dielectric deposition

- Rinsing a nanowire sample for a 30' sec in an IPA and DI water
- Depositing PECVD SiO_2 200 nm at 330 °C

Defining gates

- Rinsing a nanowire sample for a 30' sec in an IPA and DI water
- Spin coating MMA 8.5 polymer 5' 500 rpm/ 60' 3000 rpm
- Baking for 3 min at 180 °C
- Repeating the previous two steps twice
- Spin coating PMMA A6-A6 resist 5' 500 rpm/ 60' 2500 rpm
- Baking for 3 min at 150 °C
- Spin coating Electra-92 conducive polymer 60' sec 3000 rpm
- Exposing the e-beam pattern by a JOEL 100 kV lithography system
- Rinsing the sample in DI water 60' sec to remove the polymer

- Development in a 3:7 DI/IPA solvent at 5 °C for 5' min
- Rinsing in DI for 5' minutes to stop the development
- Optical inspection

Metal deposition and lift-off

- Descum the sample
- Deposit 15 nm Ti / 80 nm Au by e-beam thermal evaporator at a deposition rate of---- at room temperature.
- Lift-off by dipping the sample in a PG remover for an overnight. Sometimes heating the sample at 80 °C helps the lift-off process.
- Optical inspection

Selective area removal of the dielectric

- Rinsing a nanowire sample for a 30' sec in an IPA and DI water
- Spin coating MMA 8.5 polymer 5' 500 rpm/ 60' 3000 rpm
- Baking for 3 min at 180 °C
- Repeating the previous two steps twice
- Spin coating PMMA A6-A6 resist 5' 500 rpm/ 60' 2500 rpm
- Baking for 3 min at 150 °C

- Spin coating Electra-92 conducive polymer 60' sec 3000 rpm
- Exposing the e-beam pattern by a JOEL 100 kV lithography system
- Rinsing the sample in DI water 60' sec to remove the polymer
- Development in a 3:7 DI/IPA solvent at 5 °C for 5' min
- Rinsing in DI for 5' minutes to stop the development
- Optical/SEM/electrical inspection

Appendix B

Codes

B.1 Next Nano simualtion code

This is an input file for a quantum dot (core/shell structure). Variables start with % sign.

The syntax for template files is described at:

http://www.nextnano.com/nextnano3/nextnanomat/template.htm

```
1
2  !****************************************************************************!
3  !                                                                            !
4                                       !
5  !****************************************************************************!
6
7
8  !+++++++++++++++++++++++++++++++++++++++++++++++++++++++++++++++++++++++++++++
9
10 !-----------------------------------------------------------------------------
11 ! We have to be careful about the value of a variable.
12 ! Should it be regarded as a string (default),
13 ! or as a function ('%FunctionParser␣=␣yes')?
14 !-----------------------------------------------------------------------------
```

```
15
16 !%AloySweepActive       = yes                                               ! Sweep over alloy
       concentrations.
17  %AloySweepActive       = no                                                ! Do not wweep
       over alloy concentrations.
18
19 !--------------------------------------------------------------------------
20 ! Treat variables as strings (default): e.g. %variable1 = %zmin %zmax        ! '%zmin␣%zmax' is
       treated as a string
21 !                                            %variable2 = 2.5d0              ! '2.5d0'       is
       treated as a string
22 !                                            %variable3 = 2.5                ! '2.5'         is
       treated as a string without exponent 'e0'
23 !--------------------------------------------------------------------------
24  %grid_spacing   = 0.5                                                      ! grid spacing
                                     (DisplayUnit:nm)
25
26 !--------------------------------------------------------------------------
27 ! From now on, evaluate all functions:  e.g. %variable1 = %zmin %zmax        ! '%zmin␣%zmax' is
       treated as a formula (which will produce an error in this case)
28 !                                            %variable2 = 2.5                ! '2.5' is
      converted to a real number including exponent 'e0'
29 !--------------------------------------------------------------------------
30  %FunctionParser     = yes                                                  ! use function
       parser (DoNotShowInUserInterface)
31
32  %CoreOuterRadius    = 15                                                   ! ==> GaAs core
       radius          (DisplayUnit:nm) (RangeOfValues:From=5.0,To=15.0,Step=2.0) (ListOfValues
       :5,7,9,11,13,15)
33  %ShellThickness     = 110                                                  ! ==> thickness of
        AlGaAs shell (DisplayUnit:nm) (RangeOfValues:From=10.0,To=15.0,Step=1.0) (ListOfValues
       :10,15)
34  %dielecthickness    = 150
35  %ShellOuterRadius   = %CoreOuterRadius + %ShellThickness                   ! AlGaAs shell
       radius           (DisplayUnit:nm) (DoNotShowInUserInterface)
36  %dielecOuterRadius  = %CoreOuterRadius + %ShellThickness + %dielecthickness
37  %Rsintheta          = %dielecOuterRadius * sin(1.2217)
38  %Rcostheta          = %dielecOuterRadius * cos(1.2217)
```

```
39  %boundary           = %dielecOuterRadius + 1                                 ! device_width/2
                       (DisplayUnit:nm) (DoNotShowInUserInterface)
40  !%x1nodes            = ( 2 * %boundary ) / %grid_spacing - 1                  ! number of nodes
        (DoNotShowInUserInterface)
41  !%y1nodes            = ( 2 * %boundary ) / %grid_spacing - 1                  ! number of nodes
        (DoNotShowInUserInterface)
42 !----------------------------------------------------------------------------
43 ! If you need an integer, then call the variable '%INT(<name>)'.
44 !----------------------------------------------------------------------------
45 !%INT(x1nodes)       = %x1nodes                                             ! number of nodes
     (integer) <== it is necessary to convert it to an integer (DoNotShowInUserInterface)
46 !%INT(y1nodes)       = %y1nodes                                             ! number of nodes
     (integer) <== it is necessary to convert it to an integer (DoNotShowInUserInterface)
47
48  %AlGaAsAlloy        = 0.33                                                 ! ==> Al alloy
      content (bowing!) (DisplayUnit:) (ListOfValues:0.25,0.30,0.33)
49
50  %temperature        = 4                                                    ! ==> temperature
          (DisplayUnit:K) (ListOfValues:4,100,200,300,350) (RangeOfValues:From=10,To=340,Step
      =50)
51
52 !++++++++++++++++++++++++++++++++++++++++++++++++++++++++++++++++++++++++++++
53
54 !---------------------------------------------------------------------------!
55 $numeric-control                                                            !
56  simulation-dimension            = 2                                         !
57  zero-potential                  = no                                      ! do not solve
      initial Poisson equation
58 !zero-potential                  = no                                        !        solve
     initial Poisson equation
59
60 !schroedinger-masses-anisotropic = yes ! discretization includes   offdiagonal effective-mass
     tensor components
61  schroedinger-masses-anisotropic = box ! discretization includes   offdiagonal effective-mass
      tensor components (box-integration method)
62 !schroedinger-masses-anisotropic = no  ! discretization includes only diagonal effective-mass
     tensor components
63
```

```
64  !+++++++++++++++++++++++++++++++++++++++++++++++++++++++++++++++++++++++++++!
65  ! a) ARPACK eigenvalue solver
66  !+++++++++++++++++++++++++++++++++++++++++++++++++++++++++++++++++++++++++++!
67   schroedinger-1band-ev-solv      = ARPACK                                  ! 'lapack', 'laband
        ', 'arpack', 'chearn'
68   schroedinger-1band-iterations   = 1000     ! for ARPACK!!!
69  ! schroedinger-kp-ev-solv          = ARPACK
70  ! schroedinger-kp-iterations       =  30
71  ! schroedinger-kp-residual         =  1.0d-10
72  ! schroedinger-kp-more-ev          =  6
73  !+++++++++++++++++++++++++++++++++++++++++++++++++++++++++++++++++++++++++++!
74
75  !+++++++++++++++++++++++++++++++++++++++++++++++++++++++++++++++++++++++++++!
76  ! b) chearn eigenvalue solver
77  !+++++++++++++++++++++++++++++++++++++++++++++++++++++++++++++++++++++++++++!
78  !schroedinger-1band-ev-solv      = chearn                                  ! 'lapack', 'laband
       ', 'arpack', 'chearn'
79   schroedinger-chearn-el-cutoff   = 0.150d0                                 ! [eV] for chearn
        eigenvalue solver (This is an optimized value for this tutorial!)
80  !schroedinger-1band-iterations   = 10       ! for chearn!!!
81  !schroedinger-chearn-el-cutoff   = 5d0
82  !schroedinger-chearn-hl-cutoff   = 5d0
83  !+++++++++++++++++++++++++++++++++++++++++++++++++++++++++++++++++++++++++++!
84
85  !varshni-parameters-on           = no                                      ! no temperature
       dependent band gaps
86   varshni-parameters-on           = yes                                     !    temperature
        dependent band gaps
87   schroedinger-1band-residual          = 1d-7     ! default: 1d-12             Poison editing
88   schroedinger-poisson-precor-residual = 1d-9     ! default: 1d-9            !  Poison editing
89   discontinous-charge-density-1band    = yes                                ! Poison editing
        only relevant for 1D/2D quantum mechanical calculation
90  !---------------------------------------------------------------------------
91
92  $end_numeric-control                                                       !
93  !--------------------------------------------------------------------------!
94
95  !****** OVERALL SIMULATION PARAMETERS *************************************!
```

```
96
97  !----------------------------------------------------------------------------!
98  ! orientation specifies the axes which are simulated                         !
99  ! e.g. in 1D, 0 0 1 means along z axis                                       !
100 !----------------------------------------------------------------------------!
101 $simulation-dimension                                                        !
102  dimension   = 2                                                             !
103  orientation = 1 1 0                                                         ! simulation in (x,
     y) plane
104 $end_simulation-dimension                                                    !
105 !----------------------------------------------------------------------------!
106
107 !----------------------------------------------------------------------------!
108 $global-parameters                                                           !
109  lattice-temperature = %temperature                                          ! 4.2 Kelvin
110 !lattice-temperature = 300d0                                                 ! 300 Kelvin
111 !lattice-temperature = 4.2d0                                                 ! 4.2 Kelvin
112 $end_global-parameters                                                       !
113 !----------------------------------------------------------------------------!
114
115 !----------------------------------------------------------------------------!
116 ! Flow control is the possibility to control the actual computation.         !
117 !----------------------------------------------------------------------------!
118 $simulation-flow-control                                                     !
119 !flow-scheme         = 2                                                      ! 2 = quantum
    mechanical calculation
120  flow-scheme         = 2                                                      ! 3 = quantum
     mechanical calculation, calculate eigenstates only
121  strain-calculation  = no-strain                                             ! raw-strain-in  or
       homogeneous-strain  or  strain-minimization  or  zero-strain-amorphous
122 $end_simulation-flow-control                                                 !
123 !----------------------------------------------------------------------------!
124
125 !----------------------------------------------------------------------------!
126 ! The domain type in 1D usually is 0 0 1 which means that the simulated      !
127 ! dimension is the 0 0 1 axis.                                               !
128 ! z-coordinates specify the size of the simulated region in [nm].            !
129 ! pseudomorphic-on specifies the substrate material and therefore            !
```

```
130 ! determines strain.                                                          !
131 !-----------------------------------------------------------------------------!
132 $domain-coordinates                                                           !
133  domain-type             = 1 1 0                                              !
134  x-coordinates           = -%boundary %boundary                               !
135  y-coordinates           = -%boundary %boundary                               !
136 !growth-coordinate-axis = 0 0 1                                               !
137  pseudomorphic-on        = GaAs                                               !
138 $end_domain-coordinates                                                       !
139 !-----------------------------------------------------------------------------!
140
141 !****** END OVERALL SIMULATION PARAMETERS **********************************!
142
143
144 !****** REGIONS AND CLUSTERS ***********************************************!
145
146 !-----------------------------------------------------------------------------!
147 ! You specified n regions in the simulation area. If they do not              !
148 ! completely fill the simulation area, the resulting rest area is             !
149 ! automatically assigned as region number n+1.                                !
150 ! So you ALWAYS have one region more than you actually specified (even if     !
151 ! they completely fill the simulation area).                                  !
152 ! We could also set any region to a higher priority which means that it       !
153 ! would be on top of the lower priority region.                               !
154 !-----------------------------------------------------------------------------!
155 $regions                                                                      !
156
157  !---------------------------------------
158  ! left half circle
159  !---------------------------------------
160  region-number = 1    base-geometry = semiellipse region-priority = 3       ! GaAs
161  semi-ellipse-base = 0d0   0d0   -14d0 14d0
162  semi-ellipse-top  = -%CoreOuterRadius  0d0                                         !
163                                                                               !
164  !---------------------------------------
165  ! right half circle
166  !---------------------------------------
167  region-number = 2    base-geometry = semiellipse region-priority = 3       ! GaAs
```

```
168 semi-ellipse-base = 0d0   0d0   -14d0 14d0
169 semi-ellipse-top  = %CoreOuterRadius 0d0                                          !
170                                                                            !
171 !-------------------------------------
172 ! left half circle
173 !-------------------------------------
174 region-number = 3    base-geometry = semiellipse region-priority = 2       ! AlGaAs
175 semi-ellipse-base = 0d0   0d0   -%ShellOuterRadius %ShellOuterRadius       !
176 semi-ellipse-top  = -%ShellOuterRadius  0d0                                       !
177                                                                            !
178 !-------------------------------------
179 ! right half circle
180 !-------------------------------------
181 region-number = 4    base-geometry = semiellipse region-priority = 2       ! AlGaAs
182 semi-ellipse-base = 0d0   0d0   -%ShellOuterRadius %ShellOuterRadius
                                       !
183 semi-ellipse-top  = %ShellOuterRadius 0d0                                !
184 !-------------------------------------
185 ! left half dielectric
186 !-------------------------------------
187 region-number = 5    base-geometry = semiellipse  region-priority = 1
188 x-coordinates = 0d0  0d0  -%dielecOuterRadius  %dielecOuterRadius          ! Dielectric
189 semi-ellipse-base = 0d0   0d0   -%dielecOuterRadius %dielecOuterRadius      ! zeeshan
                                !
190 semi-ellipse-top =  -%dielecOuterRadius  0d0
191 !-------------------------------------
192 ! right half dielectric
193 !-------------------------------------
194 region-number = 6    base-geometry = semiellipse  region-priority = 1
195 x-coordinates = 0d0  0d0  -%dielecOuterRadius  %dielecOuterRadius          ! Dielectric
196 semi-ellipse-base = 0d0   0d0   -%dielecOuterRadius %dielecOuterRadius     ! zeeshan
                                  !
197 semi-ellipse-top = %dielecOuterRadius 0d0                                  !
198 !-------------------------------------
199 ! Electrical gates
200 !-------------------------------------
201 region-number = 7     base-geometry = semiellipse   region-priority = 4    !  1.0 nm Top Gate
```

```
202  semi-ellipse-base = -%Rcostheta %Rcostheta %Rsintheta %Rsintheta           !  Top zeeshan
                                  !
203  semi-ellipse-top = 0d0 %dielecOuterRadius
204
205  region-number = 8     base-geometry = semiellipse   region-priority = 4    !  1.0 nm Left Gate
206  semi-ellipse-base = -%Rsintheta   -%Rsintheta   -%Rcostheta %Rcostheta     !  left zeeshan
                                !
207  semi-ellipse-top  = -%dielecOuterRadius 0d0
208
209  region-number = 9     base-geometry = semiellipse   region-priority = 4    !  1.0 nm Right
         Gate
210  semi-ellipse-base =  %Rsintheta   %Rsintheta   -%Rcostheta %Rcostheta      ! right zeeshan
                                  !
211  semi-ellipse-top  =  %dielecOuterRadius 0d0
212
213  region-number = 10    base-geometry = semiellipse   region-priority = 4    !  1.0 nm Bottom
         Gate
214  semi-ellipse-base = -%Rcostheta   %Rcostheta   -%Rsintheta -%Rsintheta     !  bottom zeeshan
                                   !
215  semi-ellipse-top  = 0d0 -%dielecOuterRadius
216
217 $end_regions                                                                 !
218 !----------------------------------------------------------------------------!
219 $grid-specification                                                          !
220  grid-type      =    1 1 0                                                   !
221
222  x-grid-lines   = -%boundary  -%dielecOuterRadius  -%Rsintheta   -%ShellOuterRadius     -%
         Rcostheta   -%CoreOuterRadius     0d0     %CoreOuterRadius  %Rcostheta    %
         ShellOuterRadius      %Rsintheta  %dielecOuterRadius  %boundary   ! [nm]
223  x-nodes        =            1                    2           20                     24
                  64                   20       20                  64           24
                        20               2                    1             !
224  x-grid-factors =            1d0                  1d0         1d0                    1d0
                  1d0                  1d0      1d0                 1d0          1d0
                       1d0             1d0                  1d0          !
225
226  y-grid-lines   = -%boundary  -%dielecOuterRadius  -%Rsintheta   -%ShellOuterRadius     -%
         Rcostheta      -14d0              0d0      14d0            %Rcostheta    %ShellOuterRadius
```

```
       %Rsintheta  %dielecOuterRadius  %boundary   ![nm]
227  y-nodes        =            1                    2           20                   24
                  64                   20      20                   64           24
                  20           2                    1              !
228  y-grid-factors =           1d0                  1d0          1d0                  1d0
                 1d0                  1d0     1d0                  1d0           1d0
                   1d0          1d0                  1d0           !
229
230
231 $end_grid-specification                                                     !
232 !---------------------------------------------------------------------------!
233 ! For every boundary between regions, there has to exist a grid line. And   !
234 ! between these grid lines there are a certain number of nodes which        !
235 ! determine the resolution of the simulated region. In order to specify     !
236 ! inhomogeneous grids you can use a grid factor different from one. This    !
237 ! means that the distance between each node is increased by this factor     !
238 ! from i to i+1.                                                            !
239 !---------------------------------------------------------------------------!
240  !$end_domain-coordinates  ! BIRNER
241 !---------------------------------------------------------------------------!
242
243 !---------------------------------------------------------------------------!
244 ! A cluster is a group of regions. Every region has to belong to a cluster  !
245 ! but a cluster can contain several regions. This is useful if you want to  !
246 ! construct more complicated objects of more regions which have the same    !
247 ! material.                                                                 !
248 !---------------------------------------------------------------------------!
249 $region-cluster                                                             !
250
251  cluster-number = 1    region-numbers = 1 2                                 ! GaAs
252  cluster-number = 2    region-numbers = 3 4                                 ! AlGaAs
253  cluster-number = 3    region-numbers = 5 6                                 ! dielectric
254  cluster-number = 4    region-numbers = 7                                   ! Top Gate
255  cluster-number = 5    region-numbers = 8                                   ! Left Gate
256  cluster-number = 6    region-numbers = 9                                   ! Right Gate
257  cluster-number = 7    region-numbers = 10                                  ! Bottom Gate
258  cluster-number = 8    region-numbers = 11                                  ! Air
259 $end_region-cluster                                                         !
```

```
260 !---------------------------------------------------------------------------!
261
262 !****** END REGIONS AND CLUSTER ********************************************!
263
264
265 !****** MATERIALS AND ALLOY PROFILES ****************************************
266
267 !---------------------------------------------------------------------------!
268 ! All materials used in the simulation region are listed here. A material   !
269 ! has to be assigned to each cluster.                                       !
270 ! In the case of alloys an alloy function has to be specified.              !
271 !---------------------------------------------------------------------------!
272 $material                                                                   !
273
274  material-number = 1                                                        !
275  material-name   = GaAs
276  cluster-numbers = 1                                                        !
277
278  material-number = 2                                                        !
279  material-name   = Al(x)Ga(1-x)As
280  cluster-numbers = 2                                                        !
281  alloy-function  = constant
282
283  material-number = 3                                                        !
284  material-name   = Al2O3    ! BIRNER
285  cluster-numbers = 3                                                        !
286
287  material-number = 4                                                        ! 1.0 nm Gate
288  material-name   = Metal
289  cluster-numbers = 4 5 6 7
290
291  material-number = 5                                                        ! boundary is Air
292  material-name   = Air
293  cluster-numbers = 8                                                        !
294 $end_material                                                               !
295 !---------------------------------------------------------------------------!
296
297 !---------------------------------------------------------------------------!
```

```
298 $alloy-function                                                              !
299                                                                              !
300  material-number        = 2      ! BIRNER                                    !
301  function-name          = constant
302  xalloy                 = %AlGaAsAlloy                                       ! Al0.33Ga0.67As
303
304  alloy-sweep-active          = %AloySweepActive                              !
305 !alloy-sweep-active          = yes                                           ! to switch on
        alloy sweep
306 !alloy-sweep-active          = no                                            ! to switch off
        alloy sweep
307  alloy-sweep-step-size       = -0.03d0                                       ! increase alloy
      concentration in each step by -0.03. (This value can also be negative, i.e. decrease alloy
       concentration.)
308  alloy-sweep-number-of-steps = 11                                            ! number of alloy
      sweep steps
309                                                                              !
310 $end_alloy-function                                                          !
311 !----------------------------------------------------------------------------!
312 !----------------------------------------------------------------------------!
313 ! Here we are overwriting the database entries for GaAs.                     !
314 ! E_gap = 2.979 - 1.346 - 1/3 * 0.341 = 1.519333 eV   (  0 K)                !
315 ! E_gap = 2.882 - 1.346 - 1/3 * 0.341 = 1.422333 eV   (300 K)                !
316 ! E_gap: 1.42 eV (Greg Snider)
317 !----------------------------------------------------------------------------!
318 $binary-zb-default                                                           !
319  binary-type                 = GaAs-zb-default                               !
320  apply-to-material-numbers    = 1 2                                          !
321  conduction-band-masses       = 0.067d0  0.067d0  0.067d0   ! DEFAULT       ! Gamma cb1 - 1st
      principal axis, 2nd, 3rd
322                                1.9d0    0.0754d0 0.0754d0                   ! L     cb2 - 1st
                                   principal axis, 2nd, 3rd - m_l m_t m_t
323                                1.3d0    0.23d0   0.23d0                     ! X     cb3 - 1st
                                   principal axis, 2nd, 3rd - m_l m_t m_t
324  valence-band-masses          = 0.500d0  0.500d0  0.500d0   ! DEFAULT       ! heavy hole
325                                0.068d0  0.068d0  0.068d0   ! DEFAULT       ! light hole
326                                0.172d0  0.172d0  0.172d0   ! DEFAULT       ! split-off hole
327  conduction-band-energies     = 2.979d0  3.275d0  3.441d0   ! DEFAULT       ! DEFAULT at 0 K
```

```
328 !conduction-band-energies     = 2.882d0  3.167d0  3.359d0                   ! 300K: E_g(Gamma)
    =1.422 (Varshni formula) conduction band edge energies relative to valence band number 1 (
    number corresponds
329  valence-band-energies        = 1.346d0                                     ! Zunger valence
     band edge energies relative to valence band number 1 (number corresponds
330  band-shift                   = 0d0                                         ! [eV]
331  6x6kp-parameters             = -16.220d0  -3.860d0  -17.580d0              ! L,M,N [hbar^2/2m
     ](--> divide by hbar^2/2m)
332                                 0.341d0                                     ! delta_(split-off)
                                      in [eV]
333 $end_binary-zb-default                                                      !
334 !---------------------------------------------------------------------------!
335 
336 !---------------------------------------------------------------------------!
337 ! Here we are overwriting the database entries for AlAs.                    !
338 ! E_gap = 4.049 - 0.857 - 1/3 * 0.28 = 3.098667 eV   (  0 K)                !
339 ! E_gap = 3.953 - 0.857 - 1/3 * 0.28 = 3.002667 eV   (300 K)                !
340 !---------------------------------------------------------------------------!
341 $binary-zb-default                                                          !
342  binary-type                  = AlAs-zb-default                             !
343  apply-to-material-numbers    = 1                                           !
344  conduction-band-masses       = 0.15d0    0.15d0   0.15d0     ! DEFAULT     ! Gamma cb1 - 1st
     principal axis, 2nd, 3rd
345                                1.32d0    0.15d0   0.15d0     ! DEFAULT     ! L     cb2 - 1st
                                    principal axis, 2nd, 3rd - m_l m_t m_t
346                                0.97d0    0.22d0   0.22d0     ! DEFAULT     ! X     cb3 - 1st
                                    principal axis, 2nd, 3rd - m_l m_t m_t
347  valence-band-masses          = 0.5d0     0.5d0    0.5d0      ! DEFAULT     ! hh (Landolt-
     Boernstein) possible values > 0.0  [m0]. Ordering of numbers corresponds to band Nr. 1, 2,
      ...
348                                0.26d0    0.26d0   0.26d0     ! DEFAULT     ! lh (Landolt-
                                    Boernstein)
349                                0.28d0    0.28d0   0.28d0     ! DEFAULT     ! so
350  conduction-band-energies     = 4.049d0   3.410d0  3.190d0    ! DEFAULT     ! DEFAULT at 0 K
351 !conduction-band-energies     = 3.953d0   3.302d0  3.114d0                  ! 300 K !!! Birner
    suggestion conduction band edge energies relative to valence band number 1 (number
    corresponds
```

```
352  valence-band-energies        = 0.857d0                       ! DEFAULT     ! Zunger valence
         band edge energies relative to valence band number 1 (number corresponds
353  band-shift                   = 0d0                                         ! [eV]
354  6x6kp-parameters             = -8.040d0  -3.120d0 -8.520d0                 ! L,M,N [hbar^2/2m
         ](--> divide by hbar^2/2m)
355                                  0.28d0                                     ! delta_(split-off)
                                      in [eV]
356 $end_binary-zb-default                                                     !
357 !--------------------------------------------------------------------------!
358
359 !--------------------------------------------------------------------------!
360 ! Here we are overwriting the database entries for Al(x)Ga(1-x)As.          !
361 !--------------------------------------------------------------------------!
362 $ternary-zb-default                                                        !
363  ternary-type                 = Al(x)Ga(1-x)As-zb-default                   !
364  apply-to-material-numbers    = 2                                           !
365  bow-conduction-band-masses   = 0.000d0  0.000d0  0.000d0                   ! Bowing parameters
          b are defined for Q[A(x)B(1-x)C] = x*Q[AC]+(1-x)*Q[BC]-b*x*(1-x)
366                                 0.000d0  0.000d0  0.000d0                   !
367                                 0.000d0  0.000d0  0.000d0                   !
368 !bow-conduction-band-energies = 0.0d0    0.0d0    0.055d0                   ! ZERO BOWING
369 !bow-conduction-band-energies = 0.135d0  0.0d0    0.055d0                   ! 0.135 for x=0.20
370  bow-conduction-band-energies = 0.305d0  0.0d0    0.055d0                   ! DEFAULT -0.127d0
         +1.310x for E_g(Gamma) Vurgaftman
371 !                              0.384d0  for Al0.39GaAs                      ! Crossover at x
        =0.39 (300 K) Gamma-L
372 !                              0.3315d0 for Al0.35GaAs                      !
373 !                              0.305d0  for Al0.33GaAs                      !
374 !                              0.266d0  for Al0.30GaAs                      !
375 !                              0.135d0  for Al0.20GaAs                      !
376 !                              0.0695d0 for Al0.15GaAs                      !
377 $end_ternary-zb-default                                                    !
378 !--------------------------------------------------------------------------!
379
380 !****** END MATERIALS AND ALLOY PROFILES **********************************!
381
382 !****** QUANTUM ***********************************************************!
383
```

```
384 !----------------------------------------------------------------------------!
385 ! Including quantum models (1-band Schroedinger, multi-band kp)              !
386 !                                                                            !
387 ! For quantum solutions, you have to define quantum regions and clusters on !
388 ! which certain quantum models are applied. The syntax of the quantum        !
389 ! regions and clusters is the same as for current and material regions.     !
390 !                                                                            !
391 ! The model specifies the kind of equation that is solved in the certain    !
392 ! cluster.                                                                   !
393 !                                                                            !
394 ! Example:                                                                   !
395 ! You could solve the 1-band Schroedinger equation for conduction band 2    !
396 ! and valence bands 1 2 3. For each band you could specify 10               !
397 ! eigenvalues in 'number-of-eigenvalues-per-band␣=␣10␣10␣10'.               !
398 !                                                                            !
399 !----------------------------------------------------------------------------!
400
401 !----------------------------------------------------------------------------!
402 $quantum-regions                                                             !
403
404  !-------------------------------------------------
405  ! Here we use a circular shaped quantum cluster.
406  !-------------------------------------------------
407
408  !---------------------------------------
409  ! left half circle
410  !---------------------------------------
411  region-number = 1    base-geometry = semiellipse region-priority = 1       !
412  semi-ellipse-base = 0d0    0d0  -%ShellOuterRadius    %ShellOuterRadius
413  semi-ellipse-top  = -125.79d0   0d0
414                                                                              !
415  !---------------------------------------
416  ! right half circle
417  !---------------------------------------
418  region-number = 2    base-geometry = semiellipse region-priority = 1       !
419  semi-ellipse-base = 0d0   0d0   -%ShellOuterRadius   %ShellOuterRadius
420  semi-ellipse-top  = 125.79d0  0d0
421
```

```
422 $end_quantum-regions                                                      !
423 !------------------------------------------------------------------------!
424 
425 !------------------------------------------------------------------------!
426 $quantum-cluster                                                          !
427  cluster-number         = 1                                               !
428  region-numbers         = 1 2                                             !
429  deactivate-cluster     = no                                              !
430 $end_quantum-cluster                                                      !
431 !------------------------------------------------------------------------!
432 
433 
434 !****** QUANTUM MODELS ****************************************************!
435 
436 !------------------------------------------------------------------------!
437 $quantum-model-electrons                                                  !
438  model-number                          =  1                               !
439  model-name                            =  effective-mass                  !effective-mass
440  cluster-numbers                       =  1                               !
441  conduction-band-numbers               =  1                               ! 1 = Gamma, 2 = L,
       3 = X
442  number-of-eigenvalues-per-band        =  4                               !
443  boundary-condition-100                =  Dirichlet                       !
444  boundary-condition-010                =  Dirichlet
445 
446 $end_quantum-model-electrons                                              !
447 !------------------------------------------------------------------------!
448 
449 !------------------------------------------------------------------------!
450 $quantum-model-holes                                                      !
451  model-number                          =  1                               !
452  model-name                            =  effective-mass                  !8x8kp, 6x6kp or
      effective-mass
453  cluster-numbers                       =  1                               ! (quantum) cluster
       numbers to which this model applies
454  valence-band-numbers                  =  1                               !2  3hh, lh, so
455 !number-of-eigenvalues-per-band        =  10 10 10                        ! how many
    eigenenergies have to be calculated in each band (minimum)
```

```
456 !valence-band-numbers                    =  1                              ! hh
457  number-of-eigenvalues-per-band          =  1                              ! how many
         eigenenergies have to be calculated in each band (minimum)
458  boundary-condition-100                  =  Dirichlet                      ! Neumann or (
         Dirichlet|dirichlet|DIRICHLET).
459  boundary-condition-010                  =  Dirichlet                      ! Neumann or (
         Dirichlet|dirichlet|DIRICHLET).
460
461 $end_quantum-model-holes                                                   !
462 !--------------------------------------------------------------------------!
463
464 !****** END QUANTUM MODELS *************************************************!
465
466
467 !****** END QUANTUM ********************************************************!
468
469
470 !****** OUTPUT *************************************************************!
471
472 !--------------------------------------------------------------------------!
473 ! For the output the destination directories are free to choose whereas the !
474 ! filenames are fixed and incorporate all information about the files.      !
475 !--------------------------------------------------------------------------!
476 $poisson-boundary-conditions
477  poisson-cluster-number                  =  1                  ! Gate Top
478  region-cluster-number                   =  4
479  applied-voltage                         = 0d0
480  boundary-condition-type                 = !ohmic !schottky
481  !schottky-barrier                        = 2.52d0
482  contact-control                         = voltage
483
484  poisson-cluster-number                  =  2                  ! Gate Left
485  region-cluster-number                   =  5
486  applied-voltage                         = 0d0
487  boundary-condition-type                 = !ohmic !schottky
488  !schottky-barrier                        = 2.52d0
489  contact-control                         = voltage
490
```

```
491  poisson-cluster-number                  =  3                    ! Gate Right
492  region-cluster-number                   =  6
493  applied-voltage                         = 0.3d0
494  boundary-condition-type                 = !ohmic !schottky
495  !schottky-barrier                        = 2.52d0
496  contact-control                         = voltage
497
498  poisson-cluster-number                  =  4                   ! Gate Bottom
499  region-cluster-number                   =  7
500  applied-voltage                         = 0d0
501  boundary-condition-type                 = !ohmic !schottky
502  !schottky-barrier                        = 2.52d0
503  contact-control                         = voltage
504
505 $end_poisson-boundary-conditions
506 !----------------------------------------------------------------------------------------------------------

507
508 !---------------------------------------------------!
509 !-----------------------------------------------------------------------------!
510 $global-settings                                                              !
511  output-directory           = output/
512  number-of-parallel-threads = 1                                               ! 2 = for dual-core
      CPU / 4 = for quad-core CPU
513  debug-level                = 0                                               !
514 $end_global-settings                                                          !
515 !-----------------------------------------------------------------------------!
516
517 !-----------------------------------------------------------------------------!
518 ! This is the output for the band structure and the potential.               !
519 !-----------------------------------------------------------------------------!
520 $output-bandstructure                                                         !
521  destination-directory                   = band_structure/
522  conduction-band-numbers                 = 1 !2 3                             ! 1 = Gamma, 2 = L,
      3 = X
523 !valence-band-numbers                    = 1 2 3                              ! hh, lh, so
524  valence-band-numbers                    = 1                                  ! hh
525  potential                               = no                                 !
```

```
$end_output-bandstructure                                                     !
!-----------------------------------------------------------------------------!

!-----------------------------------------------------------------------------!
! OUTPUT 1-BAND SCHROEDINGER                                                  !
!                                                                             !
! For the 1-band Schroedinger solutions a filename looks like:                !
!   'qm_cb001_qr001_sg001min001max010num_deg001_dir.dat'                      !
!                                                                             !
! In this file the eigenvalues and eigenfunctions are stored for              !
!   parameter:  cb001:   conduction band 1                                    !
!               qr001:   quantum region 1                                     !
!               sg001:   Schroedinger equation 1                              !
!               min001:  minimum eigenvalue                                   !
!               max010:  maximum eigenvalue                                   !
!               deg001:  number of subsolution                                !
!               _dir:    boundary condition (dir=Dirichlet, neu=Neumann)      !
!                                                                             !
! The file 'sg-structure.dat' provides some information about the             !
! structure of the 1-band solutions.                                          !
!                                                                             !
! Meaning of                                                                  !
!   num_sg   For different band energies, different Schroedinger              !
!            equations have to be solved. These are numbered by num_sg.       !
!   num_deg  For equal energy but different masses, again, different          !
!            equations have to be solved which are then numbered by num_deg.!
!-----------------------------------------------------------------------------!
$output-1-band-schroedinger                                                   !
 destination-directory                = Schroedinger_1band/
 sg-structure                         = yes                                   !
!scale                                = 1d0                                   !
 conduction-band-numbers              = 1                                     !
 cb-min-ev                            = 1                                     !
 cb-max-ev                            = 5                                     !
 valence-band-numbers                 = 1 2 3                                 !
 vb-min-ev                            = 1                                     !
 vb-max-ev                            = 2                                     !
```

```
563  complex-wave-functions                  = yes                               ! output amplitude
         psi
564  interband-matrix-elements               = yes                               !
565  shift-wavefunction-by-eigenvalue        = no                                ! This is useful if
         you want to plot the psi^2 and the band edge in one plot.
566 $end_output-1-band-schroedinger                                              !
567 !----------------------------------------------------------------------------!
568
569 !----------------------------------------------------------------------------!
570 $output-section                                                              !
571  section-number = 1    section-name = vertical_slice_middle_along   section-type = x     x = 0
        d0  !  1D slice through center
572  section-number = 2    section-name = horizontal_slice_middle_along section-type = y     y = 0
        d0  !  1D slice through center
573 $end_output-section                                                          !
574 !----------------------------------------------------------------------------!
575
576 !****** END OUTPUT *********************************************************!
```

B.2 Python code for 2D Gaussian fit of output wave-functions from Next Nano

```
1  import scipy.optimize as opt
2  import numpy as np
3  import matplotlib.pyplot as plt
4  from mpl_toolkits.mplot3d import Axes3D
5  import matplotlib.cm as cm
6  import xlrd
7  from scipy.integrate import simps
8  from pandas import DataFrame
9  import matplotlib.ticker as ticker
10 # import matplotlib.pyplot as plt
11 # import matplotlib.pyplot as plt
12
```

```
13 df=DataFrame(index=['sigmax_e','sigmay_e','sigmax_h','sigmay_h','Lx_eh','Ly_eh','fss', 'overlap
       '], columns=['L(nm)','Energy(ev)'])
14
15 hbar =  6.582119514e-16
16 Eg = 1.519
17 Ep = 23
18 e = 1.6e-19
19 m = 9.1e-31
20
21
22 width = 3.4
23 height = width / 1.618
24
25 file = 0.7
26 file_name_hh = str(file) + "_hh"
27 initial_guess = (0.005,0,0,5.0,5.3,0,1)
28
29
30 file_location1 = "C:\\Users\\Zeeshan\\Desktop\\Simulations\\Next_Nano_Data\\Dot_28_30\\TB_-LR_+
       lateral\\"+ file_name_hh +".xlsx"
31 workbook = xlrd.open_workbook(file_location1)
32 sheet =  workbook.sheet_by_index(0)
33
34 x = []
35 for row in range(0,223):
36     r = sheet.cell_value(row,0)
37     x.append(r)
38 # print(x)
39 x=np.array(list(x))
40 y = []
41 for row in range(224,447):
42     r = sheet.cell_value(row,0)
43     y.append(r)
44 y=np.array(list(y))
45 x,y = np.meshgrid(x, y)
46
47
48 #define model function and pass independant variables x and y as a list
```

```
49 def twoD_Gaussian(xdata_tuple, amplitude, xo, yo, sigma_x, sigma_y, theta, offset):
50     (x, y) = xdata_tuple
51     xo = float(xo)
52     yo = float(yo)
53     a = (np.cos(theta)**2)/(2*sigma_x**2) + (np.sin(theta)**2)/(2*sigma_y**2)
54     b = -(np.sin(2*theta))/(4*sigma_x**2) + (np.sin(2*theta))/(4*sigma_y**2)
55     c = (np.sin(theta)**2)/(2*sigma_x**2) + (np.cos(theta)**2)/(2*sigma_y**2)
56     g = offset + amplitude*np.exp( - (a*((x-xo)**2) + 2*b*(x-xo)*(y-yo)
57                         + c*((y-yo)**2)))
58     return g.ravel()
59
60 #hole_fitting
61 # data_hh
62
63 file_name_hh = str(file) + "_hh"
64 initial_guess = (0.005,0,0,5.5,5.5,20,1)
65
66 file_location1 = "C:\\Users\\Zeeshan\\Desktop\\Simulations\\Next_Nano_Data\\Dot_28_30\\TB_-LR_+
       lateral\\"+ file_name_hh+".xlsx"
67 workbook = xlrd.open_workbook(file_location1)
68 sheet =  workbook.sheet_by_index(0)
69
70 data_hh_r = []
71 for row in range(448,sheet.nrows):
72     r = sheet.cell_value(row,1)
73     data_hh_r.append(r)
74 data_hh_r=list(data_hh_r)
75 matdata_hh_r=np.array(data_hh_r)
76
77 data_hh_i = []
78 for row in range(448,sheet.nrows):
79     r = sheet.cell_value(row,2)
80     data_hh_i.append(r)
81 data_hh_i=list(data_hh_i)
82 matdata_hh_i=np.array(data_hh_i)
83
84 matdata_hh_total = matdata_hh_r + 1J * (matdata_hh_i)
85 #matdata_hh = (np.real(np.conjugate(matdata_hh_total) * matdata_hh_total))
```

```
86  matdata_hh = (np.absolute(matdata_hh_total))**2
87
88
89  popt, pcov = opt.curve_fit(twoD_Gaussian, (x, y), matdata_hh, p0=initial_guess)
90
91
92  data_fitted_hh = twoD_Gaussian((x, y), *popt)
93
94
95
96  fig, ax = plt.subplots(1,1)
97
98  fig.set_size_inches(width, height)
99  p = ax.pcolor(x, y, matdata_hh.reshape(223, 223), cmap=cm.jet, vmin=abs(matdata_hh.reshape(223,
        223)).min(), vmax=abs(matdata_hh.reshape(223, 223)).max())
100 cb = fig.colorbar(p)
101 plt.axis([-15,15,-15,15])
102 title_font = {'fontname':'Arial', 'size':'16', 'color':'black', 'weight':'normal',
103               'verticalalignment':'bottom'} # Bottom vertical alignment for more space
104 axis_font = {'fontname':'Arial', 'size':'8','labelsize': '8'}
105 # ax.contour(x, y, data_fitted_hh.reshape(223, 223), 8, colors='w')
106 plt.xlabel('Dimension␣(nm)',size=8)
107 plt.ylabel('Dimension␣(nm)',size=8)
108 plt.rc('xtick', labelsize=8)
109 plt.rc('ytick', labelsize=8)
110 ax.set_aspect('equal')
111 plt.tight_layout()
112 # print(popt)
113 # fig.savefig(file_name_hh+".pdf")
114 plt.show()
115 df.set_value('sigmax_h', 'L(nm)', float(popt[3]))
116 df.set_value('sigmay_h', 'L(nm)', float(popt[4]))
117
118 # el_fitiing
119
120 file_name_el = str(file) + "_el"
121
122 file_location2 = "C:\\Users\\Zeeshan\\Desktop\\Simulations\\Next␣Nano␣Data\\Dot_28_30\\TB_-LR_+
```

```
    lateral\\" + file_name_el + ".xlsx"
123 workbook = xlrd.open_workbook(file_location2)
124 sheet =  workbook.sheet_by_index(0)
125 
126 
127 data_el_r = []
128 for row in range(448,sheet.nrows):
129     r = sheet.cell_value(row,1)
130     data_el_r.append(r)
131 data_el_r=list(data_el_r)
132 matdata_el_r=np.array(data_el_r)
133 
134 data_el_i = []
135 for row in range(448,sheet.nrows):
136     r = sheet.cell_value(row,2)
137     data_el_i.append(r)
138 data_el_i=list(data_el_i)
139 matdata_el_i=np.array(data_el_i)
140 
141 matdata_el_total = matdata_el_r + 1J * (matdata_el_i)
142 # matdata_el = (np.real(np.conjugate(matdata_el_total) * matdata_el_total))
143 matdata_el = (np.absolute(matdata_el_total))**2
144 initial_guess = (0.005,0,0,6,6,0,1)
145 popt, pcov = opt.curve_fit(twoD_Gaussian, (x, y), matdata_el, p0=initial_guess)
146 
147 
148 data_fitted_el = twoD_Gaussian((x, y), *popt)
149 
150 
151 # plt.figure()
152 fig, ax = plt.subplots(1,1)
153 fig.set_size_inches(width, height)
154 p = ax.pcolor(x, y, matdata_el.reshape(223, 223), cmap=cm.jet, vmin=abs(matdata_el.reshape(223,
     223)).min(), vmax=abs(matdata_hh.reshape(223, 223)).max())
155 cb = fig.colorbar(p)
156 plt.axis([-15,15,-15,15])
157 title_font = {'fontname':'Arial', 'size':'16', 'color':'black', 'weight':'normal',
158               'verticalalignment':'bottom'} # Bottom vertical alignment for more space
```

```
159 axis_font = {'fontname':'Arial', 'size':'8','labelsize': '8'}
160 # ax.contour(x, y, data_fitted_el.reshape(223, 223), 8, colors='w')
161 plt.xlabel('Dimension␣(nm)',size=8)
162 plt.ylabel('Dimension␣(nm)',size=8)
163 plt.rc('xtick', labelsize=8)
164 plt.rc('ytick', labelsize=8)
165 ax.set_aspect('equal')
166 # print(popt)
167 plt.tight_layout()
168 # fig.savefig(file_name_el+".pdf")
169 df.set_value('sigmax_e', 'L(nm)', float(popt[3]))
170 df.set_value('sigmay_e', 'L(nm)', float(popt[4]))
171 plt.show()
```